

SIGNAL PROCESSING IN  
SINGLE MOLECULE STUDIES

A Dissertation

Presented to the Faculty of the Graduate School  
of Cornell University

in Partial Fulfillment of the Requirements for the Degree of  
Doctor of Philosophy

by

Pangshun Zhu

January 2012

© 2012 Pangshun Zhu  
ALL RIGHTS RESERVED

SIGNAL PROCESSING IN  
SINGLE MOLECULE STUDIES

Pangshun Zhu, Ph.D.

Cornell University 2012

In this dissertation, I present signal processing techniques used in investigating single molecule kinetics and interactions. The first chapter provides an overview of signals and systems pertaining to single molecule studies. It discusses the need for signal processing, and gives a summary of current single molecule techniques. The second chapter introduces two techniques developed in our research using fluorescence microscopy, namely, spectral deconvolution in multi-color fluorescent microscopy systems; and fluorescent pattern recognition in the time domain using the correlation functions. In the third chapter, spectral deconvolution is demonstrated in separating autofluorescence from the fluorescence of enzyme label, used in quantitative fluorescence studies. In the fourth chapter, I discuss the fabrication of sub-wavelength metallic apertures that are used in single-molecule studies. I also discuss how optical properties of these devices are modeled and characterized. In the fifth chapter, I demonstrate how matched filter is used to give a precise quantitative measure of GFP fluorescence upon GFP aptamer binding. Similar technique is used to recognize photon bursts as a fluorescent molecule passes through an observation volume, discussed in the sixth chapter. I use this method to analyze the mobility of molecules in a fluidic channel. Chapter seven provides a summary and outlook for future studies.

## **BIOGRAPHICAL SKETCH**

Pangshun Zhu (朱庞顺) was born in Quzhou, a small town in southeastern China's Zhejiang province. He earned his Bachelor's degree from University of Kentucky, and Master's degree from the Johns Hopkins University, both in Electrical Engineering. After seven years in consumer electronics industry, Mr. Zhu joined Cornell's Applied Physics Ph.D. program.

*Intelligence is like four-wheel drive. It only allows you to get stuck  
in more remote places.*

– Garrison Keillor

## ACKNOWLEDGEMENTS

I want to thank Professor Harold Craighead for accepting me into his research group, where I had many opportunities to work with various projects using diverse technologies. I want to thank the many group members who have provided valuable help and discussion. In particular, Ben Cipriany help me with optics set up. Without his help I would still be in the dark ages; Kylan Szeto was inspirational in discussions and brain storming; Kevan Samiee showed me how to make Zero-Mode Waveguides; Jose Moran-Mirabal provided labeled cellulase for pretreated wood studies; Josh Cross showed me the fine art of channel making and wafer bonding; and Rob Reichenbach was the first group member that led me to the world of MEMS and nanofabrication. I also thank Dr. Huizhong Xu for providing finite element simulation model of ZMWs, and showing me how to run COMSOL program. I thank professor John Lis and professor Jerome Hass for being on my special committee, providing guidance in my studies of molecular biology and managerial economics.

Nano-fabrication were done at the Cornell Nanoscale Science and Technology Facility, a member of the National Nanotechnology Infrastructure Network, which is supported by the National Science Foundation (Grant ECS-0335765). The research on pretreated wood particles was funded by DOE Contract GO18084, and made use of the Biofuel Research Laboratories at Cornell University, which was funded by the New York State Foundation for Science, Technology and Innovation. GFP-Aptamer was provided by Abdullah of Lis Lab. The aptamer study was funded by Grant 1R01DA030329-01.

Finally, I also want to thank my flight instructors Rick Prado, Terry Mason, and David St. George at East Hill Flying Club. With patience and grace, they guided me to the sky, and taught me to be in control for every safe landing.

## TABLE OF CONTENTS

|  |           |
|--|-----------|
| Biographical Sketch . . . . .  | iii       |
| Dedication . . . . .   | iv        |
| Acknowledgements . . . . .   | v         |
| Table of Contents . . . . .  | vi        |
| List of Figures . . . . .  | ix        |
| List of Tables . . . . .   | xvii      |
| List of Abbreviations . . . . .  | xviii     |
| <b>1 Introduction</b>  | <b>1</b>  |
| 1.1 Introduction . . . . .   | 2         |
| 1.2 Single Molecule Studies . . . . .                                    | 3         |
| 1.2.1 Motivation . . . . .   | 3         |
| 1.2.2 Signal Processing in Single Molecule Studies . . . . .             | 4         |
| 1.3 Techniques to increase SNR in Single Molecule Studies . . . . .      | 5         |
| 1.3.1 Limit the Number of Observable Molecules . . . . .                 | 5         |
| 1.3.2 Integrate to Utilize Redundancy . . . . .                          | 10        |
| 1.4 Maximize Signal Energy . . . . .                                     | 12        |
| <b>2 Signal Processing Techniques Used in Single Molecule Studies</b>    | <b>14</b> |
| 2.1 Introduction . . . . .   | 15        |
| 2.2 Spectral Deconvolution . . . . .                                     | 16        |
| 2.2.1 Motivation: Spectra Bleed-Through . . . . .                        | 18        |
| 2.2.2 Quantitative Fluorescence Microscopy . . . . .                     | 18        |
| 2.2.3 Demonstration of Spectral Deconvolution . . . . .                  | 21        |
| 2.3 Matched Filtering . . . . .  | 24        |
| 2.3.1 Where Do We Need Matched Filtering . . . . .                       | 24        |
| 2.3.2 Problem Definition . . . . .                                       | 24        |
| 2.3.3 Matched Filter and Cauchy-Schwarz Inequality . . . . .             | 26        |
| 2.3.4 The Adaptive Filter . . . . .                                      | 27        |
| 2.3.5 Implementation . . . . .   | 29        |
| 2.3.6 Results . . . . .  | 30        |
| <b>3 Cellulase Binding to Wood Particles</b>                             | <b>35</b> |
| 3.1 Introduction . . . . .   | 36        |
| 3.2 Transient Enzyme-Binding Model . . . . .                             | 38        |
| 3.3 Materials and Methods . . . . .                                      | 40        |
| 3.4 Results and Discussion . . . . .                                     | 45        |
| 3.5 Conclusions of Binding Study using CLSM . . . . .                    | 56        |
| 3.6 Advanced Discussions on Diffusion and Binding . . . . .              | 57        |
| 3.6.1 Diffusion of fluorescent probes into cellulose particles . . . . . | 57        |
| 3.6.2 Interstitial Diffusion and Binding Model . . . . .                 | 62        |
| 3.6.3 Competitive Binding . . . . .                                      | 68        |
| 3.7 Future Studies . . . . .   | 72        |

|          |  |            |
|----------|--|------------|
| <b>4</b> | <b>Optical Properties of Zero-Mode Waveguides</b>                      | <b>73</b>  |
| 4.1      | Introduction . . . . .   | 74         |
| 4.2      | Motivation . . . . .   | 76         |
| 4.3      | Fabrication of Zero-Mode Apertures . . . . .                           | 79         |
| 4.4      | Characterize Zero Mode Waveguides . . . . .                            | 82         |
| 4.4.1    | Several aspects of Zero Mode Waveguides . . . . .                      | 82         |
| 4.5      | Electromagnetic Solution of Zero-Mode Apertures . . . . .              | 88         |
| 4.5.1    | Wave Solution in Cylindrical Coordinates . . . . .                     | 88         |
| 4.5.2    | Numerical Solution Using Finite Element Methods . . . . .              | 91         |
| 4.6      | Simulation Results . . . . .   | 96         |
| 4.7      | Experimental Materials and Methods . . . . .                           | 101        |
| 4.7.1    | Tunable Filter for Measuring Transmission . . . . .                    | 101        |
| 4.7.2    | Aluminum Oxide Filling by Atomic Layer Deposition . . . . .            | 102        |
| 4.8      | Results and Discussion . . . . .                                       | 110        |
| 4.8.1    | Transmission Properties . . . . .                                      | 110        |
| 4.8.2    | Illumination Profile Inside Apertures . . . . .                        | 112        |
| 4.9      | Conclusion . . . . .   | 114        |
| <b>5</b> | <b>GFP Aptamer Binding to GFP</b>                                      | <b>115</b> |
| 5.1      | Introduction . . . . .   | 116        |
| 5.2      | Background . . . . .   | 116        |
| 5.3      | Fluorescence Measurement of Many Molecules . . . . .                   | 120        |
| 5.3.1    | Materials and Methods . . . . .  | 120        |
| 5.3.2    | In Solution . . . . .  | 121        |
| 5.3.3    | Immobilized on Surface . . . . .                                       | 122        |
| 5.3.4    | Whether Aptamer completely quenches GFP . . . . .                      | 124        |
| 5.4      | Single-Molecule Measurements . . . . .                                 | 125        |
| 5.4.1    | Lack of Aptamer Unbinding from GFPs . . . . .                          | 126        |
| 5.4.2    | GFP-AP3 Interaction Model . . . . .                                    | 129        |
| 5.5      | Conclusion . . . . .   | 140        |
| 5.6      | Appendix . . . . .   | 142        |
| 5.6.1    | Poisson Process . . . . .  | 142        |
| 5.6.2    | GFP interaction with ZMW . . . . .                                     | 143        |
| 5.6.3    | Running GFP in Nanofluidic Channel . . . . .                           | 144        |
| 5.6.4    | Reconstructed GFP photon burst from correlation function . . . . .     | 146        |
| 5.6.5    | Background Correction in FCS Models . . . . .                          | 146        |
| <b>6</b> | <b>Mobility Studies of Fluorescent Molecules under Electrophoresis</b> | <b>148</b> |
| 6.1      | Introduction . . . . .   | 149        |
| 6.2      | Theory of Electrophoresis in fluidic Channels . . . . .                | 150        |
| 6.3      | Materials and Methods . . . . .  | 153        |
| 6.3.1    | Optical Setup . . . . .  | 153        |
| 6.3.2    | Channel Fabrication . . . . .  | 154        |
| 6.3.3    | Analyte Preparation . . . . .  | 158        |

|          |   |            |
|----------|---|------------|
| 6.3.4    | Electrical Setup . . . . .                                | 160        |
| 6.4      | Results and Discussion . . . . .                          | 162        |
| 6.4.1    | 2-spot separation . . . . .                               | 162        |
| 6.4.2    | From Photon Traces to Cross-Correlation . . . . .         | 163        |
| 6.4.3    | Mobility of Different DNA Constructs . . . . .            | 167        |
| 6.4.4    | Differences between Long and Short Channels . . . . .     | 167        |
| 6.4.5    | Differences between Shallow and Deep Channels . . . . .   | 169        |
| 6.4.6    | Mobilities of Quantum Dots and DNA Constructs . . . . .   | 170        |
| 6.5      | Conclusion . . . . .                                      | 172        |
| <b>7</b> | <b>Summary and Future Studies</b>                         | <b>174</b> |
| 7.1      | Summary . . . . .   | 175        |
| 7.1.1    | Techniques to Increase SNR in Single Molecule Studies . . | 175        |
| 7.2      | Future Research . . . . .                                 | 176        |
| 7.2.1    | Single Molecule Studies in ZMW and nanofluidic Channels   | 176        |
| 7.2.2    | Cellulose . . . . .                                       | 177        |
| 7.2.3    | System Integration with Electronics . . . . .             | 178        |
| 7.2.4    | Single Molecule Sorting Based on Mobility . . . . .       | 179        |
| 7.3      | Conclusion . . . . .                                      | 180        |
|          | <b>Bibliography</b>                                       | <b>182</b> |

## LIST OF FIGURES

|     |   |    |
|-----|---|----|
| 1.1 | Artist rendition of the Voyager spacecraft. <i>From NASA (67)</i> . . . .   | 2  |
| 1.2 | Block diagram of system estimation process. Due to uncertainty in measurement, an estimation of the state of a system is never the exact replica of reality. . . . .  | 4  |
| 2.1 | Sample image of a wood particle incubated with Alexa-488 labeled Cel6B and Alexa-647 labeled Cel9A. . . . .   | 17 |
| 2.2 | Normalized emission curves of AF-488 and pre-treated wood particles when excited with 488nm laser. Fluorescence spectra were taken with Leica TCS SP2 Confocal laser scanning microscope (Leica Microsystems, GmbH, Wetzlar, Germany) with prism and variable slit, recording emission from 500nm to 700nm at 10nm steps and 10nm spectral bandwidth. Data and error bar at every wavelength are average and standard deviation of pixel values of the image for that wavelength, respectively. | 19 |
| 2.3 | Determining linear range of CLSM system by imaging (a) 5'-dUTP-Alexa 488 and, (b) 5'-dUTP-Alexa 647 fluorophores at concentrations between 20nM and 10 $\mu$ M, with excitation lasers at 488nm, 543nm and 635nm all set at 2% of respective maximum power levels. For a 12-bit image, pixel intensities less than 3500 are assumed linearly correlated with fluorophore concentration.   | 22 |
| 2.4 | Relative spectral intensity distribution of Alexa-488, autofluorescence of pretreated wood, and Alexa-647, in three collection channels. The actual numerical values form the cross-talk matrix elements $\alpha_{ij}$ of <b>A</b> , and is used in spectral separation to recover each fluorophore's concentration, and deduce the amount of bound enzymes . . . . .   | 23 |
| 2.5 | We test the pulse-recovering algorithm with a A. square wave, B, arbitrary wave and C, cosine wave. Their autocorrelation functions are first generated and Fourier Transformed to generate the energy spectra. Subsequent inverse Fourier Transform of the square root of the energy spectra reproduces the original pulse shape. . . . .  | 31 |
| 2.6 | Sample photon spectral analysis with and without binning and filtering. . . . .   | 32 |
| 2.7 | Sample photon trace and intensity trace as result of filtering. . . .   | 33 |

|     |  |    |
|-----|--|----|
| 3.1 | Confocal Laser Scanning Microscope set up using Olympus Flouview® 1000 system. Excitation lasers at 488nm, 543nm and 635nm are combined and scanned to illuminate the specimen through a SAPO 100x Oil objective with Numerical Aperture (N.A.) of 1.4. Fluorescence signal is collected with the same objective, and passed through a sequence of single band dichroic mirrors (SDM), filtered with band-pass optical filters before being collected by photo-multiplier tubes (PMT) of each channel. . . . . | 44 |
| 3.2 | Scanning Electron Microscope (SEM) images of pre-treated wood particles immobilized on flat surface, showing a. Particles of various sizes and morphologies; b. Fibrous protrusions adhering to the surface, immobilizing the particle; c. Zoom-in view of one particle, showing such surface features as pores and criss-crossing fibers and d. where nano-meter scale pores are clearly visible. . . . .   | 46 |
| 3.3 | Sample enzyme binding images of <i>T. fusca</i> Cel9A labeled with AF488 at discrete time points. AF488-labeled Cel9A in ROX buffer was added to pretreated particles at time 0. Fluorescence in red channel was from wood particle's autofluorescence. . . . .  | 49 |
| 3.4 | Sample enzyme binding images of <i>T. fusca</i> Cel5A labeled with AF488 at four discrete time points. AF488-labeled Cel5A in ROX buffer was added to pretreated particles at time 0, before which point, only autofluorescence was visible. As time progressed, more and more cellulases adsorbed to immobilized particles, represented by accumulation of AF488 fluorescence. Spectra deconvolution routines were used to separate AF488 fluorescence from autofluorescence of wood. . . . .                 | 50 |
| 3.5 | Sample data-fitting curve with 2.5nM, 5nM and 10nM Cel5A-AF488 fluorescence increment data. Each data series as fit to Eq. 3.11. In this case, data points after the initial jump of fluorescence are arbitrarily excluded in order to limit the binding kinetics to the most accessible sites and exclude kinetics involving interstitial diffusion and adsorption. . . . .   | 54 |
| 3.6 | Size distribution of FITC- or TRITC-labeled dextran particles. . . . .   | 58 |
| 3.7 | Fluorescently labeled dextran particles diffusing into pretreated and un-treated wood particles. . . . .   | 59 |
| 3.8 | Simulation of A. Incubation and B. Washing of labeled probes inside porous medium with arbitrary diffusion constants. In general we see the curves follow an exponential decay model. . . . .  | 61 |
| 3.9 | Finite element simulation of diffusive reaction in a porous substrate. . . . .   | 67 |
| 4.1 | Illustration of Zero-Mode-Waveguide devices. . . . .   | 74 |

|      |   |    |
|------|---|----|
| 4.2  | A. SEM image of arrays of ZMWs of increasing sizes from “0” to “9”, Numbers and rectangles visible in this image are fabricated in gold to enhance contrast. Numbers designate column and row, while rectangles enclose ZMW arrays; B. Color image of transmitted light from an incandescent bulb. ZMWs with larger diameters pass more longer wavelength light than those with smaller diameters; C. Measured ZMW diameters compared to design size, from “0” to “9” . . . . . | 77 |
| 4.3  | SEM image of an array of ZMWs at $1\mu m$ spacing, showing apertures (black circular holes) in aluminum where e-beam resist pillars have lifted off; and where resist pillars still remain, with aluminum covering their tops (bright spots); and where the pillars have fallen flat on the substrate surface during the e-beam resist developing stage and were subsequently covered by deposited aluminum. . . . .  | 79 |
| 4.4  | Resulting aperture diameter is a function of total dose and expansion factor $\sigma$ . . . . .   | 85 |
| 4.5  | Evaporated aluminum on top of pillars, creating a shadow for what’s below. . . . .  | 86 |
| 4.6  | Focused-Ion-Beam cross-section cut showing pillar formed by developed NEB-31A before lifting off. . . . .   | 86 |
| 4.7  | SEM Image of a cross-section of a Zero-Mode-Waveguide device, showing approximately 0.2 radian sloped aluminum side-wall. The diameter of the aperture is approximately $150nm$ . . . . .   | 87 |
| 4.8  | ZMW simulation model used in COMSOL. Electric field is arbitrarily defined to be polarized in the $x$ direction. A. Geometric drawing of half a device showing fused silica substrate, aluminum cladding, ALD layer dielectric, and aqueous filling above the ZMW; B. Meshing divides the geometry into 700,000 piecewise linear elements. Corners and curves are segmented with finer elements, whereas coarse elements are used for the open volume. . . . .                  | 92 |
| 4.9  | Refractive index of $SiO_2$ , measured from $170\mu m$ fused silica wafer.  | 94 |
| 4.10 | Optical constants of thermally evaporated aluminum. Complex refractive index is wavelength dependent and is written is $\tilde{n} = n - ik$ .   | 95 |
| 4.11 | Simulated result of attenuation of energy density along the central axis of transmission inside ZMW. Inset shows corresponding color plot of energy density on the same color scale. . . . .  | 96 |
| 4.12 | Decay constants of various metals simulated as cladding surrounding apertures. Energy density along the central axis of aperture is fit to an exponential decay model, $I(z) = I_0 e^{-\eta z}$ , and exponential decay constant $\eta$ is plotted here. . . . .  | 97 |

|      |   |     |
|------|---|-----|
| 4.13 | Time average of electric energy density inside and outside an aperture of diameter=150nm in 100nm-thick aluminum layer, supported by fused silica on one side, and immersed in aqueous solution in another. Light incidents from the fused silica side. Shown in dB scale to include large dynamic range. A. $\lambda = 488nm$ without ALD layer; B. $\lambda = 530nm$ without ALD layer; C. $\lambda = 488nm$ with 20nm $Al_2O_3$ ALD layer; and D. $\lambda = 530nm$ with 20nm $Al_2O_3$ ALD layer. . . . . | 98  |
| 4.14 | Simulated illumination profile inside ZMW with larger opening than entrance. For each plot, the left half represents an aperture with straight side-wall, and the right half represent an aperture with a slanted sidewall. The intensity plots are on the same scale for easy comparison. . . . .  | 100 |
| 4.15 | Tunable Filter setup. The angle of the filter determines the pass band. As the motor (m) drives the filter through one rotation, the permanent magnet (2) triggers the hall effect sensor (3), generating a short pulse. Buffered output (5) momentarily nulls APD output. The zero-photon count region in photon intensity data stream indicates filter position (Angle= $-90^\circ$ ). . . . .  | 103 |
| 4.16 | Sample <i>Versa Chrome</i> Transmission characteristic at $0^\circ$ and $60^\circ$ , two edges of the usable range. . . . .   | 104 |
| 4.17 | Linear relationship between deposited $Al_2O_3$ and the number of ALD cycles. . . . .   | 105 |
| 4.18 | Measured refractive indices of native aluminum oxide and ALD deposited $Al_2O_3$ , smoothed to a Cauchy model $n = 1.583 + \frac{7551}{\lambda^2} + \frac{0.8474}{\lambda^4}$ . . . . .   | 106 |
| 4.19 | Reconstructed 3-D representations of AFM measurement of device profile showing a, height difference $h_0$ between top aluminum and fused silica substrate surfaces without ALD deposition and, b, height difference $h$ with 320 cycles of ALD deposition resulting in $39nm Al_2O_3$ . Both $h_0$ and $h$ are found to be approximately $120nm$ , indicating uniform ALD deposition on both fused silica and aluminum surfaces . . . . .   | 107 |
| 4.20 | Reconstructed 3-D representations of AFM measurement of one ZMW coated with ALD film. The dip in the surface indicates where the ZMW used to be, and is only partially filled with the deposited film. The small lump next to the opening of the dip was most likely due to deposited aluminum that did not completely lift off during the ZMW fabrication process. . . . .   | 108 |
| 4.21 | Scanning Electron Microscope image of a ZMW with a thin layer of ALD film cover. The ALD film is seen to have conformally coated the ZMW aperture. . . . .  | 108 |

|      |  |     |
|------|--|-----|
| 4.22 | Drawing of ZMW with ALD layer. Deposited ALD thickness $t$ conformally coats the inside of ZMWs and shrinks the effective volume of the aperture. . . . .  | 109 |
| 4.23 | Compare measured and simulation results of transmitted light through $156.2 \pm 2.1 \text{ nm}$ aperture in aluminum layer, with and without $20 \text{ nm Al}_2\text{O}_3$ ALD layer. . . . .   | 110 |
| 4.24 | Comparing measured and simulated fluorescence intensity for apertures of two diameters, with and without ALD deposited aluminum. . . . .   | 112 |
| 5.1  | Tertiary structure of Green Fluorescent Protein (GFP) showing beta barrel and its caged fluorophore. Image from the RCSB PDB ( <a href="http://www.pdb.org">www.pdb.org</a> ) of PDB ID 1GFL (109). . . . .  | 117 |
| 5.2  | Chemical structure of GFP fluorophore. (78) . . . . .  | 117 |
| 5.3  | Secondary structure of GFP aptamer AP3 (89). . . . .   | 120 |
| 5.4  | GFP fluorescence in solution with and without Aptamer. . . . .   | 122 |
| 5.5  | Fluorescence of GFP molecules fixed on surface via $\text{Ni}^{2+}$ binding, before and after adding Aptamer solution. . . . .   | 123 |
| 5.6  | Sample photon traces from four ZMWs with adsorbed GFP and bound aptamer, showing bleaching of Cy-3 labels on bound aptamer. We drew in horizontal lines to illustrate where we think single-fluorophore bleaching occurred. There is usually more than one GFP adsorbed in a given ZMW, and hence more than one bound aptamer with Cy-3 label. . . . . | 127 |
| 5.7  | Reaction model of GFP and GFP-aptamer. . . . .   | 129 |
| 5.8  | Excitation and emission spectra of GFP, Cy3, and Dy647. There is very little overlap between GFP and Dy647. Yet there is considerable spectra leak through between Cy3 and GFP, and Cy3 and Dy647. . . . .   | 132 |
| 5.9  | Autocorrelation curves of GFP and Dy-647-labeled aptamers independently. Lack of spectral bleed-through to the corresponding detection channel is shown as a lack in correlation curves, 647nm channel, above, and 488 channel, below. . . . .   | 133 |
| 5.10 | Cross correlation measurement of GFP and Dy647-labeled Aptamer. Though it is a cross-correlation curve, we find Eq. 4.16 provide a good fit. . . . .   | 134 |
| 5.11 | Derived concentration from average number of fluorescent molecules in a ZMW's observation volume. . . . .  | 134 |

|      |  |     |
|------|--|-----|
| 5.12 | Sample photon data traces of GFP and Dy647 labeled aptamer diffusing through ZMW observation volume. Frame G0: 100nM GFP solution without aptamer, and 647nm detection channel background shown in frame A0; Frame G1: 93.3nM GFP with 0.067x aptamer solution, with detected aptamer photon trace shown in frame A1; Frame G2: 84nM GFP with 0.16x aptamer solution, with detected aptamer photon trace shown in frame A2. The slight decrease in background is noticeable from G0 to G1. | 136 |
| 5.13 | Photon statistics of GFP transition through illumination volume inside ZMW. As aptamer concentration is increased, we see a definite shift of GFP peak fluorescence towards the lower.   | 137 |
| 5.14 | Apparent GFP Diffusion time inside metallic apertures gets shorter as excitation laser power is increased. I think this is due to GFP fluorescence gets more easily quenched at higher powers when they interact with metallic walls of the aperture.  | 144 |
| 5.15 | Set up for measuring single molecule fluorescence in nanofluidic channel.  | 145 |
| 5.16 | Reconstructed characteristic photon burst from FCS curve as a GFP or a Dy-647 labeled aptamer diffuses through the illumination volume of a ZMW. We also reconstruct the autocorrelation function from this photon burst and plot the error between the reconstructed correlation function from the measured correlation function.   | 147 |
| 6.1  | Drawing of single molecule separation in nanofluidic channels based on electrophoretic mobility.   | 150 |
| 6.2  | Electrophoresis model of a molecule with mass $m$ , charge $q$ , hydrodynamic radius $r_{\text{hyd}}$ flowing under electric field $E$ in nanofluidic channel where the viscosity of the fluid is $\mu$ , leading to speed $u$ dependent drag force $F_{\text{drag}}$ .  | 151 |
| 6.3  | 2-spot measurement set up.   | 153 |
| 6.4  | CAD design of microfluidic channels for single molecule mobility studies. The A and B windows correspond to Fig. 6.5.A and B AFM measurement frames. We have designed in a cross-junction for possible applications such as voltage/current monitoring, and providing an alternate path for single molecule separation.  | 155 |
| 6.5  | AFM image of etched channel in fused silica substrate before bonding, showing A, 45-degree bend region to be 20% wider, and B, the junction region for potential use as single molecule separation device. Surface curvature shown in frame B is an artifact of AFM.   | 157 |

|      |   |     |
|------|---|-----|
| 6.6  | ssDNA and ssRNA structures for hybridization. The “iSP9” is a triethylene glycol spacer incorporated between RNA bases and fluorophores to minimize possible quenching effect due to Guanine (95). . . . .  | 158 |
| 6.7  | Structures and spectra of fluorescent labels on ssDNA and ssRNA.  | 159 |
| 6.8  | We use fluorescence correlation spectroscopy to confirm the existence of hybrid DNA+RNA molecules. The existence of cross correlation between green and red photon detection channels means there are single molecules containing both green and red fluorophores. . . . .  | 161 |
| 6.9  | 2 laser spot set up with red circles designating laser spot location when using A. twisted channel section and B. straight channel section. Frame A was taken with arc lamp illumination, resulting in much better contrast of water-filled channel region to bonded glass region. Frame B which was taken with overhead lamp illumination, showing poorer contrast. . . . .  | 162 |
| 6.10 | Temporal fluorescence intensity traces of A. Methylated and B. Unmethylated DNA intercalated with YOYO label driven at $60V_{DC}$ . A2 and B2 provide sections of zoom-in view of A1 and B1. Here we used blue and red traces to illustrate two photon detection channels. The actual emission filter for YOYO label is same as FITC dye (green) and hence it is result of a single-color, dual channel detection set up. . . . . | 163 |
| 6.11 | Two-spot measurement of methylated and unmethylated DNA with YOYO label in fluidic channels, showing A, cross-correlation curves with respect to voltages; and B, summary of the averages of transit times with respect to voltages. . . . .  | 164 |
| 6.12 | Compare mobility of hybridized and single-strand oligonucleotide. . . . .   | 166 |
| 6.13 | Compare mobility of hybridized oligonucleotide in twisted and straight channels of different etch depths. Measured transition times between two observation laser spots are fit to Eq. 6.7, and parameters $A$ and $k$ are extracted. . . . .   | 168 |
| 6.14 | Average transit time of dUTP-Alexa488 molecule through two laser spots separated by $16.8\mu m$ , in shallow-etch channel with depth = $85.3nm$ showing non-linear relationship especially at $V_{DC} = 2560V$ . . . . .  | 169 |
| 6.15 | Compare transit times of Quantum Dots and DNA, both detected in the $525nm$ spectral range. Part A shows cross-correlation peaks due to quantum dots and DNA with varying voltages. In part B we plot the average of transit times with respect to drive voltages. . . . .  | 171 |

|     |   |     |
|-----|---|-----|
| 7.1 | Block diagram of single molecule separation based on electrophoretic mobility differences in fluidic channels. With four interrogation spots and four detection devices, fluorescent photon counts are fed to digital signal processor to be filtered and used to calculate molecule mobility in real time. A sorting voltage is triggered based on an empirically determined and dynamically adjustable threshold. . . . . | 179 |
|-----|---|-----|

## LIST OF TABLES

|     |  |     |
|-----|--|-----|
| 3.1 | Fluorescence decay constant $d$ of Equation 3.13 when substrate-bound and fluorescently labeled cellulases were continuously scanned by excitation laser source. . . . .   | 48  |
| 3.2 | Fitting result of $k_1$ for AF488/647-labeled Cel5A, Cel6B and Cel9A. Smaller $k_1$ values at low enzyme concentrations are most likely due to enzyme loss to the petri dish side walls, and hence the actual enzyme concentration was much lower than we had prepared. For this reason, we conclude the binding rates obtained at higher enzyme concentrations are closer to the actual values. . . . . | 55  |
| 4.1 | <i>Versa Chrome</i> filter series center wavelength and pass band width, extracted from simulation results provided by Semrock. .  | 104 |
| 4.2 | Fitting result of exponential decay constant $\eta$ used in equation 4.21. . . . .   | 113 |
| 5.1 | Incubating GFP in ZMWs with Aptamer and Control. Cy-3 labeled AP3 clearly binds to GFP in ZMWs and partially quenches GFP fluorescence, while Cy-3 fluorescence could be detected, indicating aptamer binding. . . . .   | 128 |
| 5.2 | Corrected concentration is the concentration of still fluorescent GFP, inferred from FCS fitting result and corrected to initial starting concentration of 100nM. . . . .  | 139 |
| 6.1 | Channel depth as a result of etch times. Measurement was done using KLA-Tencor profilometer p10 (Milpitas, CA) with 1Å resolution. . . . .   | 156 |
| 6.2 | Characteristic times for Diffusion and Flow after we fit the data shown in Fig. 6.11 to Eq. 6.7. . . . .   | 165 |
| 6.3 | Compare parameters of QD and DNA transit model. . . . .  | 172 |

## LIST OF ABBREVIATIONS

|       |  |
|-------|--|
| AFM   | Atomic Force Microscopy                          |
| ALD   | Atomic Layer Deposition                          |
| APD   | Avalanche Photo Diode                            |
| AU    | Astronomical Unit                                |
| BMCC  | Bacterial Microcrystalline Cellulose             |
| BSA   | Bovine Serum Albumin                             |
| CAD   | Computer Aided Design                            |
| CBM   | Cellulose Binding Module                         |
| CLSM  | Confocal Laser Scanning Microscopy               |
| DOE   | Department of Energy                             |
| DNA   | Deoxyribonucleic acid                            |
| ds    | Double Strand                                    |
| DSP   | Digital Signal Processing                        |
| EDTA  | Ethylenediaminetetraacetic Acid                  |
| EMCCD | Electron-Multiplying Charge-Coupled Device       |
| FCS   | Fluctuation Correlation Spectroscopy             |
| FFT   | Fast Fourier Transform                           |
| FIONA | Fluorescence Imaging with One Nanometer Accuracy |
| FITC  | Fluorescein isothiocyanate                       |
| FRET  | Förster Resonance Energy Transfer                |
| GFP   | Green Fluorescent Protein                        |

|       |  |
|-------|--|
| MEMS  | Microelectromechanical systems                 |
| NSOM  | Near-field scanning optical microscopy         |
| PBS   | Phosphate Buffered Saline                      |
| PMT   | Photo Multiplier Tube                          |
| QD    | Quantum Dot                                    |
| RF    | Radio Frequency                                |
| RNA   | ribonucleic acid                               |
| ROI   | Region of Interest                             |
| SELEX | Systematic Evolution by Exponential Enrichment |
| SEM   | Scanning Electron Microscopy                   |
| SNR   | Signal-to-Noise Ratio                          |
| ss    | Single Strand                                  |
| STED  | Stimulated Emission Depletion                  |
| TE    | Tris-EDTA                                      |
| TIRF  | Total Internal Reflection Fluorescence         |
| TRITC | Tetramethylrhodamine Isothiocyanate            |
| ZMW   | Zero Mode Waveguide                            |

# **Chapter 1**

## **Introduction**

## 1.1 Introduction



Figure 1.1: Artist rendition of the Voyager spacecraft. *From NASA (67)*

Having left earth 33 years ago and now ten billion miles away from home, the Voyager spacecrafts are probing at the outer edge of our solar system. With only 23 Watts of radio transmitter power, Voyagers 1 and 2 are still returning scientific information about their surroundings through the Deep Space Network (67). To put these numbers into perspective: seen from our back yard, radio signal from the Voyagers is dimmer than a cell phone display on the moon<sup>1</sup>. Many engineering techniques have been used in listening to the faint whisper from the Voyagers. As we look into the microscopic world of single molecules, the same techniques applied to the far-and- beyond can be similarly used on the near-but-tiny. This dissertation is an attempt at adapting some of the signal processing techniques traditionally used in electrical engineering to fluorescence

---

<sup>1</sup>Assuming distance from Voyager 1 to the earth is  $\sim 117\text{AU}$  and from moon to the earth is  $0.0026\text{AU}$

microscopy.

## **1.2 Single Molecule Studies**

### **1.2.1 Motivation of Single Molecule Studies using Fluorescence Microscopy**

Apparent behavior from a large collection of molecules may not be completely understood if it is not possible to study individual molecules one, or a few, at a time. With advances in instrumentation, researchers can now observe and track single particles through time and space, record their behavior and their interaction with the environment. From the recorded information, the single molecule's basic physical, chemical, or biological properties can be obtained or deduced. In addition, with repeated observations of many particles, we can collect a statistical distribution of the properties we are interested in, which contains far more information than an ensemble measurement in which only an average is observable. Events that are rare will simply be averaged below the unobservable limit. It is especially true in a heterogeneous system, where single molecule measurements are needed to extract all the parameters. What's more, with improvements in both experimental hardware and software, single molecules can be observed and analyzed in real time, and separated based on one or several of their basic properties such as charge, mobility, and fluorescence, resulting in targeted isolation, separation, and characterization.

At this time, the optical approach is one of the mature technologies used

in studying single molecule dynamics, because the existence of a photon creates high contrast to back-ground, compared to for example electrical detection. However optical method has to overcome such technical barriers as fluorescence labeling, (fluorescence) background discrimination, and diffraction-limited far-field illumination. In this dissertation, we will focus our discussion on optical fluorescence microscopy in studying single molecules.

## 1.2.2 Signal Processing in Single Molecule Studies

The underlying principle of single molecule study is not fundamentally different from other disciplines in the physical sciences, or from the first human hunting down a rabbit with a stone: to the object of curiosity, we interrogate it with some form of energy, such as a burst of electricity, a beam of light, or a swinging baseball bat, and look for a response. The response may contain the information we look for, which we call signal. The response may also contain energies that we do not wish to collect, which we lump together with errors that may have been contributed from the methodology, the environment, and ultimately the observer, and call it noise. In short, the collected raw data contains both signal and noise, as shown in Fig. 1.2.

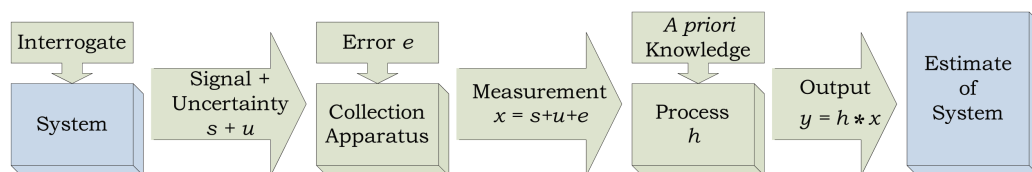


Figure 1.2: Block diagram of system estimation process. Due to uncertainty in measurement, an estimation of the state of a system is never the exact replica of reality.

To understand our object of interest, we would like to separate signal from noise, in other words, maximize the energy contained in the signal, and minimize that in the noise. The procedures performed on a signal in order to extract information, is called Signal Processing. Signal processing is performed to enhance the information contrast to noise, in order to obtain the best estimation of the system of interest. We stress here that what we obtain from our signal is at best an “estimation” of the system, and not necessarily the actual state of the system. The estimate can be made as close as possible to the actual system provided the noise energy can be made as small as possible compared to the redundancy in measurement.

### **1.3 Techniques to increase SNR in Single Molecule Studies**

Since the goal of “Single Molecule Study” is to study single molecule, the fundamental requirement is such that the signal energy obtained from single molecule is sufficiently high compared to noise energy, such that single molecule properties can be determined (61). This leads to two subsequent requirements: 1, there is only one molecule in the observation volume; and 2, after integration, signal energy is higher than noise energy.

#### **1.3.1 Limit the Number of Observable Molecules**

The average number of molecules  $N$  in a given volume  $V$  depends on the concentration  $C$ :

$$N = C \times V \tag{1.1}$$

Certainly the instantaneous number of molecules in a given volume  $V$  at any time  $t$  follows a Poisson distribution (see section 5.6.1), but to reduce average  $N$ , we can reduce concentration  $C$ , i.e, dilute analyte, or reduce observation volume  $V$ , for example using near-field optical techniques to bring probing volume really close to the single molecule (e.g, STM, AFM, NSOM, or FRET with membrane bound receptor), or a combination of these methods that reduce both the average concentration and observation volume.

### **Decrease Concentration**

There are two mechanisms to decrease analyte concentration. One is to physically increase separation between molecules, which is what we normally consider “dilution”; and the other is to chemically or optically make fraction of the analyte un-detectable.

**Physical Dilution** The most straight-forward way to decrease the number of observable fluorophores in a given volume is to dilute the sample. In a typical diffraction limited optical set up, a laser spot can be focused down to  $\sim 500\text{nm}$  diameter laterally and  $7\mu\text{m}$ . Concentration below  $100\text{pM}$  would result in less than one molecule per focal volume on average. However even the de-focused part of the laser beam can still excite fluorophores in bulk solution, though with less power, and still contribute to the fluorescence background.

**Opto-chemical Dilution using Switchable Fluorophores** With careful engineering of fluorescent molecule pairs, switchable fluorophores can be stochastically switched from dark state to fluorescent state. As long as the number of flu-

orescent molecules is relatively low, such that they are spatially distributed far apart, they can be distinguished from one another. This technique is often used together with Point-Spread-Function fitting to reconstruct ultra-high-resolution images (82).

### **Reduce Observation Volume**

There are two ways to reduce observation volume. One is to block out illuminated region of the sample – confocal microscopy is an example of physical blocking, STED is an example of optical blocking; the other is to limit excitation volume by using near field techniques, for example using ZMW, TIRF, or by mathematical probability multiplication such as two photon microscopy.

**Confocal Microscopy** Considered a far-field technique, confocal microscopy uses a diffraction limited laser spot to illuminate the sample. The region of interest however, is selected in the image plane using a small pin-hole (77). Light is therefore rejected from out-of-focus regions. This set up results in an approximate cylindrical observation volume, with  $500\text{nm}$  diffraction limited laser spot width, and  $2\mu\text{m}$  height limitation due to spherical aberration. With volume on the order of a femtoliter, confocal microscopy allows single fluorophore observation with up to nano-molar concentration.

Though the pin-hole at the image plane cuts down out-of-focus light, the confocal technique is still diffraction-limited, and has a larger observation volume compared to other near-field techniques such as NSOM. However confocal microscopy has several important advantages over near-field microscopy. First of all it allows large laser power to be used and hence more photons can be

collected within a small period of time. Secondly with synchronized scanning mirrors in the illumination and detection paths, confocal microscopes offer 3-dimensional sectional capability with non-invasive detection, which means it can image into reasonably thick cell or tissue sample and still obtain great resolution.

In Chapter 3, we use confocal microscopy to study cellulase binding to pre-treated wood particles.

**STED** Using technique called stimulated emission depletion (STED), Hell *et al* has demonstrated 4.5× improvement of resolution compared to diffraction-limited fluorescence microscopy. By using a second laser source to effectively induce transition and deplete most of the fluorophores from the excited state, fluorescence from the only remaining fluorophores are selected temporally for detection and constitute a super resolution image (28). Similar to other far-field fluorescence techniques, STED proves to be non-invasive and has been increasingly applied in the biological as well as in the material sciences (86).

**Two Photon Microscopy** Like confocal microscopy, two-photon microscopy is also a far-field technique that offers three-dimensional spatial resolution. Excitation probability increases quadratically with the photon intensity. Therefore out of focus excitation probability, and hence fluorescence intensity, drops off quickly, leading to an inherent small focal volume, defined by probability multiplication of two 3-dimensional Gaussian-like intensity functions (17, 106).

**Total Internal Reflection Fluorescence** In total internal reflection fluorescence microscopy set up, incoming excitation light beyond critical angle is completely reflected. However an evanescent wave exists at the substrate-liquid interface, providing enough energy to excite fluorophores that happens to be located in this  $\sim 100nm$  region, thus achieving optical confinement in one dimension. This method can be combined with other microscopy techniques to provide high resolution imaging. However it is often used for tracking molecules in a 2-dimensional bound surface such as membranes.

**Zero-Mode-Waveguides** Zero Mode Waveguides are sub-wavelength apertures milled in optically opaque film supported on fused silica substrate. These apertures are typically manufactured with diameters on the order of  $100nm$ . Evanescent field is established at the entrance of the waveguides if no propagating modes exist, resulting in zeptoliter observation volumes, allowing micromolar concentration fluorescence microscopy not achievable using either confocal or even TIRF. In fact ZMW technique is similar to that of NSOM, in that fluorophores are excited only when they are in the vicinity of the near-field of the optical excitation, however unlike NSOM, ZMWs are fixed relative to the sample, where as samples diffuse in and out of the focal volume, where as NSOM tip can be scanned across the sample and search for regions of interest.

**NSOM** Like ZMW, a diffraction-limited illumination volume can be achieved using near-field optics, where optical energy is guided via an optical fiber, and aluminum coating at the tip of the fiber restricts scattered light and reduces background illumination into the sample (98). A non-scanning version of NSOM devices base off dielectric-filled ZMWs have been introduced recently

to study membrane-bound diffusers (39).

**Other Techniques** Single molecule spectroscopy, for example used in fluorescence resonance energy transfer or FRET, is often achieved by confocal detection or by excitation with an evanescent wave generated by total internal reflection. Furthering these two techniques, that is, excitation using an evanescent wave while detecting using a confocal set up, is achieved by Zero-Mode-Waveguides, which we discuss in detail in Chapter 4.

### 1.3.2 Integrate to Utilize Redundancy

When we have done due diligence and minimized observation volume, minimized background fluorescence, cooled our cameras to reduce electronic noise, what else can we do to increase signal to noise ratio and make our estimate  $\hat{x}$  approach  $x$  with infinitesimal error?

Fig. 1.2 suggests that we can use *a priori* information in aid of signal integration, and utilize redundancy in signal to help increase signal-to-noise ratio after integration. Since redundancy is correlated with the signal, and noise is uncorrelated, therefore after averaging or integration, signal is enhanced with respect to uncorrelated noise.

Examples of redundancy in language can be readily found. For example the sentence:

“Helo world.”

is easily interpreted as “Hello world.” by most readers familiar with the English language, despite the missing letter “l”. There is enough redundancy built into this phrase for us to use our prior knowledge that “helo” is not an English word, whereas “Hello” is. Similarly, fluorescence microscopy can utilize redundancy in increasing signal to noise ratio, provided we have prior information as to how to correctly interpret and utilize the redundant signals.

**Integrate All Photons** A single fluorophore can emit  $10^5 \sim 10^6$  photons before photo bleaching. While the overall detection efficiency of ultra sensitive optical system allows 5% photons to be converted into electronic pulses, thus representing 5000 – 50000 photons per single fluorophore before photo bleaching (70). Although most of the time we do not illuminate a fluorophore until it bleaches, we would like to collect as many photons as possible. In spatially locating a fluorophore, the uncertainty of a fluorophore’s position decreases with the increase of  $\sqrt{N}$  where  $N$  is the number of collected photons.

In a technique called fluorescence imaging with one-nanometer accuracy (FIONA), more than 10,000 photons can be collected from a single fluorescent molecule and its image fit to a point-spread-function, resulting in uncertainty of the fluorophore’s localization on the order of  $1nm$  (110). Here not only was redundancy used (large number of photons), *a priori* knowledge is also applied that the detected image can be fit to a Gaussian point-spread function such that the centroid of the function is taken as the location of the fluorescence emitter.

As we can see in super resolution microscopy, the number of photons is important in reducing uncertainty, and hence improving resolution of the image. To collect more photons, ultra-sensitive avalanche photodiode can be used

where possible in place of CCD cameras;  $4\pi$  collection has been used to double the number of photons collected (27); Oxygen reducing agents can be used in buffers to increase fluorescence life time of fluorophores before photo bleaching, as well as reducing triplet state (99, 100).

Whereas FIONA takes advantage of the fact that fluorophores are spaced so far apart that only one fluorophore exists in the region of interest, its point-spread-function fitting routine cannot be applied directly to complex images. Because complex images contain large number of fluorophores. Sub-diffraction-limit imaging by stochastic optical reconstruction microscopy (STORM) overcomes this difficulty by using switchable fluorophores to randomly increase the separation and lower the concentration of fluorescent molecules in the field of view, allowing reconstruction of sub-diffraction limit optical images of complex structures (82).

In STORM, we see a combination of increasing redundancy, i.e, increase signal and reducing concentration, i.e, reducing uncertainty or noise, in order to increase signal to noise ratio.

## **1.4 Maximize Signal Energy by Temporal or Spectral Integration**

The methods, spectral deconvolution and matched filtering, described in Chapter 2 and demonstrated Chapter 3 and 5 follow the general principle that all usable photons should be integrated in order to get the best estimate of the system.

Spectral deconvolution uses the fact that fluorescence emission has a spread in the optical spectrum, and in multi-color optical detection systems, photons emitted from one fluorescent species may fall into several color channels. Re-combining signals from multiple color channels allows us to correctly quantify fluorophore concentration.

Whereas FIONA fits a point-spread-function in the spatial domain, matched filtering fits a similar photon distribution function in the time domain. This method is used to identify stochastic single molecule events in nano-interrogation devices such as nanofluidic channels and Zero-Mode-Waveguides. We will describe these two methods in detail in the next chapter.

## **Chapter 2**

# **Signal Processing Techniques Used in Single Molecule Studies**

## 2.1 Introduction

Although spectral deconvolution and matched filtering techniques seem quite distinct, the underlying principle is the same: integrate as much signal energy as possible, and reject as much noise energy as possible. In spectral deconvolution, one fluorophore's emission is collected in multiple detection channels, partially overlapping with another fluorescent species' emission and collection bands. Linear transformation converts photon energy from each collection channel and attribute them to their rightful emitter. Though seldom necessary in fluorescence imaging that examines the existence of a fluorophore, this technique is essential when quantitative fluorescence microscopy is used to enumerate fluorescent molecule accumulation, for example, as we applied later in Chapter 3.

Matched filtering, unlike spectral deconvolution which operates in the spectral domain, uses temporal information to enhance signal to noise ratio. Its development and application can be traced back to the emergence of radar technology in World War II (71). The general idea is to base one's interpretation of information on all of the energies collected, where redundant energy helps to enhance signal to noise ratio, and has roots deep in our languages.

Although both methods estimate the state of a system, the difference between these two methods is the selection model that is based on *a priori* knowledge. For spectral deconvolution, the spectrum of each fluorophore is deterministic and does not change from measurement to measurement. On the other hand, the selection model for matched filter is based on an ensemble average of large number of stochastic events, and therefore is a maximum likelihood

model.

## 2.2 Spectral Deconvolution

Fluorescence microscopy has been used to monitor protein activity *in vivo* and *in vitro*. In most cases, the actual number of fluorophores is not as important as verifying the existence and the kinetic activities of proteins. But in quantitative fluorescence microscopy, the fluorescence intensity represented by fluorophores is a direct measure of either enzymatic activity, or binding of labeled ligands. For example in our study of cellulase binding to cellulose, the rate of fluorescently-labeled cellulase binding to immobilized substrates was inferred from the observed fluorescence increase, it was essential to separate label fluorescence from other fluorescence sources. In many cases, careful selection of fluorescence emission filters would be adequate in discriminating the two, giving excellent qualitative, if not quantitative, description of fluorophore distribution (65). However, to obtain meaningful numerical values of fluorophore concentration, spectral deconvolution is needed. Knowing the spectral shape of each fluorochrome in the system, and knowing the photon collector response to the rise of fluorescence signal (the simplest being a linear response), fluorophore concentration can be back-calculated from collected photons. As will be seen later, knowing the rate of change in collected fluorescence signal is sufficient in estimating binding coefficients.

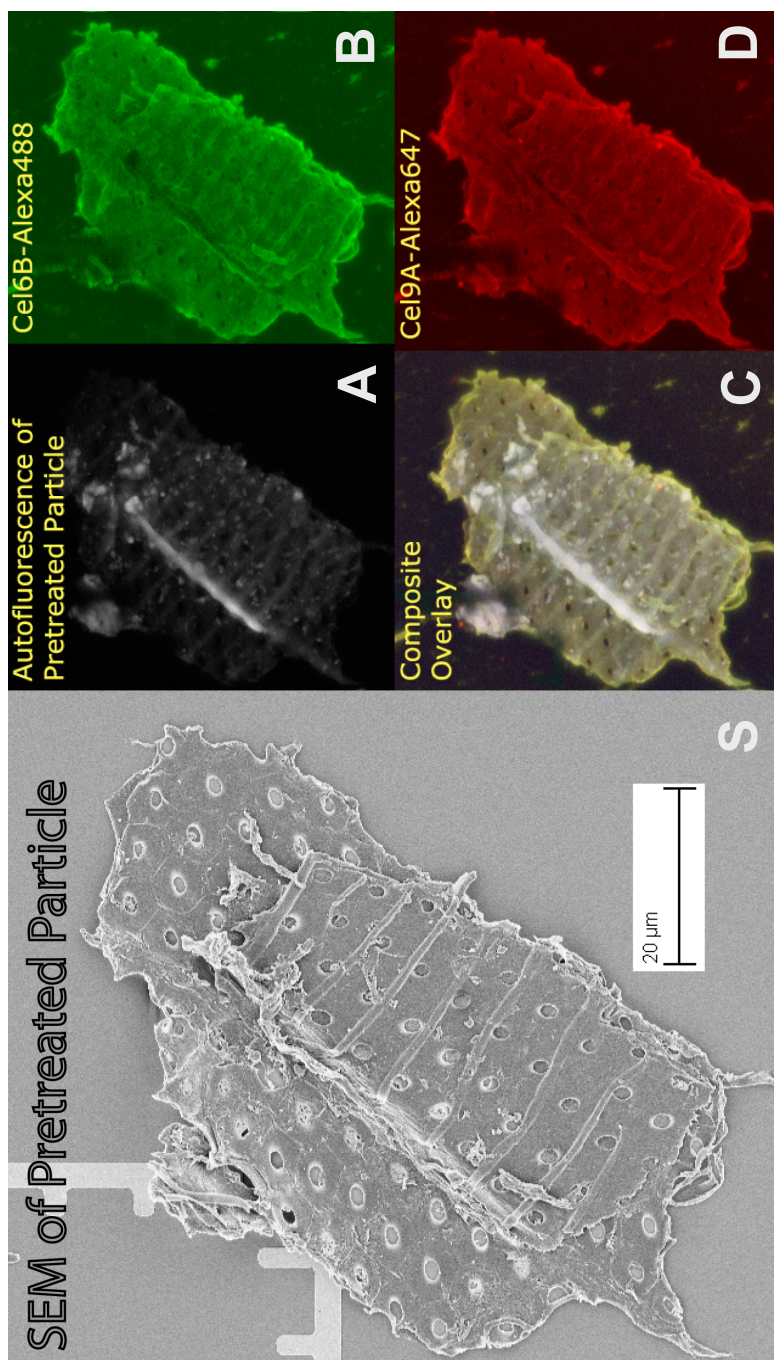


Figure 2.1: Sample image of a wood particle incubated with Alexa-488 labeled Cel6B and Alexa-647 labeled Cel9A.

### 2.2.1 Motivation: Spectra Bleed-Through

Fig. 2.1 provides an illustrative example of labeled enzyme binding to an autofluorescent wood particle substrate. From the SEM image of a wood particle (left), we can clearly distinguish the edge of the particle, with rich binding sites for cellulases, and lignin-rich hemicellulose region in the middle, where fibers are seemingly bundled up into nodules. It is in these lignin-rich region that we find the highest autofluorescence, whereas the edges of the particle attract more labeled cellulases. However it does not mean cellulases do not bind to the lignin-rich region. As we will see in Chapter 3, separating autofluorescence of particle is essential in determining binding rate of cellulase enzymes.

Pre-treated wood particles have strong autofluorescence when excited with a 488nm laser, as we can see in Figure 2.2 which shows the spectral signature of pretreated wood, and AF488, when excited with a 488nm laser. We see there is significant overlap of the two. In addition, the emission tail of pre-treated wood particles extends to the range of AF647 emission spectrum (not shown). Therefore if used without processing, raw fluorescence intensity would introduce considerable error due to spectral cross-talk in quantitative fluorescence microscopy.

### 2.2.2 Quantitative Fluorescence Microscopy

When measuring fluorescence in bulk, the collected fluorescence intensity  $I^{PMT}$  by a photo multiplier tube (PMT) is a function of excitation light intensity  $I^{EX}$ , number of fluorophores  $n$  in the focal volume, the average extinction coefficient  $\sigma$  of each fluorophore, quantum yield  $\phi^f$  of the fluorophore, collection efficiency

of the optical system  $\eta$ , transmission properties of the emission band-pass filter  $T^{BP}$ , and quantum yield  $\phi^{PMT}$  of the PMT, written as,

$$I^{PMT} = I_{EX} \cdot \sigma \cdot n \cdot \phi^f \cdot \eta \cdot T^{BP} \cdot \phi^{PMT} \quad (2.1)$$

Fluorescence is the emission of a photon during electronic transition from the first excited singlet state to the ground singlet state after optical excitation. The photon energy is equal to the difference between the lowest vibrational level of the excited state and the vibrational level of the singlet ground state

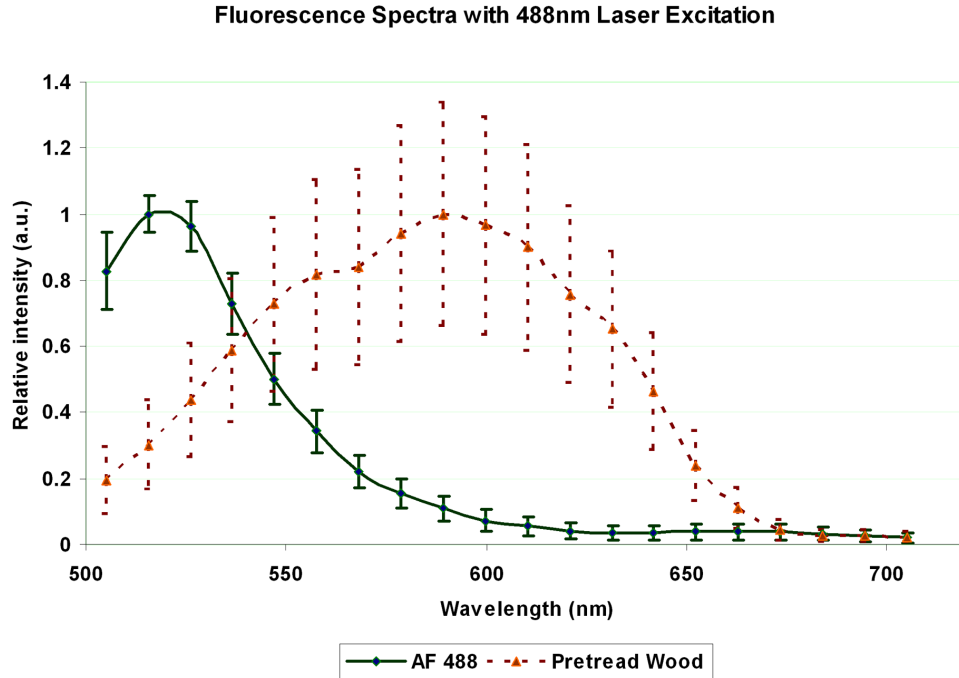


Figure 2.2: Normalized emission curves of AF-488 and pre-treated wood particles when excited with 488nm laser. Fluorescence spectra were taken with Leica TCS SP2 Confocal laser scanning microscope (Leica Microsystems, GmbH, Wetzlar, Germany) with prism and variable slit, recording emission from 500nm to 700nm at 10nm steps and 10nm spectral bandwidth. Data and error bar at every wavelength are average and standard deviation of pixel values of the image for that wavelength, respectively.

(58). Therefore the emission spectrum of a fluorophore does not depend on the number of its species,  $n$ , or the intensity of the excitation beam. In other words, holding constant excitation light intensity  $I^{EX}$ , and maintaining physical environment of the fluorophore and hence maintaining a constant  $\sigma$  and  $\phi^f$ , the following equation for the collected fluorescence intensity is obtained for each optical system set up (i.e, same microscope objective),

$$I^{PMT} = \alpha \cdot n \quad (2.2)$$

where

$$\alpha = I^{EX} \cdot \sigma \cdot \phi^f \cdot \eta \cdot T^{BP} \cdot \phi^{PMT} \quad (2.3)$$

If there are two species of fluorophores  $n_1$  and  $n_2$ , being illuminated simultaneously, and their fluorescence collected by two photon collection channels, separated by distinct emission band-pass filters, each PMT observes an intensity given by

$$\begin{bmatrix} I_1^{PMT} \\ I_2^{PMT} \end{bmatrix} = \begin{bmatrix} \alpha_{11} & \alpha_{12} \\ \alpha_{21} & \alpha_{22} \end{bmatrix} \cdot \begin{bmatrix} n_1 \\ n_2 \end{bmatrix} \triangleq \mathbf{A} \cdot \begin{bmatrix} n_1 \\ n_2 \end{bmatrix} \quad (2.4)$$

where we have defined the cross-talk matrix  $\mathbf{A}$  that completely describes the distribution of fluorescence signal from each fluorophore species into either photon collection channels. Each matrix coefficient  $\alpha_{ij}$  is

$$\alpha_{ij} = I^{EX} \cdot \sigma_j \cdot \phi_j^f \cdot \eta_i \cdot T_{ij}^{BP} \cdot \phi_i^{PMT} \quad (2.5)$$

where  $i$  denotes collection channel number, and  $j$  a fluorophore species. Since each fluorophore's emission spectrum covers a range of wavelengths, depending on the bandpass filter used in each optical path, the off-diagonal elements of  $\mathbf{A}$  may not vanish, which results in signal bleed-through.

To accurately discern the number of bound enzymes, it is necessary to determine each individual element  $\alpha_{ij}$  and calculate the number  $n_j$  from  $I_i^{PMT}$  using the relationship

$$\begin{bmatrix} n_1 \\ n_2 \end{bmatrix} = \mathbf{A}^{-1} \cdot \begin{bmatrix} I_1^{PMT} \\ I_2^{PMT} \end{bmatrix} \quad (2.6)$$

Commercially available software abound to do spectral deconvolution with known fluorophores and system set up. With uncharacterized fluorophores or a custom optical system, it is necessary to measure  $\alpha_{ij}$ . To find  $\alpha_{11}$  and  $\alpha_{21}$ ,  $I_1^{PMT}$  and  $I_2^{PMT}$  are measured with a known  $n_1$  while  $n_2$  is set to 0.  $\alpha_{12}$  and  $\alpha_{22}$  can be found in similar fashion with known  $n_2$  and holding  $n_1 = 0$ . This method can be easily expanded into multi-channel, multi-fluorophore system, as long as  $\mathbf{A}$  is not singular.

### 2.2.3 Demonstration of Spectral Deconvolution

**Determine Linear Range** To determine the range of fluorescent signals we could safely take without saturating photo detectors, we characterized the CLSM using Alexa Fluor 488-5'-dUTP and Alexa Fluor 647-5'-dUTP (Molecular Probes, Eugene OR) at various concentrations. From these measurements shown in figure 2.3, we determined that for a 12-bit image with maximum pixel value of 4095, pixel intensities below 3500 were seen to be linearly related to fluorophore concentration (79), a necessary condition for spectral deconvolution using linear transformation.

**Spectra Separation** Since AF-labeled cellulase binding was inferred from observed temporal fluorescence increase on immobilized substrates, it was essential that we completely separate AF488/647 fluorescence from wood autofluorescence, that is, obtain the coefficients in cross-talk matrix  $\mathbf{A}$ , which in this case, is a  $3 \times 3$  matrix.

Fluorescence emissions from Alexa-fluorophore labeled enzymes, as well as that of wood particles' autofluorescence, were collected in three discrete channels, separated by emission filters 505-525nm, 560-620nm, and 655-755nm, as seen in Fig. 3.1. By measuring signal outputs from each channel with one fluorochrome species at a time, we calculated each fluorophore's spectral distribution in each collection channel, as shown in Fig 2.4. Using this result, we estimated and corrected for spectral bleed-through in fluorescence images taken

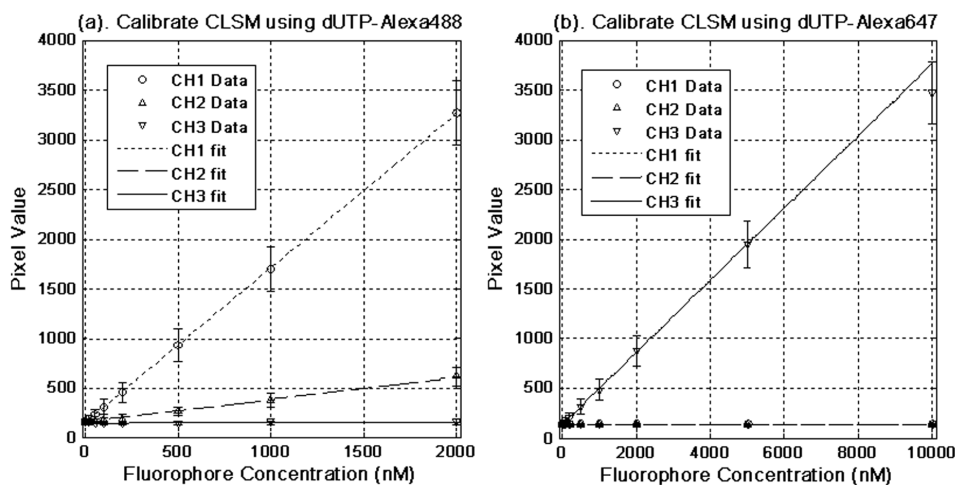


Figure 2.3: Determining linear range of CLSM system by imaging (a) 5'-dUTP-Alexa 488 and, (b) 5'-dUTP-Alexa 647 fluorophores at concentrations between 20nM and 10 $\mu$ M, with excitation lasers at 488nm, 543nm and 635nm all set at 2% of respective maximum power levels. For a 12-bit image, pixel intensities less than 3500 are assumed linearly correlated with fluorophore concentration.

with all three fluorochromes.

For our system, the cross-talk matrix used in spectral deconvolution was found to be:

$$\mathbf{A} = \begin{bmatrix} 0.87 & 0.14 & 0 \\ 0.13 & 0.52 & 0 \\ 0 & 0.34 & 1 \end{bmatrix} \quad (2.7)$$

We demonstrate the utility of spectral deconvolution in Chapter 3, where we studied the adsorption rate of fluorescently labeled cellulases to pretreated

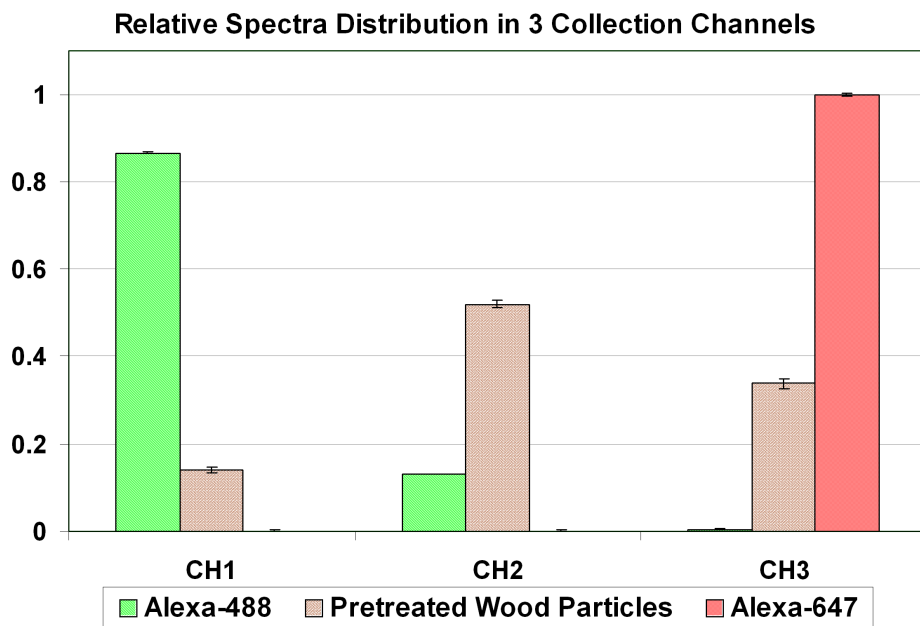


Figure 2.4: Relative spectral intensity distribution of Alexa-488, autofluorescence of pretreated wood, and Alexa-647, in three collection channels. The actual numerical values form the cross-talk matrix elements  $a_{ij}$  of  $\mathbf{A}$ , and is used in spectral separation to recover each fluorophore's concentration, and deduce the amount of bound enzymes

wood particles.

## **2.3 Matched Filtering**

### **2.3.1 Where Do We Need Matched Filtering**

In single molecule discrimination experiments using nanofluidic channels, such as single molecule sorting, voltage switching decision is made upon the detection of the presence of a molecule. Presence of a molecule is detected by the fluorescence signal from avalanche photo diode. However often times the detected fluorescence signal is rather low, and decision has to be made on only a few or tens of photon collected within the sub-millisecond period of molecule transition through illumination volume. We find ourselves in the situation similar to those engineers working on the first generation of radar defense system: determine whether a faint radar signal constitute a remote aircraft. In 1943, North proposed the concept of “Integration after Detection” as opposed to “Detection after Integration”, and demonstrated its advantage of maximizing the signal to noise ratio on a system with known signal period (71). His research laid the foundation of theoretical development of matched filtering that is ubiquitous in today’s communication devices.

### **2.3.2 Problem Definition**

In fluorescence study using nano interrogation devices such as nanofluidic channels or ZMWs, when there is no fluorescent molecule in the focal volume,

the reported photon pulses are from:

1. Reflected excitation light that is not completely blocked by emission filter. This contributes the majority of extra photon counts;
2. Dark count of APD, which is pretty rare at approximately 100 counts per second, or fewer than one per single molecule transition period, which is on the order of  $1ms$ ;
3. Ambient light, which is rather low and negligible if we keep the optical detection area well shielded;
4. Autofluorescent species in solution and fluorescent molecules in bulk solution that are excited by scattered illumination laser

Fluorescent signals from items listed above constitute a semi-constant noise background that we can attempt to reduce, but not completely remove. As a fluorescent molecule comes through the focal volume, we will need to discriminate a burst of photon pulses from noisy background and make a decision on whether the photon burst constitute a real molecule transition event.

For simplicity, we lump the background noise into a stationary random process  $n(t)$  with a constant mean and standard deviation  $\sigma$ , and define its average power as  $E[nn^\dagger] = R_n$ , where the  $(\dagger)$  denotes a hermitian operator. For real  $n$ ,  $n^\dagger$  is simply its transpose.

In mathematical form, the APD output can be written as:

$$x(t) = s(t) + n(t) \tag{2.8}$$

where  $s(t)$  is the burst of photon pulse due to fluorescent molecule of interest.

Our goal is to process  $x(t)$  and correctly identify the occurrence of single molecule events that produce  $s(t) > 0$  while minimizing the probability of error.

### 2.3.3 Matched Filter and Cauchy-Schwarz Inequality

Let's denote the linear process we subject  $x(t)$  to as  $h(t)$ . The output  $y(t)$  of such process can be written as:

$$y(t) = h(t) * x(t) = h^\dagger x = h^\dagger s + h^\dagger n = y_s + y_n \quad (2.9)$$

where  $*$  denotes convolution in the time domain, and  $h^\dagger$  is the hermitian conjugate transpose of  $h$ <sup>1</sup>. Our goal is to design  $h$  so as to maximize the signal-to-noise-ratio of  $y(t)$ .

The signal-to-noise ratio (SNR) of the output signal,  $y(t)$ , is

$$\text{SNR}_{\text{out}} = \frac{|y_s|^2}{E[|y_n|^2]} = \frac{|h^\dagger s|^2}{E[|h^\dagger n|^2]} \quad (2.10)$$

We rewrite the denominator as:

$$\begin{aligned} E[|h^\dagger n|^2] &= E[(h^\dagger n)(h^\dagger n)^\dagger] \\ &= E[h^\dagger n n^\dagger h] \end{aligned} \quad (2.11)$$

and  $h$  is not stochastic and can be moved outside of the expectation operator:

$$\begin{aligned} E[|h^\dagger n|^2] &= h^\dagger E[n n^\dagger] h \\ &= h^\dagger R_n h \\ &= h^\dagger (R_n^{1/2})^\dagger R_n^{1/2} h \\ &= (R_n^{1/2} h)^\dagger (R_n^{1/2} h). \end{aligned} \quad (2.12)$$

---

<sup>1</sup>Since integration is a linear operation, we write it in matrix multiplication form, where  $h$  can be of infinite dimension. In practice however,  $h$  is truncated, making it a finite impulse response (FIR) filter.

Similarly, we rearrange the numerator:

$$\begin{aligned}
|h^\dagger s|^2 &= |h^\dagger \cdot \mathbf{1} \cdot s|^2 \\
&= |h^\dagger (R_n^{1/2})^\dagger (R_n^{-1/2}) s|^2 \\
&= |(R_n^{1/2} h)^\dagger (R_n^{-1/2} s)|^2
\end{aligned} \tag{2.13}$$

So we have

$$\begin{aligned}
\text{SNR}_{\text{out}} &= \frac{|(R_n^{1/2} h)^\dagger (R_n^{-1/2} s)|^2}{(R_n^{1/2} h)^\dagger (R_n^{1/2} h)} \\
&\leq \frac{[(R_n^{1/2} h)^\dagger (R_n^{1/2} h)][(R_n^{-1/2} s)^\dagger (R_n^{-1/2} s)]}{(R_n^{1/2} h)^\dagger (R_n^{1/2} h)} \\
&= s^\dagger R_n^{-1} s
\end{aligned} \tag{2.14}$$

where we have used Cauchy-Schwarz inequality  $\|\mathbf{A} \cdot \mathbf{B}\|^2 \leq \|\mathbf{A}\|^2 \|\mathbf{B}\|^2$ , where equality holds only if  $\mathbf{A} = \alpha \mathbf{B}$ . Here  $\mathbf{A} = R_n^{1/2} h$ ,  $\mathbf{B} = R_n^{-1/2} s$ .

Therefore the upper bound of SNR is achieved only if  $R_n^{1/2} h = \alpha R_n^{-1/2} s$ , or  $h \equiv \alpha R_n^{-1} s$ , where  $\alpha$  is some constant. In words, the shape of the filter  $h$  in time domain should match the temporal shape of the photon pulse  $s(t)$ .

### 2.3.4 The Adaptive Filter

Now that we know the impulse response of the filter needed to maximize SNR is the signal itself. But without the signal, we cannot obtain the filter. That is, without the result in Fig. 1.2, we do not have the *a priori* knowledge required in Fig. 1.2 to control the estimation process. It is thus a convoluted process. Fortunately, an autocorrelation function  $G(\tau)$  of  $x(t)$  can be calculated. Since noise  $n(t)$  is uncorrelated to  $s(t)$ , signal and noise is separated in  $G(\tau)$ . Therefore we can use autocorrelation to obtain an average of  $\langle s(t) \rangle$ , and then build a matched filter  $h(t) = \langle s(t) \rangle$  normalized to integral 1.

**Wiener-Khinchin Theorem** Wiener-Khinchin Theorem states the Fourier Transform <sup>2</sup> of an autocorrelation of a signal is the square of the Fourier transform of the signal. A quick proof for the general case of a complex signal is given below.

Given complex signal  $x(t)$  and its complex conjugate  $x^*(t)$ , we can calculate its autocorrelation function  $G(\tau)$  as

$$G(\tau) = \int_{t=-\infty}^{\infty} x^*(t)x(t + \tau)dt \quad (2.15)$$

The Fourier transform  $\mathcal{F}$  of  $G(\tau)$  is

$$\begin{aligned} \mathcal{F}[G(\tau)] &= \int_{\tau=-\infty}^{\infty} G(\tau)e^{i2\pi\nu\tau} d\tau \\ &= \int_{\tau=-\infty}^{\infty} \int_{t=-\infty}^{\infty} x^*(t)x(t + \tau)e^{i2\pi\nu(t+\tau)}e^{-i2\pi\nu t} dt d\tau \\ &= \hat{x}^*(\nu)\hat{x}(\nu) \\ &= |\hat{x}(\nu)|^2 \quad \text{or,} \end{aligned} \quad (2.16)$$

$$\mathcal{F}[G(\tau)] = |\mathcal{F}[x(t)]|^2$$

Since our signal  $x(t)$  is real, we do not have to worry about complex conjugates. In addition, since both the signal  $x(t)$  and its autocorrelation  $G(\tau)$  are even functions with respect to time 0, both Fourier transforms are real functions (112).

Therefore, we recover  $x(t)$  from  $G(\tau)$  by

$$x(t) = \mathcal{F}^{-1} \left\{ \sqrt{\mathcal{F}[G(\tau)]} \right\} \quad (2.17)$$

---

<sup>2</sup>Fourier transform is a coordinate transformation method in mapping a signal from time domain to frequency domain, or vice-versa. In equation form, it is

$$\hat{x}(\nu) \equiv \mathcal{F}[x(t)] = \int_{t=-\infty}^{\infty} x(t)e^{i2\pi\nu t} dt$$

### 2.3.5 Implementation

**Obtaining Autocorrelation Function** Autocorrelation function is obtained using digital correlator box (correlator.com). Experimental results provides correlation function of time span from  $0.1\mu s$  to tens of seconds or more, sufficient to cover our time frame of interest which is empirically determined to be on the order of milliseconds.

**Implementing Signal Shape Recovery in MATLAB** However when performing Discrete Fourier transform with Matlab, we need to take care in dealing with the phase terms, as the Fast Fourier Transform (FFT) routine in Matlab utilizes discrete signal representation and uses indices from 1 to  $N$ .

In Matlab, the functions `fft(x)` and `ifft(X)` calculate the Fourier transform pair for a vector  $x$  of given length  $N$  by using (59)

$$X(k) = \sum_{j=1}^N x(j)e^{-2\pi i(j-1)(k-1)/N} \quad (2.18)$$

$$x(j) = \frac{1}{N} \sum_{k=1}^N X(k)e^{2\pi i(j-1)(k-1)/N} \quad (2.19)$$

This assumes the continuous time signal  $x(t)$  is approximated by its  $N$  discrete time samples between  $0 \leq t < T$  with

$$x(t) \approx \sum_{j=1}^N x(j\Delta t)\delta(t - j\Delta t) \quad (2.20)$$

where  $\Delta t = T/N$ . However when time reference is left-shifted, such that  $-T/2 < t < T/2$ , the discrete samples,  $x(j)$ , are written as

$$x(t) \approx x(j) = \sum_{j=1}^N x((j - N/2 - 1/2)\Delta t)\delta(t - (j - N/2 - 1/2)\Delta t) \quad (2.21)$$

Therefore when performing FFT in Matlab, we need to cancel out the extra phase factor of the  $N/2$ -shifted signal by multiplying each term with  $e^{i\pi k(1+1/N)}$ . Note this is true for both even and odd  $N$ .

## 2.3.6 Results

### Photon Burst Reconstruction

We demonstrate the utility of this algorithm by testing several functions, shown in Fig. 2.5. It is interesting to note that even the shape of the original pulse is quite different, for example in Fig. 2.5.A and B, their autocorrelation functions are very similar. Therefore if we perform matched filtering solely based on the width of the autocorrelation function, we will either miss a lot of signal detail, or include much extraneous noise. In addition, as seen in Fig. 2.5.C, since cosine functions form a basis for all even functions, we conclude this signal recovering algorithm can be applied to all (assumed to be) even signal shapes.

### Reducing Noise and Enhancing Signal

**Results** Previously reported photon burst experiments have used various methods for signal recognition, for example binning at different widths (92), or using a weighted sum method (47), or similar to our method, utilizing a bin size that is correlated to the autocorrelation function (91). Here we have demonstrated a rigorously derived method that maximizes the SNR with a matched filter that is based on autocorrelation result.

While our method identifies photon bursts, it also acts as a low-pass filter

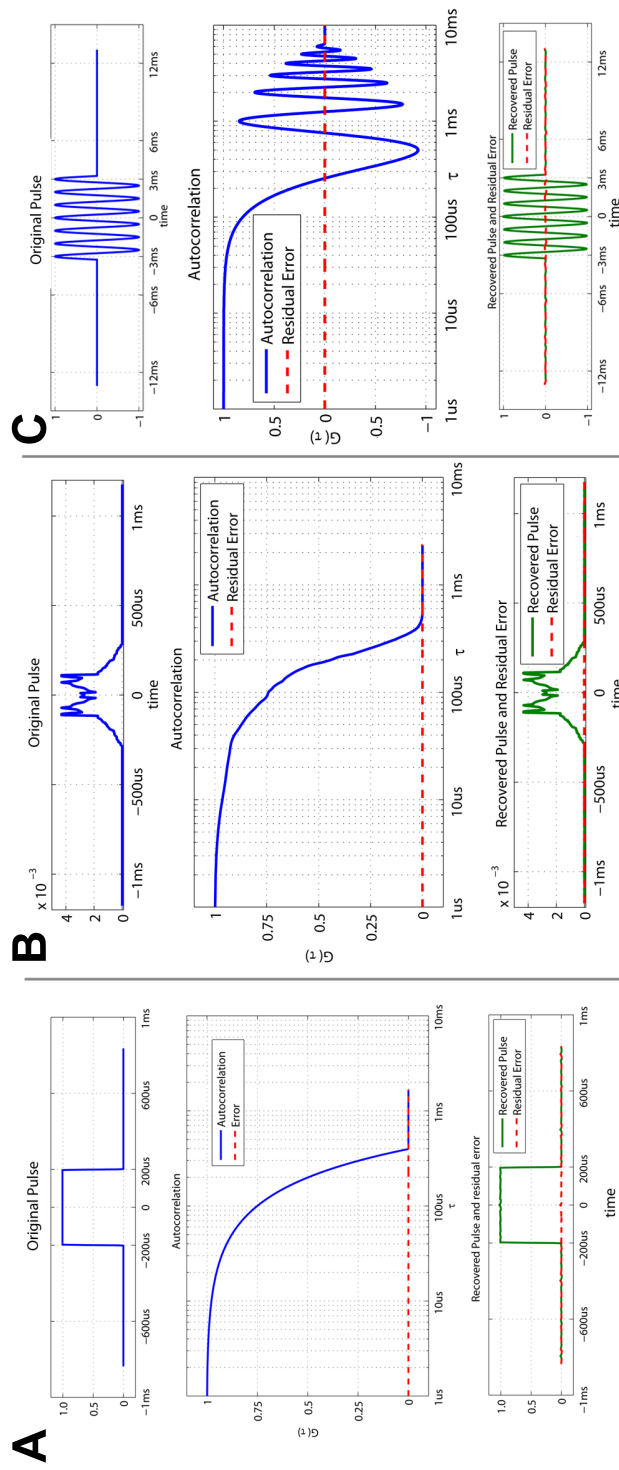


Figure 2.5: We test the pulse-recovering algorithm with a A. square wave, B, arbitrary wave and C, cosine wave. Their autocorrelation functions are first generated and Fourier Transformed to generate the energy spectra. Subsequent inverse Fourier Transform of the square root of the energy spectra reproduces the original pulse shape.

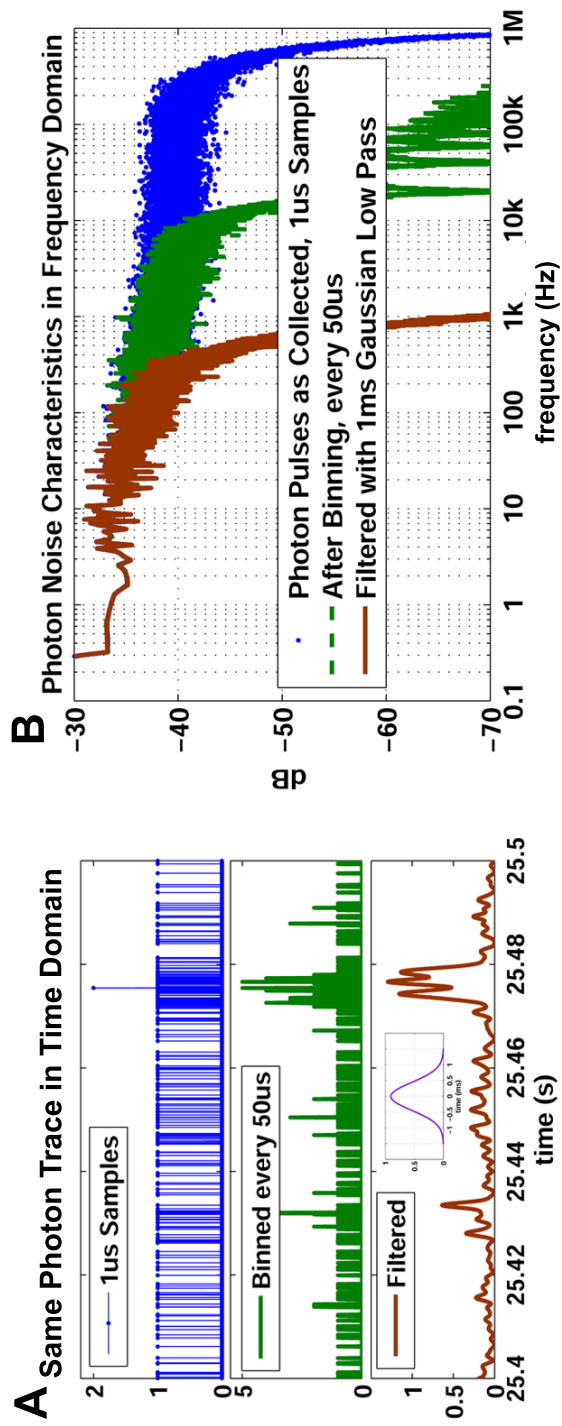


Figure 2.6: Sample photon spectral analysis with and without binning and filtering.

and reduces noise bandwidth and hence noise power considerably. From Fig. 2.6, we see the original spectrum of APD output, binned to  $1\mu s$ , has very broad spectral content in the frequency domain. In the time domain, we cannot tell directly from the raw photon data where exactly the single molecule event has occurred. After binning photons at  $50\mu s$  intervals, the spectrum has much narrower bandwidth, and we can see the result in time domain, as photons are added together. The best result is after matched filter has been applied, where we see noise has been suppressed in the frequency domain where the bandwidth is only wide enough to allow relatively slow single molecule events to pass, and restrict high frequency noise. In the time-domain, the noise is suppressed to the background level, and we can easily distinguish single molecule events from the noise background.

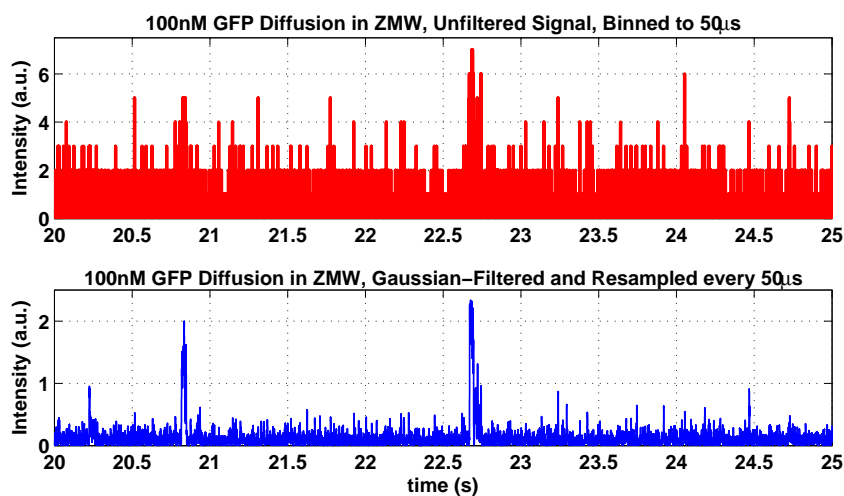


Figure 2.7: Sample photon trace and intensity trace as result of filtering.

Again we emphasize here that our assumption of the pulse shape is that the pulse has to be temporally symmetric. However in reality the single molecule event does not necessarily produce a symmetrical pulse. In nanofluidic chan-

nels, the photon burst follows the illumination spot shape, which is approximately Gaussian and symmetrical, ignoring photo bleaching. However in Zero-Mode-Waveguides, since the transition path of single molecule does not follow and predictable track inside the aperture, there is no guarantee that peak illumination and photon burst will happen at the center of the single molecule event. On average however, the expected photon burst shape should be Gaussian, as dictated by law of large numbers. In addition, the matched filter enhances events of the most likely pulse duration, and suppresses high frequency noise, and is therefore still useful for lifting signal above noise.

And we can see from Fig. 2.7, our matched filtering method also works well for single molecule events detected in ZMWs. We demonstrated the utility of this structure and filtering method in chapter 5, where we study GFP aptamer interaction with GFP.

## Chapter 3

# Real-time Observation of Cellulose Enzyme Binding to Pretreated Wood Particles <sup>1</sup>

---

<sup>1</sup>Part of this chapter has been published in *Cellulose*: Volume 18, Issue 3 (2011), Page 749, doi:10.1007/s10570-011-9506-2

### 3.1 Introduction

Cellulose is a major structural component of plant cell-walls, representing approximately half of its mass (7). As part of the natural carbon cycle, the cellulose content of trees and plants is depolymerized by fungi and bacteria to yield sugars for cell growth and metabolic activity. Nature has engineered a number of approaches to deconstruct plant cell walls. This includes the evolution of exoglucanases that depolymerize cellulose from the reducing and non-reducing ends and endoglucanases that attack along the cellulose chain (107). These molecular machines can bind and hydrolyze insoluble cellulose in both random and processive modes (10). Expanding our understanding of how these enzymes bind and hydrolyze cell-wall polymers is an important research and development activity for developing biotechnology approaches for producing fermentable sugars that can be converted into biofuels and bioproducts.

*Thermobifida fusca* produces several extracellular enzymes including cellulases that can hydrolyze cellulose and hemicellulose (54). The binding and the subsequent hydrolysis of cellulose by *T. fusca* cellulases have been extensively studied by a number of methods, many of which involved model substrates such as avicel or bacterial microcrystalline cellulose (BMCC) (36–38). The majority of these methods involves measuring bulk reaction products, whereas the heterogeneous reaction takes place on arrays of densely packed cellulose polymers with a width of 3 to 5 nm and length on the order of a few hundred nanometers (85). To gain access to these microfibrils, cellulases and other cell wall degrading enzymes must diffuse into fibrils with porous structures ranging from nano- to micro-scale. Thus, any effort to resolve cellulase binding, mobility and synergistic interactions must provide nano-scale resolution of the

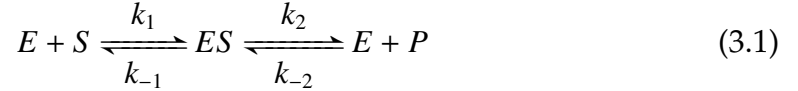
behavior of these interesting molecular machines. Recently, fluorescence microscopy was used to observe temporal cellulase binding to micro-patterned BMCC substrate (63). In the present study of cellulase binding to pretreated wood particles, time-lapse CLSM was used to explore the adsorption of three *T. fusca* cellulases to lignocellulose substrates.

These three cellulases represent three modes of attack to cellulose: Cel5A is a classical endocellulase, Cel6B is a classical exocellulase, and Cel9A is a processive endocellulase (107). Both Cel5A and Cel6B contain a family II cellulose binding module (CBM), whereas Cel9A consists of a fibronectin III-like domain, a family II and a family IIIc CBMs, in addition to a catalytic domain (37, 72). Using three cellulases provides the possibility to study different kinetics of adsorption and diffusion into the porous structures of the substrate. Coupling these cellulases with two labeling fluorophores allows for future studies of synergistic cellulose binding and hydrolysis.

CLSM is typically used to examine micrometer-sized particles or cells, where high spatial resolution is desired. Using a confocal aperture, CLSM reduces the fluorescence signal from outside the focal volume, hence making it an effective tool for imaging cross-sections of thick material, enabling the reconstruction of 3-dimensional fluorescence distribution patterns, and giving better resolution compared to epi-fluorescence imaging techniques. Here we use CLSM to take cross-section images of pretreated wood particles immersed in fluorescently labeled cellulase solutions. Preferential binding of cellulases to certain areas of the pretreated material was observed. The time-course fluorescence intensity data provided quantitative measure of bound enzymes over time, and were fit to a transient enzyme binding model.

### 3.2 Transient Enzyme-Binding Model

When an enzyme  $E$  is added to its substrate  $S$ , the two form an enzyme-substrate complex  $ES$  before the enzyme-catalyzed reaction produces a product  $P$  and releases a free enzyme again for reaction (68). This reaction can be represented by,



where  $k_1$  is binding rate,  $k_{-1}$  unbinding rate, and  $k_2$  is the rate at which product  $P$  is formed from  $ES$  complex,  $k_{-2}$  the reverse production rate.

In cases where there is negligible reaction to produce  $P$  and only enzyme adsorption to form  $ES$  complexes, this equation simplifies to



When a piece of immobilized substrate with surface binding site concentration  $[S(t)]$  is immersed in enzyme solution at concentration  $[E]$ , the rate of change in the surface concentration of enzyme-substrate complex  $[ES(t)]$  is described by

$$\frac{d[ES(t)]}{dt} = k_1[E][S(t)] - k_{-1}[ES(t)] \quad (3.3)$$

with initial condition  $[ES(t=0)] = 0$ , where  $t$  is time.

Assuming a large reservoir of enzyme solution, the enzyme concentration  $[E]$  stays constant throughout the time frame of interest. The available substrate concentration is  $[S(t)] = [S^M] - [ES(t)]$ , where  $[S^M]$  is total concentration of binding sites on the substrate. We can write the above equation as

$$\frac{d[ES(t)]}{dt} = k_1[E]([S^M] - [ES(t)]) - k_{-1}[ES(t)] \quad (3.4)$$

$$= k_1[E][S^M] - (k_1[E] + k_{-1})[ES(t)] \quad (3.5)$$

or

$$\frac{d[ES(t)]}{dt} + (k_1[E] + k_{-1})[ES(t)] = k_1[E][S^M] \quad (3.6)$$

Multiplying both sides by  $e^{(k_1[E]+k_{-1})t}$ , we have

$$\frac{d[ES(t)]}{dt} \cdot e^{(k_1[E]+k_{-1})t} + (k_1[E] + k_{-1})[ES(t)] \cdot e^{(k_1[E]+k_{-1})t} = k_1[E][S^M] \cdot e^{(k_1[E]+k_{-1})t} \quad (3.7)$$

or

$$\frac{d}{dt}([ES(t)] \cdot e^{(k_1[E]+k_{-1})t}) = k_1[E][S^M] \cdot e^{(k_1[E]+k_{-1})t} \quad (3.8)$$

which we can integrate and solve for  $[ES(t)]$ :

$$[ES(t)] \cdot e^{(k_1[E]+k_{-1})t} = \frac{k_1[E][S^M]}{k_1[E] + k_{-1}} \cdot e^{(k_1[E]+k_{-1})t} + C \quad (3.9)$$

$$[ES(t)] = \frac{k_1[E][S^M]}{k_1[E] + k_{-1}} + C \cdot e^{-(k_1[E]+k_{-1})t} \quad (3.10)$$

where  $C$  is an arbitrary constant. Setting initial condition  $[ES(0)] = 0$ , we have

$$C = -\frac{k_1[E][S^M]}{k_1[E]+k_{-1}} \text{ or}$$

$$[ES(t)] = \frac{k_1[E][S^M]}{k_1[E] + k_{-1}}(1 - e^{-(k_1[E]+k_{-1})t}) \quad (3.11)$$

which agrees with a solution obtained by Johnson (34). As  $t \rightarrow \infty$ , i.e., in steady state,  $[ES] = \frac{k_1[E][S^M]}{k_1[E]+k_{-1}}$ . Defining the dissociation constant  $K_d = \frac{k_{-1}}{k_1}$ , the Langmuir binding isotherm,

$$[ES] = \frac{[E][S^M]}{[E] + K_d} \quad (3.12)$$

is obtained.

When the substrate concentration is much higher than the enzyme concentration and enzyme adsorption on the substrate is too quick to be continuously monitored, the binding kinetics is deduced using steady state Langmuir isotherms or similar models, where  $t$  can be safely assumed large (34). But Eq. 3.11 shows that the rate of  $[ES(t)]$  formation can be monitored if either the forward binding rate  $k_1$  is sufficiently small, or enzyme concentration  $[E]$  is low enough, or both.

In the current study, we used CLSM to monitor cellulase ( $E$ ) binding to pretreated wood substrates ( $S$ ), and recorded cellulase adsorption to the substrate and hence  $ES$  formation by observing the increase of fluorescent label on the substrate. First, pretreated wood particles were immobilized onto borosilicate coverslips, followed by the addition of fluorescently-labeled cellulase solution. Localized fluorescence increments on wood substrates indicated accumulation of fluorophores and hence cellulase binding. By continuously monitoring fluorescence intensity and fitting the intensity curves to Eq. 3.11, binding rates can be extracted.

### 3.3 Materials and Methods

**Pretreated Biomass** Mixed hardwood (harvested in central NY, fall 2007) was size reduced using a cutting mill (IKA Wilmington, NC) with a 1mm screen. The resulting biomass was sieved to obtain particles collected between 75 and 38 $\mu$ m mesh screens (U.S. Standard 200 and 400 sieve respectively, E. H Sargent and Co., Chicago, IL). Cutting and sieving was repeated three times to ensure that the collected fraction was representative of the original biomass. Deionized water was added to form a slurry containing 15%(w/w) biomass. The mixture was added to a high-pressure reactor and pretreated at 200 °C for 5 minutes (after 7.5 minutes of heat-up time) with a pressure of 450 psi of gaseous  $CO_2$  using a method described by Luterbacher *et al.* (53). The resulting slurry was filtered using Miracloth filtering cloth (Merck Darmstadt, Germany, 38 $\mu$ m openings) and washed with 1L of deionized water. After pretreatment, wood particles were air dried and stored at -20 °C until use, when they are re-suspended in water at a concentration of approximately 0.01%(w/w).

**Microscope coverslip preparation** Four-inch  $170\mu\text{m}$  borosilicate wafers were first patterned with gold fiducial marks and cut into  $16 \times 16\text{mm}^2$  square coverslips. Techniques of lithographically defining gold patterns on dielectric substrate have been described elsewhere (29), and is repeated here for clarity:  $2\mu\text{m}$  wide patterns were exposed on photoresist (Shipley 1805) and dry-etched approximately  $100\text{nm}$  into borosilicate substrate. A  $10\text{-nm}$  layer of titanium was evaporated as adhesion layer, followed by  $90\text{nm}$  gold film, and lifted off by dissolving photoresist in acetone. We were left with a flat substrate surface, with gold patterns in rows and columns denoted by numbers 0 through F (in hexadecimal). Subsequent cellulose particle identification at any position on the substrate can be easily located. After acetone and isopropyl alcohol rinses, and  $O_2$  plasma clean (Harrick Plasma, Ithaca, NY), a coverslip was glued to the bottom of a MatTek (Ashland, MA)  $35\text{mm}$  petri dish, covering the  $14\text{mm}$  pre-fabricated opening. The MatTek petri dish held the cellulase solution during binding experiments.

**Immobilization of Pretreated Wood Particles** A drop of  $10\mu\text{L}$  water suspension containing approximately  $0.01\%(w/w)$  pretreated particles was pipetted on the gold-patterned coverslip, covering approximately an area of  $60\text{mm}^2$ . The surface was allowed to dry overnight at ambient temperature, to let particles adhere. The adsorbed particles were rehydrated with  $50\text{mM}$  sodium acetate buffer ( $pH = 5.5$ ) and the borosilicate surface washed 3 times, with gentle agitation (Orbital shaker  $60\text{ rpm}$  for 5 minutes each). The particles were then incubated with  $0.5\%$  Bovine Serum Albumin (BSA) in  $2\text{mL}$  sodium acetate buffer for 30 minutes, before being washed again and incubated in sodium acetate buffer over night, ready for imaging. Normally at this point, over  $90\%$  of particles

would have been washed away. Yet the remaining dozen or so particles were sufficient for time-lapse enzyme-binding experiments.

**Scanning Electron Microscopy (SEM) Imaging of Immobilized Particles** To study surface morphology of individual particles, SEM was used to take high resolution images of immobilized particles. A clean borosilicate substrate, along with immobilized particles, was first coated with approximately 20 gold-palladium using Hummer V sputtering tool (Technics, San Jose, CA), at a pressure of  $39\text{mTorr}$ , sputtering current  $10\text{mA}$ , for approximately  $30\text{sec}$ . Metal film coating helps dissipate the charge that can build up when a dielectric sample, such as pretreated wood, is targeted under an electron beam. SEM images were taken with a Zeiss Ultra 55 (Carl Zeiss NTS GmbH, Oberkochen, Germany), at an accelerating voltage of  $1.38\text{kV}$ , aperture size of  $30\mu\text{m}$ , and a working distance  $2.6\text{mm}$ .

**Cellulase Enzyme Production, Labeling, and Purification** *T. fusca* Cel5A and Cel9A were expressed in *Streptomyces lividans* and the culture was grown as described in (35). *T. fusca* Cel6B was expressed in *Escherichia coli* and grown as described in (32). Fluorescent labeling of cellulases was done with Alexa Fluor 488 and 647 amine-reactive labels (Molecular Probes, CA), and purified as described in (62). For the current study, we used the batches of enzymes with measured degree of labeling, or the average number of dyes-per-protein, equal to 1. Labeled enzymes were kept at  $200\text{nM}$  concentration of  $50\mu\text{L}$  aliquot and stored at  $-20^\circ\text{C}$  until just before use, when they were diluted in ROX buffer (described below) to make enzyme solutions between 2 and  $10\text{nM}$ .

**Cellulase Solution in ROX Buffer** Enzyme binding experiments were carried out at room temperature, with enzyme concentrations varying from 2nM to 10nM, in 2mL of ROX buffer:  $pH = 5.5$ , 50mM Sodium-Acetate, 8U Glucose Oxidase, 120U Catalase, 2mM Trolox, 1mM Methyl-Viologen and 3% Glucose, all obtained from Sigma-Aldrich (St. Louis, MO). Compared to Sodium Acetate Buffer supplemented with ascorbic acid as a reducing agent, the ROX cocktail significantly increased fluorophore photostability, and improved photon output (26,99,100).

**CLSM Setup and Characterization** CLSM imaging was performed on an inverted microscope IX81, with a 100x oil-immersion objective. Three laser beams (488, 543 and 635nm) were combined and fiber-coupled into the microscope. Automated field scanning and image recording were performed using Fluoview software. The complete setup (see Fig. 3.1) was obtained from Olympus America (Center Valley, PA).

**Data Processing** Custom MATLAB (The Mathworks, Natick, MA) routines were used to perform numerical spectra separation, curve fitting of fluorescence intensity data to binding model. Specifically, time-lapse images saved by Fluoview software were first combined into one intensity map, showing highest fluorophore concentration areas, which we defined as regions of interest (ROI). Five discrete ROIs were cropped out of each intensity map, and used as masks to generate time-series intensity averages of each respective ROI. Intensity data from three channels were run through linear transformation routine to generate actual fluorescence profile of AF488, AF647, and wood autofluorescence, respectively. And finally, time-trace of AF488 or AF647 were fitted to enzyme

binding-kinetics model to obtain binding coefficients. Out of each set of experiment using a labeled enzyme at certain concentration, between 20 and 30 ROIs were analyzed to obtain binding coefficients, from which an average and standard deviation were calculated.

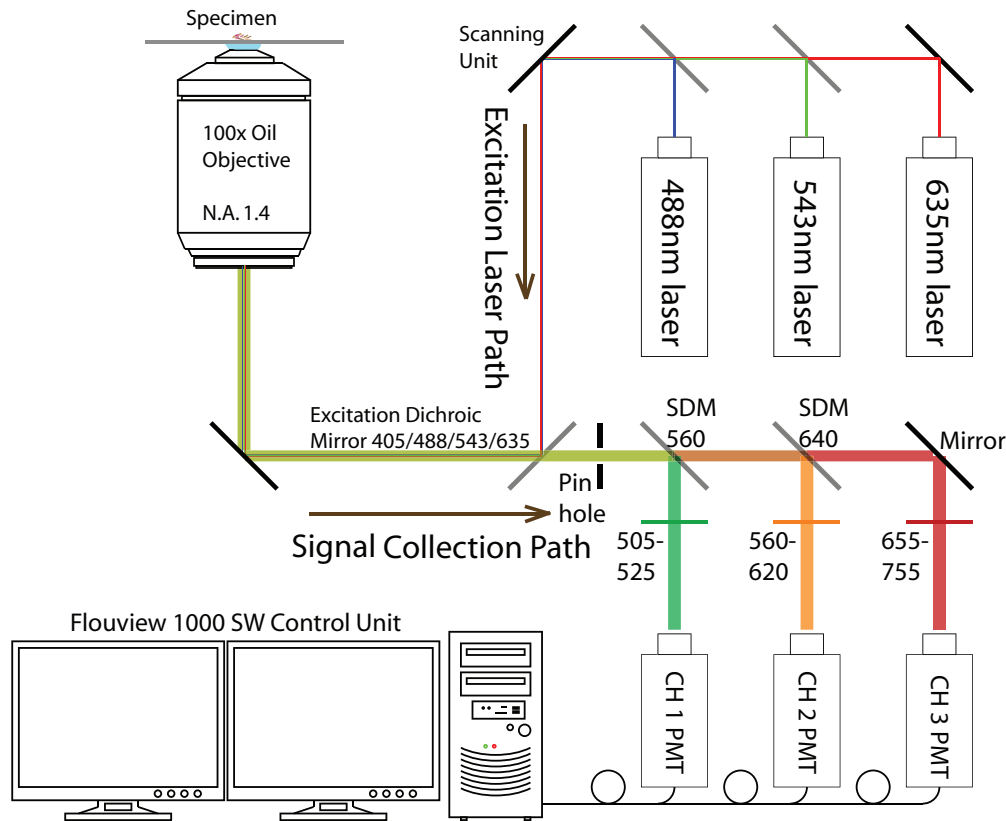


Figure 3.1: Confocal Laser Scanning Microscope set up using Olympus Flouview® 1000 system. Excitation lasers at 488nm, 543nm and 635nm are combined and scanned to illuminate the specimen through a SAPO 100x Oil objective with Numerical Aperture (N.A.) of 1.4. Fluorescence signal is collected with the same objective, and passed through a sequence of single band dichroic mirrors (SDM), filtered with band-pass optical filters before being collected by photo-multiplier tubes (PMT) of each channel.

### 3.4 Results and Discussion

**Morphology of Immobilized Wood Particles** Pretreated wood particles that adsorbed to borosilicate surfaces showed very diverse morphologies. A macroscopic view (Fig. 3.2a) shows that the mechanical milling and sieving process produces particle sizes on the length scale of 10 to 100 $\mu\text{m}$ , each comparable to a normal field of view of a confocal microscope. The width and thickness of these particles vary from a few to tens of micrometers. The edges of these particles are very rough as seen under the SEM, as are some parts of the surfaces. Folds and crevices present a large accessible surface area that is exposed to the surrounding environment. There are numerous fibrous protrusions from these crevices and edges, presenting the most accessible cellulose (Fig. 3.2b). When there is cellulase in solution, these areas will be the first sites that enzyme bind to. In addition, there are numerous sub-micrometer-scale pores on the particle surfaces (Fig. 3.2c,d). These pores are in fact the gaps between intertwined fibers that form the surface. Since the fiber layer is dense, these available gaps tend to be small, non-uniform, and do not necessarily form continuous passageways for molecule diffusion. It is likely then, that after cellulase enzymes adsorb to the most accessible surfaces of pretreated particles, diffusion of enzyme to the interior of the particles is made possible through these porous structures, and at the same time, hindered by the small pore size, and density of the surrounding material.

**Autofluorescence of Pretreated Particles** The exact origin of autofluorescence is not clear. It has been shown however, that residual aromatic compounds such as lignin and lignin derivatives in processed wood pulps can fluoresce when

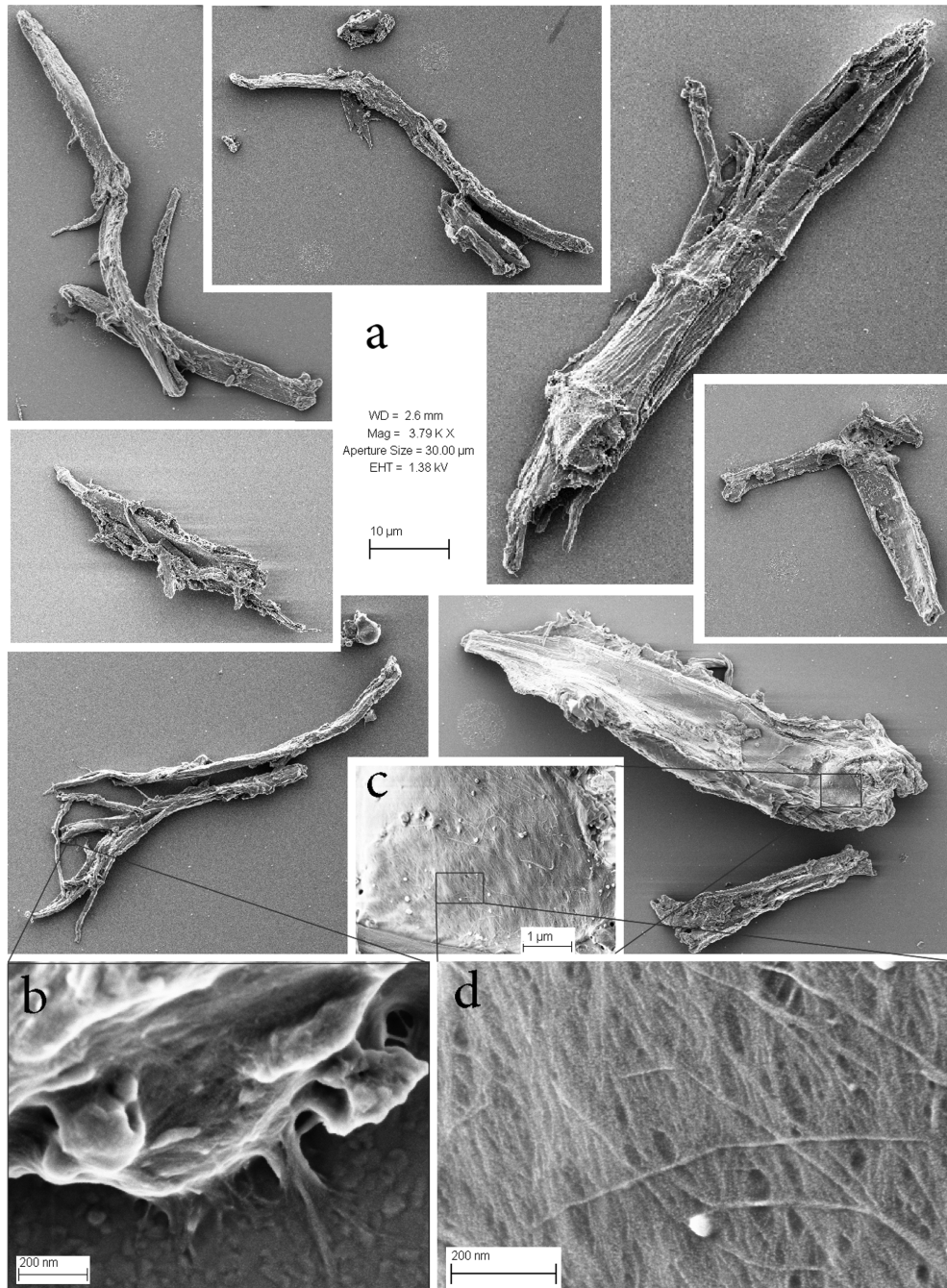


Figure 3.2: Scanning Electron Microscope (SEM) images of pre-treated wood particles immobilized on flat surface, showing a. Particles of various sizes and morphologies; b. Fibrous protrusions adhering to the surface, immobilizing the particle; c. Zoom-in view of one particle, showing such surface features as pores and criss-crossing fibers and d. where nano-meter scale pores are clearly visible.

excited with ultra-violet light (22, 52). To our advantage, however, these compounds are present inside various structures of the pretreated wood and they serve as a single fluorochrome (50, 52). Therefore, the detected autofluorescence spectrum stays constant for a given measurement condition and unaffected by the total intensity as long as the photo detector is not saturated. Unfortunately, this fluorescence emission is dominant in the 500nm band, and also has significant overlap with those of the AF488 and AF647 fluorophores.

Using spectral deconvolution method and results introduced in Chapter 2, we completely separate autofluorescence from that of cellulase fluorophore label, seen in Fig. 3.3, and minimized error in quantitative estimation of enzyme binding.

**Effect of ROX Buffer** To determine the rate of loss of fluorescence at nominal illumination laser power (2%), a piece of pretreated wood particle was allowed to incubate in ROX buffer with 2.5nM Cel6B labeled with AF488, and 2.5nM Cel6B labeled with AF647, for six hours at room temperature. A small area of a particle was then continuously imaged and the collected fluorescence monitored. The saved images were fed through spectra separation routine, and intensities of autofluorescence, AF488, and AF647 were extracted respectively. We fit the intensity time trace to an exponential decay function

$$Intensity(n) = Intensity(0) * e^{-d \times n} \quad (3.13)$$

where  $n$  is the number of scans,  $Intensity(n)$  is the average pixel intensity for scan  $n$ ,  $d$  is the constant that describes the rate of intensity decrease per scan. The rate of decrease is shown in Table 3.4.

The oxygen scavenging cocktail has different effects on the autofluorescence

of wood, and on the fluorescence of AF488 and AF647. Due to their small per-scan attenuation values, we can ignore the fluorescence loss of pretreated wood or AF488 for all practical purposes. On the other hand, for AF647, we see slightly higher rate of fluorescence decrease, at less than 1% per laser scan. Depending on the number of images taken, this attenuation factor may need to be taken into account. However for this study, the uncertainty due to diverse morphologies in the pretreated wood particle overwhelmed the slight decrease in AF647 fluorescence. Therefore we ignored this decrease as well. For comparison, similar bleaching experiments were carried out with 5mM ascorbic acid in sodium acetate buffer, in place of ROX buffer. Comparable bleaching characteristics were observed for AF488 and wood autofluorescence. However, the bleaching rate for AF647 fluorophores was approximately twice as fast as that in ROX buffer. Additionally, it is yet to be characterized as to the effects of ROX buffer on cellulase binding. In comparing fluorescence increase data taken using enzyme in ROX buffer to that in buffer with ascorbic acid, no appreciable difference was observed (data not shown).

**Temporal and Spatial Behavior of Cellulase Binding** At the start of each experiment, we took a series of CLSM image of several particles of interest incubated in ROX buffer, without added cellulase. At time 0, we pipetted out pure ROX buffer and replaced it with a 2mL enzyme solution at concentrations

Table 3.1: Fluorescence decay constant  $d$  of Equation 3.13 when substrate-bound and fluorescently labeled cellulases were continuously scanned by excitation laser source.

|                          | Wood                            | AF488                           | AF647                           |
|--------------------------|---------------------------------|---------------------------------|---------------------------------|
| $d$ (scan) <sup>-1</sup> | $(2.51 \pm 0.04) \cdot 10^{-3}$ | $(1.89 \pm 0.02) \cdot 10^{-3}$ | $(8.11 \pm 0.02) \cdot 10^{-3}$ |

between 2 and 10nM, in ROX buffer, and started time lapse imaging of the pre-treated wood particles. Images were typically recorded at intervals as short as 5 minutes, and the intervals were widened to approximately 30 minutes as the increase in fluorescent signal slowed, to reduce bleaching.

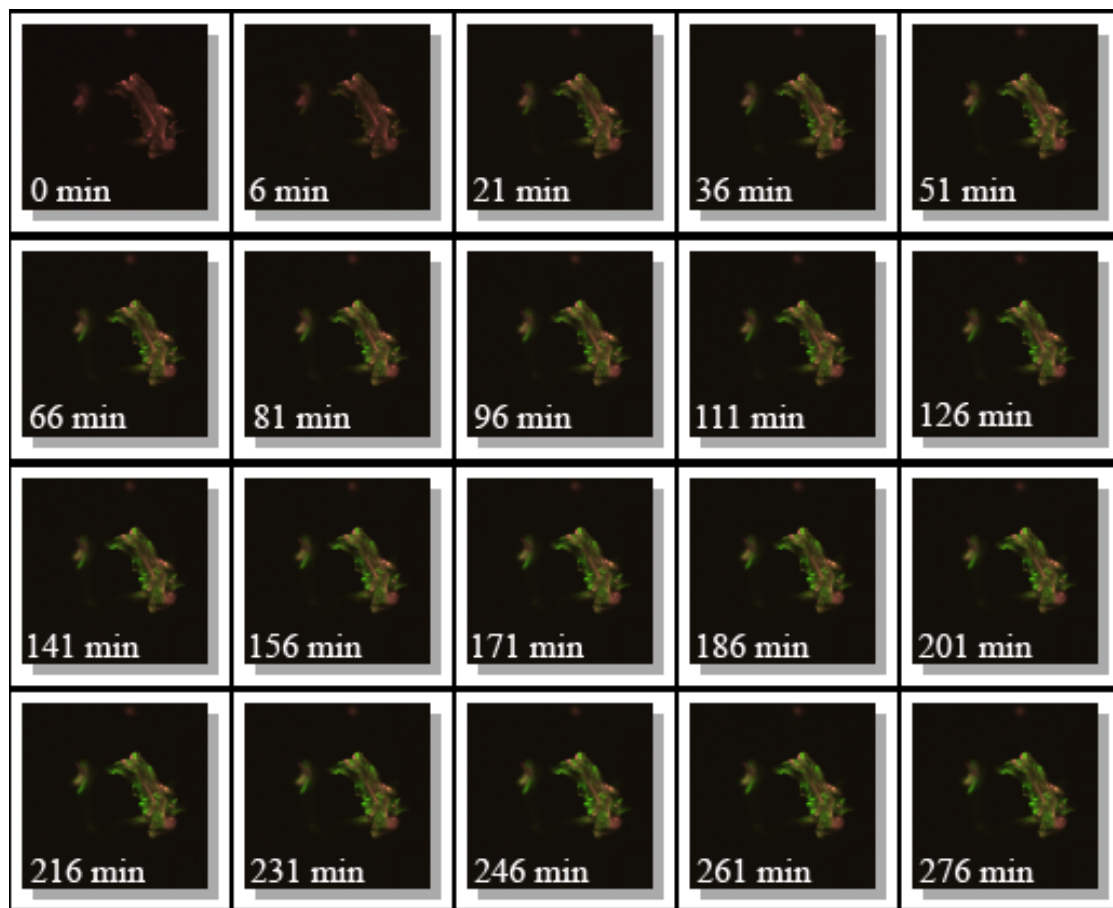


Figure 3.3: Sample enzyme binding images of *T. fusca* Cel9A labeled with AF488 at discrete time points. AF488-labeled Cel9A in ROX buffer was added to pretreated particles at time 0. Fluorescence in red channel was from wood particle's autofluorescence.

With labeled *T. fusca* cellulase, we observed increase in fluorescence on immobilized wood particles over a period of several hours. Qualitatively, the increase of fluorescence was the fastest shortly after cellulase was added (see Fig.

3.4).

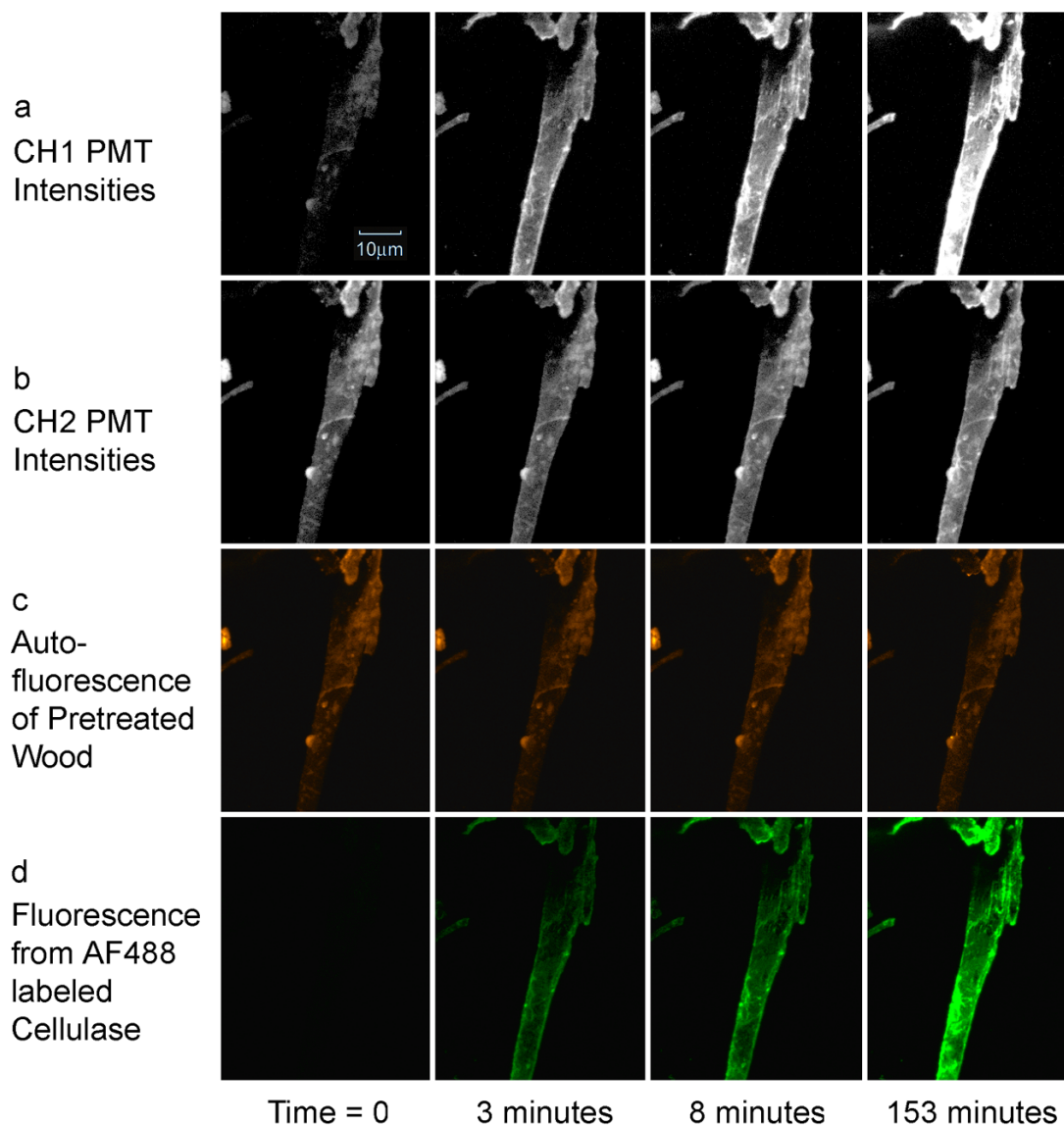


Figure 3.4: Sample enzyme binding images of *T. fusca* Cel5A labeled with AF488 at four discrete time points. AF488-labeled Cel5A in ROX buffer was added to pretreated particles at time 0, before which point, only autofluorescence was visible. As time progressed, more and more cellulases adsorbed to immobilized particles, represented by accumulation of AF488 fluorescence. Spectra deconvolution routines were used to separate AF488 fluorescence from autofluorescence of wood.

It was observed that the enzymes tended to accumulate quickest on the edges and thin surfaces of particles, indicating the most accessible binding sites. At the same time, where wood autofluorescence was the strongest, perhaps a relatively denser area inside the particle where lignin was abundant, little enzyme accumulation was seen within the experimental time frame. Although aromatic residue of lignin presented hydrophobic sites to which cellulase might non-specifically adsorb, these regions of the particle may have been blocked by BSA, or less porous and hence less accessible to enzymes.

**Estimating Binding coefficients** Several models have been used before in describing cellulase adsorption to cellulose, most notably the Langmuir model, for its simplicity and resulting in reasonably good fit for data in many cases (2, 25, 40, 41, 44, 46, 69, 74). Langmuir two-site and Langmuir-Freundlich isotherms have also been used to model enzyme adsorption to a heterogeneous surface (90, 94, 108), giving a generally better fit in cases of cellulase adsorption to cellulose, due to the complex fibrous structure of cellulose and the need for cellulases to diffuse into the porous structures of the fibers (60). Most of the previous reported measurements were performed, however, when adsorption had reached steady state, and the isotherm models related concentration of enzyme-substrate complex to free enzyme concentration. The kinetics of enzyme adsorption to cellulose surface was only inferred from the binding constants since time was assumed to be long i.e, when reaction had reached equilibrium.

On the other hand, the ability to measure temporal changes in the formation of enzyme-substrate complex can also be used obtain the binding rates. Given the complexity of the substrate in our case, several important assumptions are made in deriving the binding kinetics model. First, only the most

accessible surface areas of the substrate are considered. As was shown in the theory section, this is equivalent to using the classical Langmuir equation and ignoring the interstitial penetration and saturation (36). Second, the enzyme concentration in solution is assumed constant throughout the duration of the binding experiments. This assumption, though ideal, is acceptable because a relatively large volume ( $2mL$ ) of enzyme solution is used, compared to the total volume of micro-scale particles that are on average less than  $1nL$  in size, and less than 20 particles, for each experiment. The initial binding period in particular, on the order of tens of minutes, is short enough to assume constant enzyme-concentration, and also long enough for cellulase in buffer to replenish adsorbed enzyme surrounding the particle surfaces, where free enzyme diffusion in solution is on the order of  $10^{-6}cm^2/s$  (33). It is also assumed that the bleaching rate of bound AF-labeled enzyme is negligible. This is made possible by the ROX buffer described in Materials and Methods. In addition, it has been reported that the hydrolysis rate at room temperature is negligible compared to adsorption (55). Hence, we assume no enzyme-substrate complex loss due to hydrolysis in the time frame of our experiments.

**Data Fitting** For each time-series image of one pretreated particle, five distinct regions of interest (ROI) were cropped out. Since we were mostly interested in the most accessible sites of these particles, we focused on those ROIs with the most enzyme accumulation, shown as having the most fluorescence. Average pixel intensity of each ROI was calculated and normalized with respect to the average pixel intensity of wood autofluorescence of each ROI. This was done to compensate for different morphologies of the ROI and varying amounts of substrate presented in the ROI, with the assumption that for each experiment,

autofluorescence is a relatively consistent measure of the quantity of wood and hence the number of binding sites. This yielded a time course of average pixel fluorescence of a sample ROI as shown in Fig. 3.5, and then fitted to Eq. 3.11.

From each fit, a time coefficient  $k_1[E] + k_{-1}$  was obtained and along with it associated 95% confidence interval that described the rate of fluorescence increase. Combining results from all ROIs of a given experiment, we could calculate  $k_1[E] + k_{-1}$  and its uncertainties, and derive binding rate  $k_1$  and unbinding rate  $k_{-1}$  with known enzyme concentration  $[E]$ . For simplicity, one further assumption was made that the unbinding rate  $k_{-1}$  could be ignored at the initial binding stage, as it has been reported that cellulase enzymes bind tightly to the cellulose substrate (5).

Although binding rate  $k_1$  was expected to be fairly constant for each enzyme-substrate pair, large variations in the fitted parameters were observed, as evident in Table 3.2. However, the binding rates  $k_1$  for all three enzymes appear smaller at low concentrations. We attribute this inconsistency in  $k_1$  to enzyme loss due to non-specific adsorption to the petri dish side walls, despite initial BSA blocking step prior to each experiment. Indeed, extracted  $k_1$  values for experiments done at higher enzyme concentration solutions are larger, since a smaller fraction of enzyme was lost to non-specific adsorption. Furthermore, the binding rates at the highest concentrations we measured, are similar to results obtained in previous studies with BMCC, whose bindings sites are easily accessible (63). Nevertheless, given the large variations seen in these data, only order-of-magnitude estimation can be made on the binding rates of Cel5A, Cel6B and Cel9A, to pretreated wood. It is on the order of  $10\mu M^{-1} \cdot min^{-1}$ .

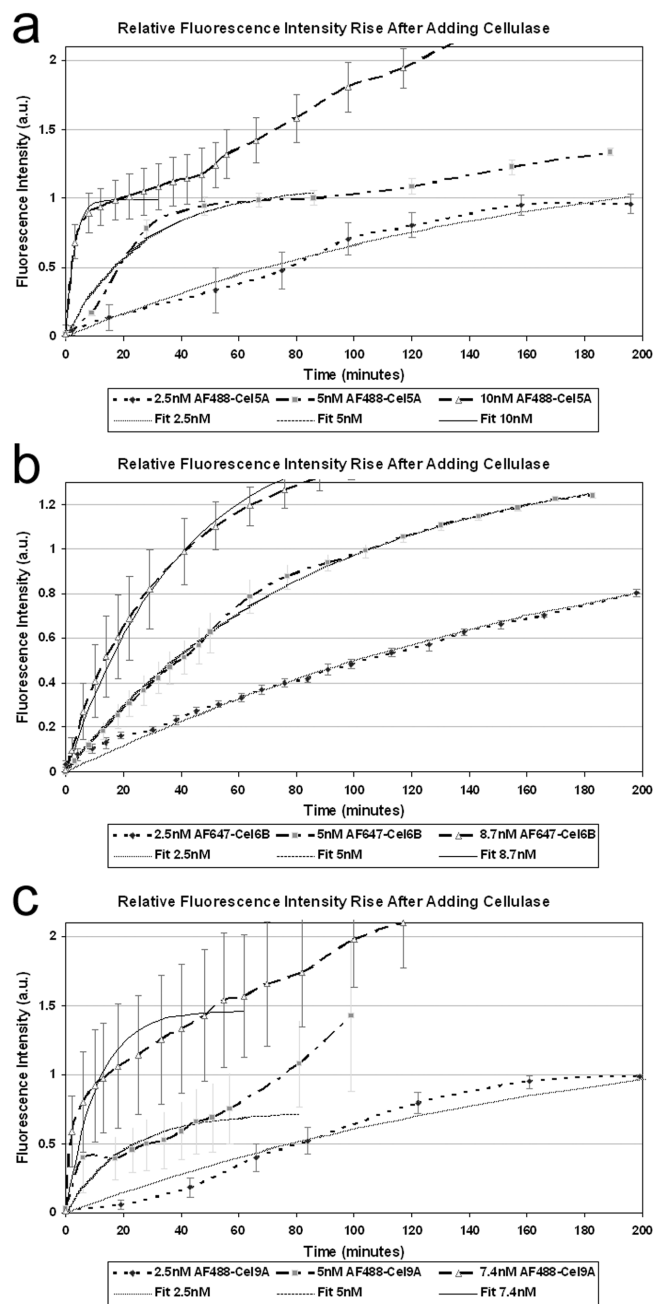


Figure 3.5: Sample data-fitting curve with 2.5nM, 5nM and 10nM Cel5A-AF488 fluorescence increment data. Each data series as fit to Eq. 3.11. In this case, data points after the initial jump of fluorescence are arbitrarily excluded in order to limit the binding kinetics to the most accessible sites and exclude kinetics involving interstitial diffusion and adsorption.

**Preferential Binding to Accessible Sites** Throughout binding experiments the greatest fluorescence accumulation was observed at edges and intra-particle gaps that were created in the mechanical milling process. Such process leaves large surface area exposed to the surrounding environment. With cellulases present, these surfaces and their fibrous protrusions present the most accessible enzyme binding sites. The initial binding of enzyme to these sites can be modeled by the Langmuir isotherm, confirmed by CLSM data. As cellulases adsorb

Table 3.2: Fitting result of  $k_1$  for AF488/647-labeled Cel5A, Cel6B and Cel9A. Smaller  $k_1$  values at low enzyme concentrations are most likely due to enzyme loss to the petri dish side walls, and hence the actual enzyme concentration was much lower than we had prepared. For this reason, we conclude the binding rates obtained at higher enzyme concentrations are closer to the actual values.

|                    |   |
|--------------------|---|
| [Cel5A-AF488] (nM) | $k_1(\mu M^{-1} \cdot \text{min}^{-1})$ |
| 2.5                | 7.48±4.36                               |
| 5                  | 8.64±2.64                               |
| 10                 | 26.64±14.37                             |
| [Cel6B-AF647] (nM) | $k_1(\mu M^{-1} \cdot \text{min}^{-1})$ |
| 2.5                | 3.89±2.97                               |
| 5                  | 3.81±2.48                               |
| 8.7                | 6.56±2.47                               |
| [Cel9A-AF488] (nM) | $k_1(\mu M^{-1} \cdot \text{min}^{-1})$ |
| 2.5                | 5.05±4.80                               |
| 5                  | 8.58±6.43                               |
| 7.4                | 37.16±25.95                             |

onto the most accessible sites, however, additional enzymes diffuse into the pretreated particle via pores and crevices, and adsorb onto the less accessible but nonetheless available sites. Thus we saw the continuous rise of fluorescence after the initial jump but equilibrium was never reached.

**Limitations of the current model** Due to the necessity of truncating a portion of the data to make the fit, the Langmuir saturation model, or our simple transient limited-binding model does not completely describe what takes place in pretreated wood particles. A more comprehensive model, that describes the interstitial diffusion and binding in addition to surface binding, is needed to provide a better fit of our fluorescence data. In fact as mentioned earlier, a two-site Langmuir and Langmuir-Freundlich isotherms have been proposed to describe the complex interactions between cellulose and cellulase. However, a transient model that takes time into account as an independent variable, in addition to enzyme concentration remains to be developed.

### 3.5 Conclusions of Binding Study using CLSM

CLSM images reveal *T. fusca* cellulases preferentially bind to the most accessible sites of pretreated wood particles. The binding rates of AF488/647-labeled Cel5A, Cel6B and Cel9A, from kinetic curves that are derived from time-lapse imaging, are on the order of  $10\mu M^{-1}min^{-1}$ , agreeing in principle with previously published values. In reaching this result, we have made several assumptions and approximations. We also limited our model to enzyme binding to the most accessible sites. But as we have found in time-lapse imaging, cellulase

enzyme not only bind to the most accessible surface sites, but also diffuse into and adsorb to the inside of the pretreated particles, via numerous nano-scale pores. Therefore, a more comprehensive transient enzyme-binding model to complex cellulose structures, such as wood, is needed. In addition, we have developed a method to spectrally deconvolve Alexa Fluorophore signal from auto-fluorescence of wood. This is important when quantitative fluorescence microscopy techniques are used to study real substrates.

## **3.6 Advanced Discussions on Diffusion and Binding**

### **3.6.1 Diffusion of fluorescent probes into cellulose particles**

**Labeled Particles** Several fluorescent probes were considered in studying porosity of cellulose particles. Our initial choice was FITC-labeled Polyethylene glycol (PEG). However we have found PEG to be non-specifically adsorbed to the surface of the wood particles, thus making it impossible to study the porosity of the pretreated particles. On the other hand, FITC- or TRITC-labeled dextrans of varying molecular weights have been used to characterize the permeability of either synthetic or natural membranes (73, 83), indicating their feasibility in studying diffusivity of porous material.

We obtained and characterized fluorescently-labeled dextran particles with molecular weight ranging from 4kDa to 2000kDa (TdB Consultancy AB, Sweden), and measured their sizes using Zetasizer (Malvern Instruments, Worcestershire, UK).

The sizes of cellulase enzymes are on the order of  $10\text{nm}$ 's. Therefore our diffusion experiments using fluorescent probes should focus on those particles on the order of  $10\text{kDa}$ .

We use FITC-labeled Dextran particles with molecular weight  $20\text{kDa}$ ,  $40\text{kDa}$  and  $70\text{kDa}$  as diffusive probes to investigate porosity of cellulose particles. These sizes of particles were selected because they have hydrodynamic radii between 4 and 6 nanometers, close to those of *T. Fusca* cellulases. In our previous experimental results (not shown), we noticed that  $155\text{kDa}$  Dextran-TRITC particles could diffuse into cellulose particles very slowly, and become trapped inside the particles. However, the time frame for  $155\text{kDa}$  Dextran-TRITC diffusion is on the order of days, far slower than we had observed in cellulase diffusion. On the other hand, previous elution measurements showed  $40\text{kDa}$

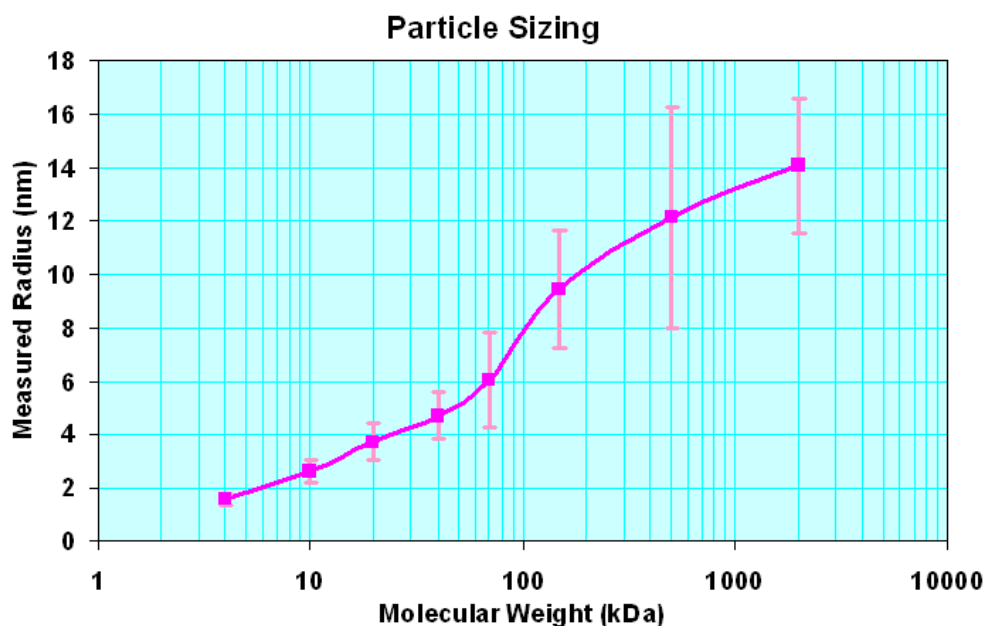


Figure 3.6: Size distribution of FITC- or TRITC-labeled dextran particles.

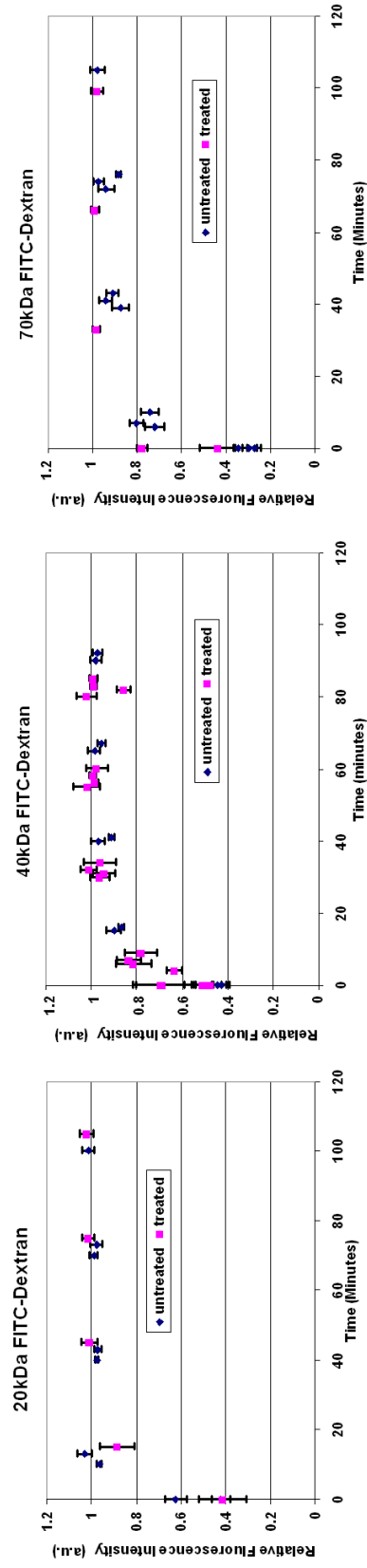


Figure 3.7: Fluorescently labeled dextran particles diffusing into pre-treated and un-treated wood particles.

FITC-labeled Dextran particles were easily washed out of the cellulose particles when they have been incubated with the particles for several days, indicating their fast diffusion constant within the cellulose particles.

We incubated 20kDa, 40kDa and 70kDa FITC-labeled Dextran with pretreated wood particles for several hours, and analyzed the fluorescence intensity within the cellulose particles over time. When fluorescent probes are first added to the cellulose particles, the fluorescence in the cellulose-occupied region consists of the particles' autofluorescence alone. The fluorescence due to probes is assumed to be nil, due to exclusion effect of the particles. However, over time the fluorescent probes will diffuse into the cellulose particles via pores and crevices, making the fluorescence within particle's volume increase. By analyzing the increase of the fluorescence, we can estimate the diffusion behavior of the labeled probes.

Fig. 3.7 shows fluorescence intensity increase inside the volume occupied by cellulose particles. Each data point is an average pixel intensity of five regions of interests of a given measurement sequence, with error bar showing standard deviation. Two kinds of particles were used in this experiment. The blue diamonds denote untreated wood particles, whereas purple squares denote treated particles.

We see the diffusion of the small labeled probes into the particles is rapid. In fact the particles are occupied with these probes within an order of tens of minutes. This is true for probes of all three molecular weights used. And there does not seem to be discernible difference in diffusion behavior among the three. We attribute this to the various pore sizes present on the wood particles, which allow both large and small probes to pass through. Due to the diverse morphol-

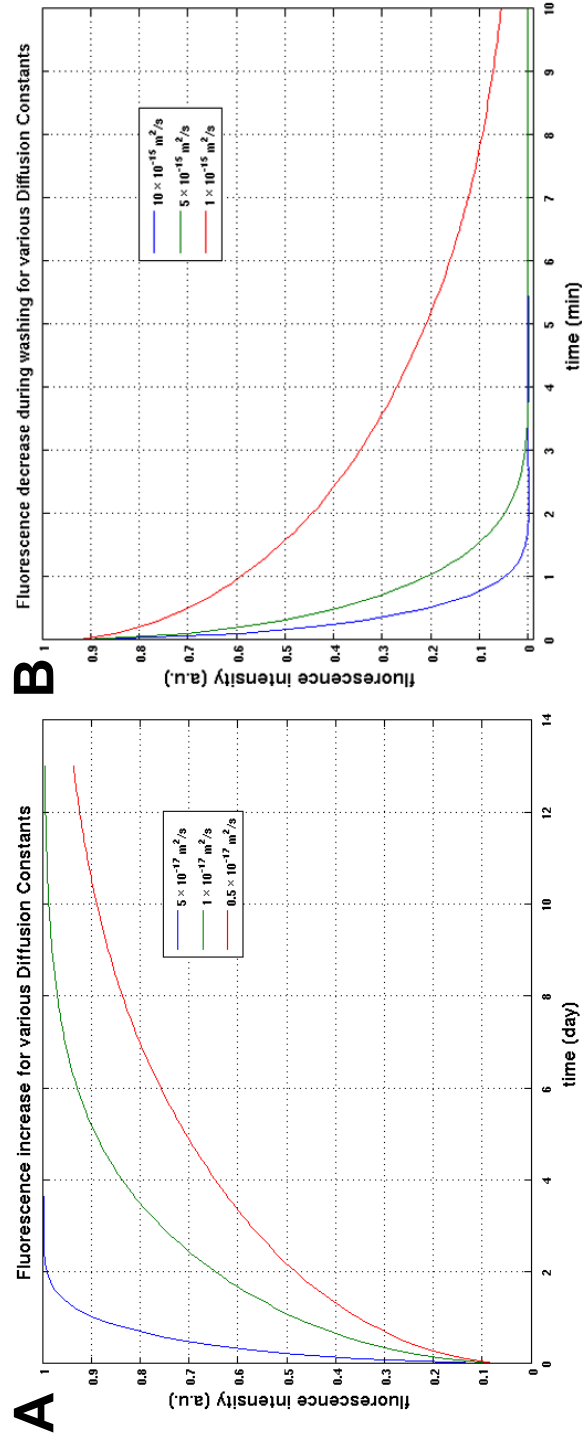


Figure 3.8: Simulation of A. Incubation and B. Washing of labeled probes inside porous medium with arbitrary diffusion constants. In general we see the curves follow an exponential decay model.

ogy of the particles, an exact diffusion constant cannot be calculated. But we do get an order of magnitude estimation of the diffusion behavior, that agrees with what we had obtained before using numerical simulation. In fact, by comparing the measurement results above and our simulation results shown in Fig. 3.8, the diffusion constant of the labeled probes within cellulose is between  $10^{-16}$  and  $10^{-15}m^2/s$ .

### 3.6.2 Interstitial Diffusion and Binding Model

**Transient Enzyme-Binding Model** When enzyme has to diffuse through porous media in order to bind to substrates, we have a situation of combined diffusion and binding. The situation becomes more complex when the same porous medium is also the substrate to which the enzyme would bind.

In literature research we came upon work done by F. J. W. Roughton in the modeling and analysis of diffusion and chemical reaction of oxygen and carbon monoxide in thin layers of Haemoglobin (80). The underlying physics of O<sub>2</sub> or CO diffusing and binding to haemoglobin is similar to that of cellulases diffusing into and binding onto cellulose fibrils with finite porosity and volume. Specifically, both reactions involve an infinite volume of solution of reactive solute, held at constant concentration, surrounding a thin slab of substrate, to which the solute can diffuse in and adsorb.

**The Diffusion Equation** In the simplest 1-dimensional diffusion case, Fick's first law of diffusion states that the rate of diffusion of substance  $Q$  across any plane of area  $A$  at right angles to the direction of diffusion  $x$  is proportional to

the gradient of concentration  $u_f$  across that plane. In equation form, it is written as

$$\frac{dQ}{dt} \div A = D \times \frac{\partial u}{\partial x} \quad (3.14)$$

where  $t$  is time, and  $D$  an arbitrary constant defined by the *Stokes-Einstein Equation*

$$D = \frac{RT}{N} \frac{1}{6\pi\eta r} \quad (3.15)$$

Now consider an isotropic medium with unit volume defined by  $dx dy dz$ . From Fick's first law, we see the unit-time in-flow to the volume from the left is

$$-D \left( \frac{\partial u}{\partial x} - \frac{\partial}{\partial x} \frac{\partial u}{\partial x} \frac{dx}{2} \right) dy dz \quad (3.16)$$

Similarly, the unit-time out-flow from the volume to the right side is

$$-D \left( \frac{\partial u}{\partial x} + \frac{\partial}{\partial x} \frac{\partial u}{\partial x} \frac{dx}{2} \right) dy dz \quad (3.17)$$

Therefore the net rate of change of  $Q$  into volume  $dx dy dz$  is

$$\frac{dQ}{dt} = D \frac{\partial^2 u}{\partial x^2} dx dy dz \quad (3.18)$$

Since  $Q = u dx dy dz$ , we have

$$\frac{du}{dt} = D \frac{\partial^2 u}{\partial x^2} \quad (3.19)$$

This relation can be easily expanded to 3-dimensional diffusion, resulting in Fick's second law of diffusion:

$$\frac{du}{dt} = D \left( \frac{\partial^2 u}{\partial x^2} + \frac{\partial^2 u}{\partial y^2} + \frac{\partial^2 u}{\partial z^2} \right) = D \nabla^2 u \quad (3.20)$$

**The Binding Equation** When an enzyme  $E$  is added to its substrate  $S$ , the two form an enzyme-substrate complex  $ES$  before the enzyme-catalyzed reaction produces a product  $P$  and releases a free enzyme again for reaction (68). This reaction can be represented by, In cases where there is negligible reaction to produce  $P$  and only enzyme adsorption to form  $ES$  complexes, this equation simplifies to



where  $k_1$  is binding rate,  $k_{-1}$  unbinding rate.

Consider enzyme adsorption inside the volume  $dx dy dz$ , enzyme  $E$  in solution is at concentration  $u_f$ , where  $f$  denotes free enzyme. We denote the concentration of  $ES$  by  $u_b$  where  $b$  means bound enzyme. Substrate  $S$  has total available sites  $S^M$  per unit volume.

Since  $[S(t)] = S^M - u_b(t)$ , we have

$$\frac{du_b(t)}{dt} = k_1 u_f(t)(S^M - u_b(t)) - k_{-1} u_b(t) \quad (3.22)$$

**Diffusive Binding** But we see  $u_f(t)$  and  $u_b(t)$  are now entangled. While the material input into the infinitesimal volume  $dx dy dz$  driven by Fick's first law is still  $D\nabla^2 u_f$ ,  $u_f$  is also consumed by adsorption, i.e,

$$\frac{du_b}{dt} = k_1 u_f (S^M - u_b) - k_{-1} u_b \quad (3.23)$$

generating the bound species  $u_b$ , where we have omitted the time-dependence of  $u_f$  and  $u_b$  for simplicity.

Therefore the complete equation describing the freely-diffusing species in

the infinitesimal volume  $dxdydz$  is

$$D\nabla^2 u_f = \frac{\partial u_f}{\partial t} + k_1 u_f (S^M - u_b) - k_{-1} u_b \quad (3.24)$$

$$= \frac{\partial u_f}{\partial t} + k_1 S^M u_f - (k_1 u_f + k_{-1}) u_b \quad (3.25)$$

**Diffusion and Adsorption in a Thin Slab of Substrate** Analytical solution to the above equation for arbitrary geometry is generally not available. For special geometries such as a thin slab of substrate, we can attempt an approximate solution.

Consider a piece of material with thickness  $2b$ , extending in the  $x$  direction from  $-b$  to  $+b$ , and its two other dimensions much larger than its thickness, rendering any diffusive material transport effectively one-dimensional. At time  $t = 0$ , this material is immersed in a large volume of enzyme solution with concentration  $u_0$ . The problem can be written as:

$$\begin{cases} D \frac{\partial^2 u_f}{\partial x^2} = \frac{\partial u_f}{\partial t} + k_1 S^M u_f - (k_1 u_f + k_{-1}) u_b, \\ \frac{du_b}{dt} = k_1 S^M u_f - (k_1 u_f + k_{-1}) u_b \end{cases} \quad (3.26)$$

with boundary and initial conditions:

1. At  $t = 0$ ,  $u_f = u_b = 0$  for all values of  $x$  within the slab.
2. At  $x = \pm b$ ,  $u_f(t) = u_0$  for all  $t$ .
3. At  $x = 0$ ,  $\frac{\partial u_f}{\partial x} = 0$  at all times.

These equations do not in general yield closed-form solutions. But for the short time after  $t = 0$ , when  $u_b$  is negligibly small, we can approximate the differential

equations as

$$\begin{cases} D \frac{\partial^2 u_f}{\partial x^2} = \frac{\partial u_f}{\partial t} + \kappa u_f, \\ \frac{du_b}{dt} = \kappa u_f \end{cases} \quad (3.27)$$

where we have introduced an effective binding constant  $\kappa = k_1 S^M$ .

The analytical solution to the partial differential equation above is then (80),

$$u_f = u_0 \left[ \frac{\cosh(x \sqrt{\frac{\kappa}{D}})}{\cosh(b \sqrt{\frac{\kappa}{D}})} - \frac{2}{b} \sum_{n=0}^{\infty} \frac{(-1)^n \beta_n}{\beta_n^2 + \frac{\kappa}{D}} \cos(\beta_n x) e^{-\beta_n^2 D t - \kappa t} \right] \quad (3.28)$$

where  $\beta_n \triangleq \frac{2n+1}{2b} \pi$ . And  $u_b = \kappa u_f t$ .

Before going further and plugging numbers into this equation, let's see what each term really means and find approximate range of each term. The effective diffusion constant is estimated to be between  $10^{-15} m^2/s$  and  $10^{-18} m^2/s$ , translated into between  $60 \cdot 10^{-3} \mu m^2/min$  and  $60 \cdot 10^{-6} \mu m^2/min$ . On the other hand, the binding rate  $k_1$  has been estimated to be between 1 and  $100 \mu M^{-1} \cdot min^{-1}$  (111), and the maximum available binding sites  $S^M$  is estimated to be between 1 and  $10 \mu M$ . This gives effectively  $\kappa$  a range of 1 and  $1000 min^{-1}$ . Therefore  $\kappa/D$  is between 4 and  $10^4 \mu m^{-2}$ , or  $\sqrt{\kappa/D}$  is between 2 and  $100 \mu m^{-1}$ . Since we are interested in  $x$  and  $b$  in the  $\mu m$  range,  $e^{x \sqrt{\kappa/D}} \gg 1 \gg e^{-x \sqrt{\kappa/D}}$ . Therefore,

$$\frac{\cosh(x \sqrt{\frac{\kappa}{D}})}{\cosh(b \sqrt{\frac{\kappa}{D}})} \approx e^{(x-b) \sqrt{\frac{\kappa}{D}}} \quad (3.29)$$

The important parameters to extract from the solution are: effective diffusion constant  $D$  which describes the porosity of the material and effectiveness of pretreatment, and  $\kappa = k_1 S^M$  which describes maximum available binding sites and binding rate. Integrating  $u_b$  and  $u_f$  throughout the volume of  $-b < x < b$ , we should have the model that approximates measured fluorescent data reflecting the total amount of labeled enzymes within the cellulose particle. Fitting this model to experimental data could present challenges, however, because

each model is an infinite sum of terms. Therefore, further simplification will be needed in order to utilize numerical fitting methods.

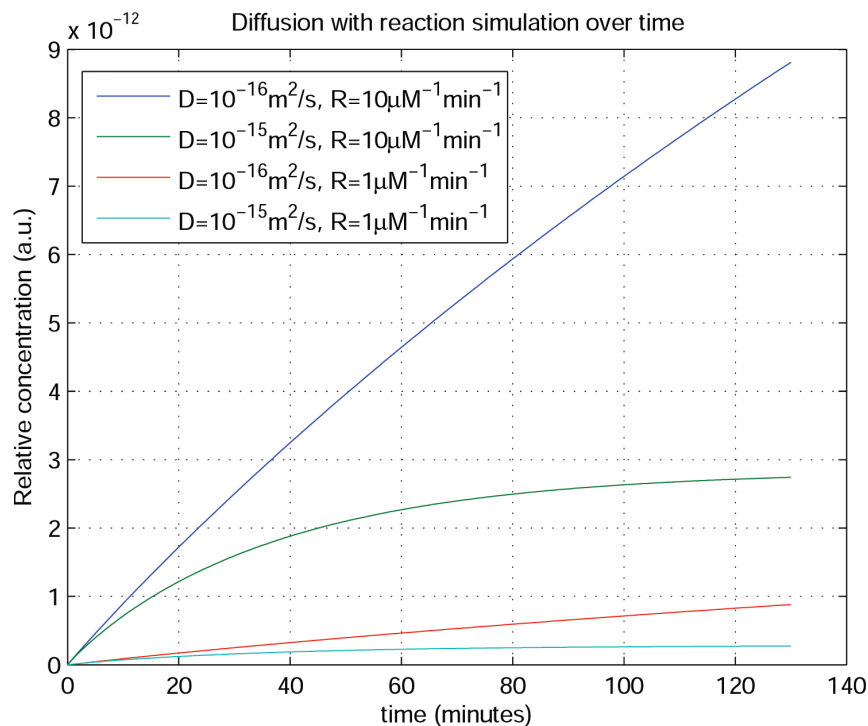


Figure 3.9: Finite element simulation of diffusive reaction in a porous substrate.

**Finite Element Simulation Results** To compare theoretical modeling and experimental results, we arbitrarily assumed four pairs of diffusive and binding constants close to the cellulose material under study. Though the exact numerical value may be far off from actual numbers presented by the cellulose environment, we can still draw a few conclusions on the diffusive binding behavior. First of all, with relatively slow diffusion  $D = 10^{-16}m^2/s$  and fast reaction  $R = 10\mu M^{-1}min^{-1}$ , the porous medium is not saturated at all. Upon contact, the number of bound ligands increases approximately linearly. This is a result of immediate binding of any available diffusive ligands. On the other hand, with

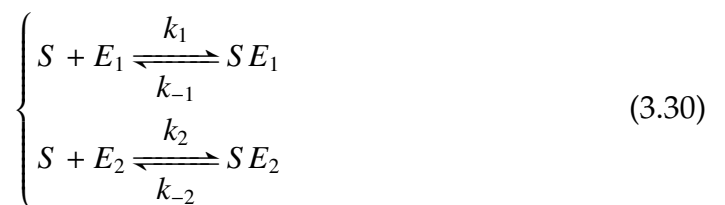
relatively fast diffusion  $D = 10^{-15}m^2/s$  and slow reaction  $R = 1\mu M^{-1}min^{-1}$ , we see a quick saturation of free ligands inside the porous material. The level of free ligands has to come to equilibrium with the ligand concentration in the presumed reservoir outside of the material.

### 3.6.3 Enzyme-Substrate Binding Model Involving Multiple Ligands on a Single Substrate

Finally, we consider transient analysis involving multiple enzymes binding to a single substrate. This analysis is relevant when both cellulose enzymes are endo-, or both are exo- cellulases competing for the same binding sites.

**Equations** In enzyme-substrate binding situations, when there are more than one enzyme species presented to a single species of substrate, and when both enzyme solutions are so dilute that the interactions among them can be ignored, we can assume they adsorb onto substrate independently. However the number of accessible sites on the substrate is limited, which leads to a competitive binding situation.

Ignoring catalytic activity of enzymes and only considering enzyme-substrate binding in a two-enzyme, one-substrate situation, we can write



where  $S$  stands for substrate,  $E_1$  and  $E_2$  are two species of enzymes,  $k_1$  and  $k_{-1}$  are forward and reverse binding rates of the first enzyme, and  $k_2$  and  $k_{-2}$  the

forward and reverse binding rates of the second enzyme, respectively.  $SE_1$  and  $SE_2$  are first and second enzyme-substrate complexes, respectively.

Denoting concentration of each reaction species using brackets, we can write the time-change of concentration of enzyme-substrate complexes as

$$\begin{cases} \frac{d[SE_1(t)]}{dt} = k_1[S(t)][E_1] - k_{-1}[SE_1(t)] \\ \frac{d[SE_2(t)]}{dt} = k_2[S(t)][E_2] - k_{-2}[SE_2(t)] \end{cases} \quad (3.31)$$

with initial condition  $[SE_1(0)] = [SE_2(0)] = 0$ .

In a fixed volume (or area), the maximum number of accessible sites  $[S^M]$  on a substrate is limited, and is the sum of available sites and occupied sites:

$$[S^M] = [S(t)] + [SE_1(t)] + [SE_2(t)] \quad (3.32)$$

or

$$[S(t)] = [S^M] - [SE_1(t)] - [SE_2(t)] \quad (3.33)$$

Substituting into differential equations above, we have a pair of coupled equations:

$$\begin{cases} \frac{d[SE_1(t)]}{dt} = k_1([S^M] - [SE_1(t)] - [SE_2(t)])[E_1] - k_{-1}[SE_1(t)] \\ \frac{d[SE_2(t)]}{dt} = k_2([S^M] - [SE_1(t)] - [SE_2(t)])[E_2] - k_{-2}[SE_2(t)] \end{cases} \quad (3.34)$$

which is a nonhomogeneous linear ordinary differential equation in the form of

$$\mathbf{v}' = \mathbf{A}\mathbf{v} + \mathbf{b} \quad (3.35)$$

where  $\mathbf{v}(t) = \begin{pmatrix} [SE_1(t)] \\ [SE_2(t)] \end{pmatrix}$ ,  $\mathbf{A} = \begin{pmatrix} -k_1[E_1] - k_{-1} & -k_1[E_1] \\ -k_2[E_2] & -k_2[E_2] - k_{-2} \end{pmatrix}$ , and  $\mathbf{b} = \begin{pmatrix} k_1[E_1][S^M] \\ k_2[E_2][S^M] \end{pmatrix}$ , with the initial condition  $\mathbf{v}(0) = \begin{pmatrix} 0 \\ 0 \end{pmatrix}$ .

The solution to equation 3.35 is given by  $\mathbf{v}(t) = \mathbf{v}_h(t) + \mathbf{v}_p(t)$ , where  $\mathbf{v}_h(t)$  is the solution to homogeneous equation  $\mathbf{v}' = \mathbf{A}\mathbf{v}$ , and  $\mathbf{v}_p(t)$  the particular solution to the nonhomogeneous equation 3.35 (14).

We first solve the homogeneous equation  $\mathbf{v}'_h = \mathbf{A} \cdot \mathbf{v}_h$ .

In order to find eigenvalues  $\lambda$  of  $\mathbf{A}$ , we set:

$$\det(\mathbf{A} - \lambda\mathbf{I}) = 0 \quad (3.36)$$

where  $\mathbf{I}$  is the identity matrix and  $\det()$  calculates the determinate of the argument, which gives,

$$\det \begin{pmatrix} k_1[E_1] + k_{-1} + \lambda & k_1[E_1] \\ k_2[E_2] & k_2[E_2] + k_{-2} + \lambda \end{pmatrix} = 0 \quad (3.37)$$

resulting in,

$$(k_1[E_1] + k_{-1} + \lambda)(k_2[E_2] + k_{-2} + \lambda) - (k_1[E_1])(k_2[E_2]) \quad (3.38)$$

$$= \lambda^2 + \lambda(k_1[E_1] + k_{-1} + k_2[E_2] + k_{-2}) + k_1[E_1]k_{-2} + k_2[E_2]k_{-1} + k_{-1}k_{-2} \quad (3.39)$$

$$= 0 \quad (3.40)$$

Therefore,

$$\lambda = -\frac{1}{2}(k_1[E_1] + k_{-1} + k_2[E_2] + k_{-2}) \quad (3.41)$$

$$\mp \frac{1}{2} \sqrt{(k_1[E_1] + k_{-1} + k_2[E_2] + k_{-2})^2 - 4(k_1[E_1]k_{-2} + k_2[E_2]k_{-1} + k_{-1}k_{-2})} \quad (3.42)$$

$$= -\frac{1}{2} \left( k_1[E_1] + k_{-1} + k_2[E_2] + k_{-2} \pm \sqrt{(k_1[E_1] + k_{-1} - k_2[E_2] - k_{-2})^2 + 4k_1[E_1]k_2[E_2]} \right) \quad (3.43)$$

Since all experimental values are non-negative, we have two distinct and real

eigenvalues of  $\mathbf{A}$ ,  $\lambda_1$  and  $\lambda_2$ , given by,

$$\lambda_1 = -\frac{1}{2} \left( k_1[E_1] + k_{-1} + k_2[E_2] + k_{-2} + \sqrt{(k_1[E_1] + k_{-1} - k_2[E_2] - k_{-2})^2 + 4k_1[E_1]k_2[E_2]} \right) \quad (3.44)$$

$$\lambda_2 = -\frac{1}{2} \left( k_1[E_1] + k_{-1} + k_2[E_2] + k_{-2} - \sqrt{(k_1[E_1] + k_{-1} - k_2[E_2] - k_{-2})^2 + 4k_1[E_1]k_2[E_2]} \right) \quad (3.45)$$

For  $\lambda_1$ , the eigenvector  $V_1$  satisfies  $(\mathbf{A} - \lambda_1 I)V_1 = \mathbf{0}$ . Here  $\mathbf{0}$  is a column vector.

And similarly for  $\lambda_2$ , there is an eigenvector  $V_2$  satisfying  $(\mathbf{A} - \lambda_2 I)V_2 = \mathbf{0}$ . Thus

$$\mathbf{V}_h(t) = (V_1 e^{\lambda_1 t}, V_2 e^{\lambda_2 t}) = (V_1, V_2) \begin{pmatrix} e^{\lambda_1 t} & 0 \\ 0 & e^{\lambda_2 t} \end{pmatrix} \triangleq (V_1, V_2) e^{\mathbf{J}t} \quad (3.46)$$

gives a basis for the solution of the system  $\mathbf{v}'_h = \mathbf{A} \cdot \mathbf{v}_h$  (14).

Using the *variation of parameters* (or *variation of constants*) method (4, 14), the complete solution to 3.35 is given by,

$$\mathbf{v}(t) = \mathbf{V}_h(t)\xi + \mathbf{V}_h(t) \int_0^t \mathbf{V}_h^{-1}(\tau)\mathbf{b}d\tau \quad (3.47)$$

Since  $\mathbf{v}(0) = \mathbf{0}$ , we have  $\xi = \mathbf{0}$ . Therefore,

$$\mathbf{v}(t) = (V_1, V_2) \begin{pmatrix} e^{\lambda_1 t} & 0 \\ 0 & e^{\lambda_2 t} \end{pmatrix} \int_0^t e^{-\mathbf{J}\tau} d\tau (V_1, V_2)^{-1} \mathbf{b} \quad (3.48)$$

$$= (V_1, V_2) \begin{pmatrix} e^{\lambda_1 t} & 0 \\ 0 & e^{\lambda_2 t} \end{pmatrix} \begin{pmatrix} \frac{1}{-\lambda_1}(e^{-\lambda_1 t} - 1) & 0 \\ 0 & \frac{1}{-\lambda_2}(e^{-\lambda_2 t} - 1) \end{pmatrix} (V_1, V_2)^{-1} \mathbf{b} \quad (3.49)$$

$$= (V_1, V_2) \begin{pmatrix} \frac{1}{\lambda_1}(e^{\lambda_1 t} - 1) & 0 \\ 0 & \frac{1}{\lambda_2}(e^{\lambda_2 t} - 1) \end{pmatrix} (V_1, V_2)^{-1} \mathbf{b} \quad (3.50)$$

We see the same method can be extended to situations where there are more than two species of enzymes.

### **3.7 Future Studies**

In this project, we have studied fluorescently-labeled cellulases adsorption to pretreated cellulose particles. We also simulated labeled cellulase using dextran particles of sizes similar to those of cellulases, given that dextran particles do not interact chemically with cellulose particles, but only diffuse through the porous structure of the cellulose. We found that adsorption of cellulases is a much faster process than diffusion process. However, determining the exact rate was hindered by the large variation in morphology of the pretreated material. Therefore for future studies using confocal scanning microscopy, we should concentrate on materials with a more uniform morphology. On the other hand, in studying pretreated material with large variations in shapes and sizes, and crevices, we should study them in large numbers in order to obtain a reasonable statistical average and small standard deviation.

## **Chapter 4**

# **Optical Properties of Zero-Mode Waveguides**

## 4.1 Introduction

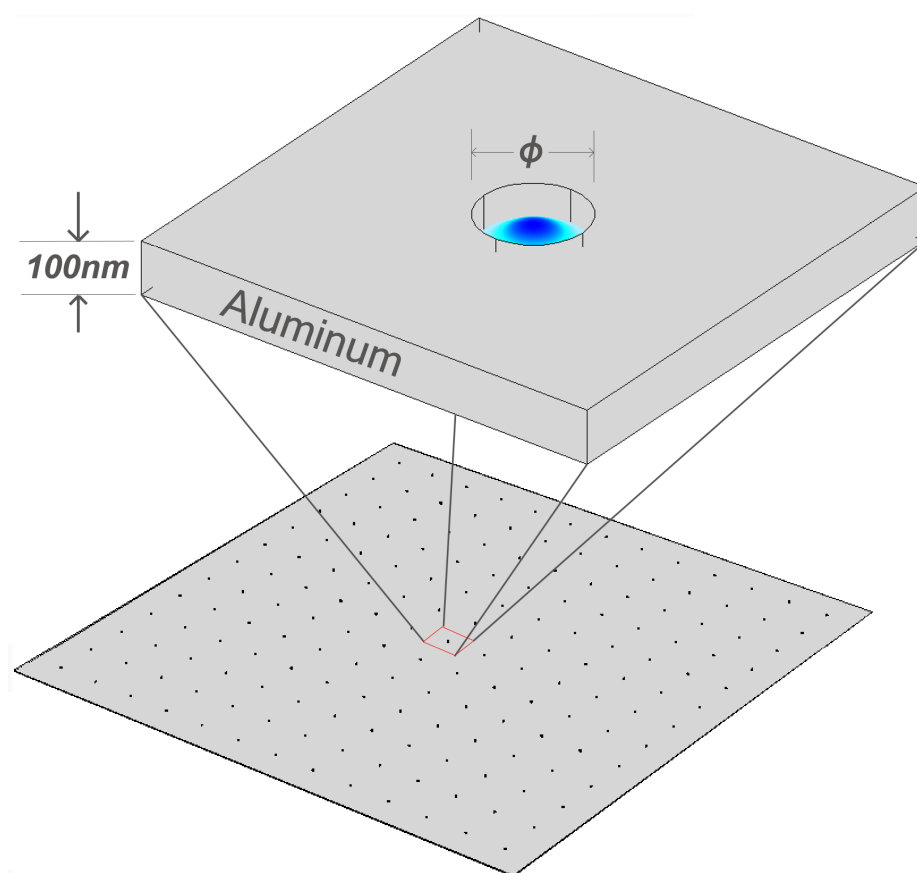


Figure 4.1: Illustration of Zero-Mode-Waveguide devices.

One method to increase signal-to-noise ratio in fluorescent single molecule studies is to minimize unwanted background fluorescence. Since detected fluorescence comes from total number of fluorescent molecules inside a volume, one way to study a single molecule while decreasing fluorescence from all other molecules without lowering excitation light, is decreasing fluorescence from all other molecules. This is achieved by limiting the total number of molecules

being simultaneously illuminated, by either lowering the concentration of fluorescent molecules in the illumination volume, or reduce the illuminated volume itself.

On the other hand, for many physiologically relevant interactions, it is necessary to keep ligand and substrate at micro-molar or higher concentrations (84). For single molecule studies at these concentrations, it is necessary to limit illumination volume to zepto-liter ( $10^{-21}$  Liter) range (49).

Zero-Mode-Waveguides (ZMWs), drawn in Fig. 4.1, are sub-wavelength apertures milled in metal cladding and supported by optically clear substrate. ZMWs reduce illumination volume by geometrically limiting the physical volume, and further optically limiting the penetration of the electromagnetic energy inside the aperture. The diameter  $\phi$  can be made as small as  $\sim 60nm$ . With a height of  $100nm$ , the cylindrical volume of the ZMW is on the order of attoliter. More importantly, ZMWs' optical property confines optical energy close to the entrance of the aperture. For wavelenghtes longer than those allowed for propagation, light enters the apertures only to be exponentially attenuated, leading to non-transmission mode, or zero-mode.

Usually the metal cladding is made of aluminum, for its best conductance and therefore the best reflectivity in the visible wavelength. Gold has been used where bio-compatibility and chemical resistance were required (51). However gold starts to lose its reflectivity for wavelenghtes shorter than  $400nm$ . Plasmonic excitation of gold and light re-emission can occur at approximately  $500nm$ , which leads to a rich field for plasmonic studies, but limits the choice of fluorophores if the fluorescence of molecules is of prime interest (75). Although silver has similar optical properties as aluminum, and apertures in silver has

been studied extensively (16), it is easily oxidized and blackened. Therefore silver has not been used in making ZMWs for biological reactions. Chromium, though chemically more resistant than silver and aluminum, has lower reflectivity, i.e, smaller refractive index, and does not block optical energy well at the visible wavelength. Indeed, ZMW devices made with 100nm-thick chromium appear slightly transparent to the eye, though their exact transmission rate over the visible spectrum remains to be characterized.

## 4.2 Motivation

There are two regions of ZMW that we need to explore the optical properties: First, the optical energy inside an aperture determines how a fluorescent molecule is excited, and how much fluorescence emission is coupled back out of the aperture that can be collected by the photon detector. This illumination profile dominates detectable signal trace in time. Second, we are interested in the optical energy coupled through the ZMWs. Not only is light transmission through a sub-wavelength aperture an area of interesting study, it can excite fluorophores in the vast region of open solution, which can contribute to background photon counts. For fluorescence studies interested in observing biological phenomenon inside the aperture, background illumination, in other words transmitted light, should be minimized to enhance signal to noise ratio.

For fluorescent single-molecule studies using ZMWs, light transmitted through the apertures is responsible for the majority of background fluorescence. Even though optical energy has been greatly attenuated through the aperture, the number of molecules it can excite in the bulk fluid is orders of

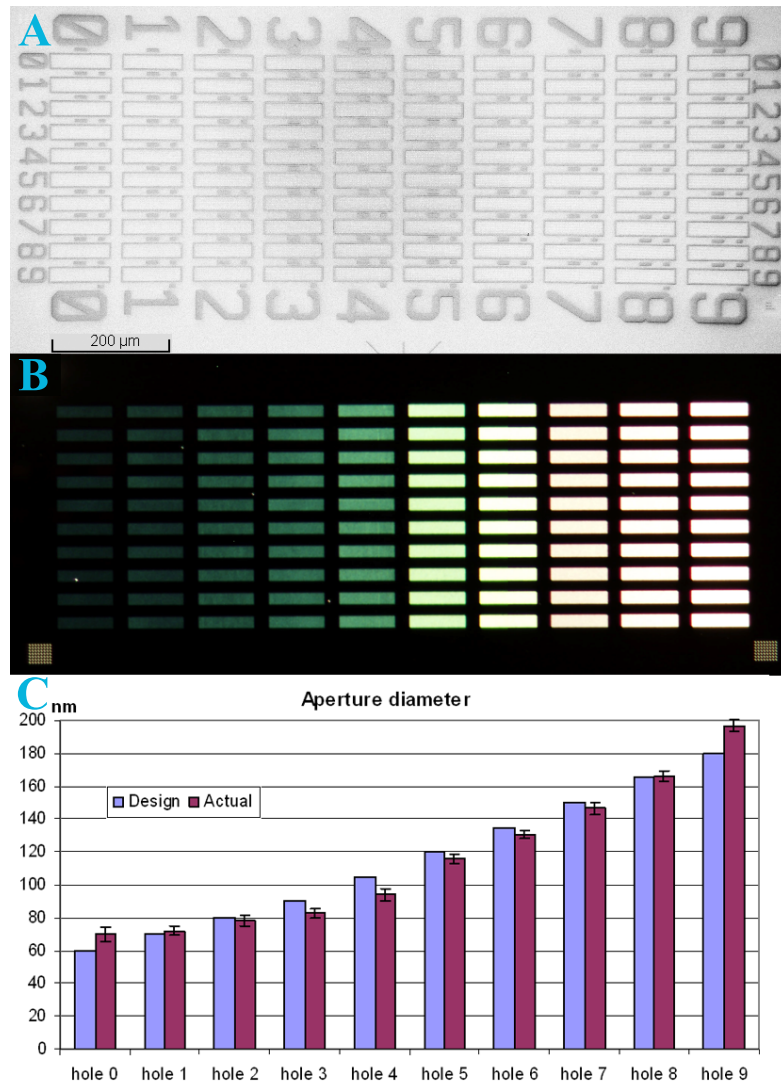


Figure 4.2: A. SEM image of arrays of ZMWs of increasing sizes from “0” to “9”, Numbers and rectangles visible in this image are fabricated in gold to enhance contrast. Numbers designate column and row, while rectangles enclose ZMW arrays; B. Color image of transmitted light from an incandescent bulb. ZMWs with larger diameters pass more longer wavelength light than those with smaller diameters; C. Measured ZMW diameters compared to design size, from “0” to “9”.

magnitude larger than that inside the ZMW. In addition to the field of plasmonics, there is interest in using light passing through ZMWs as near-field light source to study lipid membrane-bound single molecules (39). Recently, negative resist SU-8 has been used in revealing light intensity profile outside of nanoapertures (1).

Three-dimensional simulation has provided numerical solution to the electromagnetic field in- and outside the ZMWs, indicating the existence of an evanescent wave with quick attenuation along the direction of transmission (49). However to our knowledge, there has been little experimental confirmation that demonstrated this theoretical result. The experimental difficulty lies in the fact that any probe inside the ZMW that can detect the field must be small and approaching an infinitesimal dipole so as not to alter the surrounding field significantly. And secondly, the locations of these probes must be known to a great accuracy in order for the experimenter to map the electric field inside the aperture. Since our field of interest is inside a sub-wavelength aperture, the only probes that are small enough to map the field have to be at the molecular scale. And since we are working with electromagnetic waves in the optical range, either photo-sensitive or optically detectable molecules are our primary choice.

In this chapter, we first look at the fabrication techniques used in making these sub-wavelength apertures. Next we provide a solution of electromagnetic field, both theoretically for a perfect metal structure in the cylindrical coordinate, and then numerically for the fabricated structure, using actual material's optical constants. Finally we compare experimental measurements with calculated results.

### 4.3 Fabrication of Zero-Mode Apertures

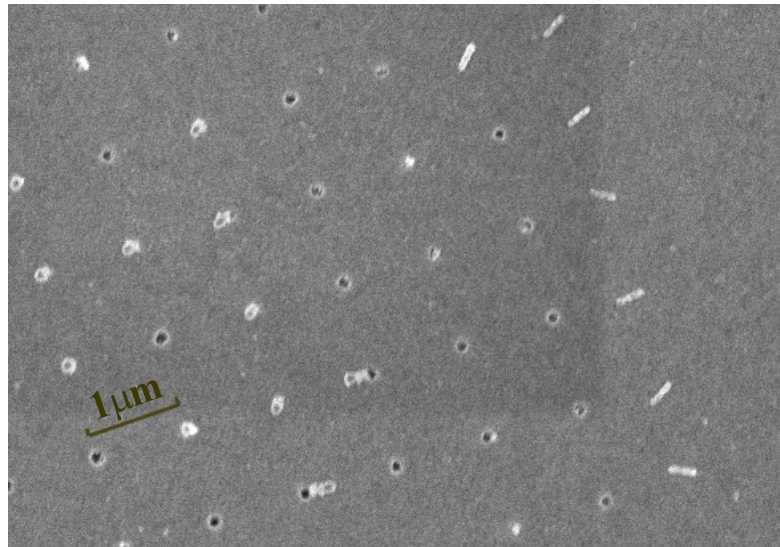


Figure 4.3: SEM image of an array of ZMWs at  $1\mu\text{m}$  spacing, showing apertures (black circular holes) in aluminum where e-beam resist pillars have lifted off; and where resist pillars still remain, with aluminum covering their tops (bright spots); and where the pillars have fallen flat on the substrate surface during the e-beam resist developing stage and were subsequently covered by deposited aluminum.

**Fabrication of Zero Mode Waveguides** Various methods have been used to fabricate sub-micrometer apertures on metal films. The straight forward way of making apertures in metal is to evaporate metal film on a clear substrate first, and then produce the apertures by, for example, focused-ion-beam (FIB) milling (16,104), or reactive ion etching into masked aluminum film (49). Alternatively, the positions of the apertures can be defined first with self-assembled nano-sized beads (23), or positive electron-beam resist on the substrate, which are subsequently dissolved after metal deposition, resulting a void where the placeholder used to be. Recently, a nanoimprint lithography step followed by metal lift-off method was also introduced (101).

Each fabrication method has its own advantages and drawbacks. FIB milling can create apertures of various sizes and locations in an optically thick film. The location and depth of milling are under experimenter's precise control. However this method creates one aperture at a time, therefore is relatively slow and inefficient, compared to self-assembled nano-sphere lithography (NSL). NSL creates large number of apertures very efficiently and inexpensively, but lacks the precision of location and size achievable by mechanical patterning techniques such as electron beam lithography. Compared to a negative-resist metal lift-off method, reactive ion etching uses a positive electron beam resist to define aperture positions on top of an aluminum film, and subsequently etches apertures into the aluminum. Both methods are large scale parallel fabrication that results in large number of precisely controlled and spaced apertures on a film. Both are efficient, compared to FIB, but more expensive compared to NSL, because of the electron-beam patterning step. In our fabrication, we have used the negative-resist and metal lift-off method as described by Foquet *et al* (24). Compared to reactive ion-etching, lift-off method gives cost-effective ZMW arrays with a clean and smooth glass substrate.

The fabrication process is briefly repeated here:  $170\mu\text{m}$  fused silica wafer is first cleaned in ammonium hydroxide with hydrogen peroxide solution and then in hydrogen chloride with hydrogen peroxide solution at  $70^\circ\text{C}$ , each for 10 minutes. Cleaned wafer is rinsed and dried under nitrogen stream. Negative electron-beam resist NEB-31A is then spin-coated onto the fused silica surface at  $4000\text{rpm}$  for 60 seconds, and baked at  $115^\circ\text{C}$  for 2 minutes to drive out the solvent. At this spin speed and pre-exposure bake temperature, the thickness of the resist is approximately  $400\text{nm}$ . A  $7\text{nm}$  layer of gold is thermally evaporated onto the surface of the resist as a minimum-thickness conductive layer

for charge dissipation during electron beam exposure. Electron beam exposure is done in Jeol9300, with a current between 1 and 2nA, at acceleration voltage of 100kV. Since NEB-31A is a chemically amplified negative e-beam resist, a post-exposure bake step via contact-hotplate at 90 °C for 2 minutes is needed to promote cross-linking reaction. Top layer gold is then etched away by immersion in gold etchant type TFA (Transene, Danvers, MA) for 10 seconds. Wafer is rinsed with de-ionized water, and developed in aqueous developer MF-321 (Shipley, Marlborough, MA) for 40 seconds, again rinsed, and dried under nitrogen stream.

Exposed areas of resist remains on the surface of the wafer. Since the area of each exposure is small, the resist remain as pillars, with diameter on the order of 100nm, and height at 400nm. Pillars with diameters smaller than 60nm tend to fall flat onto the fused silica surface (Fig. 4.3) and do not result in final apertures.

~ 100nm Aluminum is thermally evaporated onto the fused silica substrate at pressures below  $2 \times 10^{-6}$  Torr using CVC SC4500 evaporator. A quartz crystal is used to monitor the thickness of the evaporated metal. Post-fabrication AFM measurements of aluminum thickness agrees well with quartz crystal monitor reading.

A protective coating of photo-resist, typically Shipley S1827 (Shipley, Marlborough, MA), is spin-coated onto the aluminum layer, and the 170 $\mu$ m fused silica substrate is diced into easily handled devices. Before use, each ZMW device is cleaned in acetone and isopropyl alcohol, and left in resist remover (Shipley 1165) over night to dissolve e-beam resist pillars. Gentle sonication is used in the lift-off process to clean the apertures of resist. Final device is rinsed in deionized water, dried under nitrogen stream, and subject to gentle oxygen

plasma clean for 30 seconds before experiment.

## 4.4 Characterize Zero Mode Waveguides

### 4.4.1 Several aspects of Zero Mode Waveguides

Zero Mode Waveguides, depending on how they are fabricated, have different physical properties, namely, hole size/diameter, array spacing, and uniformity. First of all, since Zero-Mode Waveguides are almost always fabricated in an array, and never in isolated form, the array spacing is an important parameter to consider. As shown by Ebbeson *et al*, periodic hole arrays may preferentially transmit light at certain wavelengths (19). Secondly is their physical size, which includes height/thickness of aluminum, and the diameter of the apertures. Thirdly is their shape, i.e, if the vertical cross-section is purely cylindrical or a cone shape, and if the transverse cross-section is rounded circular. We will discuss each of these physical properties below.

**Array spacing of ZMW Devices** We fabricate ZMW arrays with 2, 5, or 10 $\mu\text{m}$  spacing. These values are compromises for different ZMW applications. Ideally, one would like to have an isolated aperture in order to minimize background that could be collected in the field of view. However such isolated features will be difficult to identify on an aluminum film, and can easily be confused with a defect in the film. In addition it will be difficult to co-localize interesting biological phenomenon with an isolated aperture. Therefore it is beneficial to maximize the number of apertures while at the same time, minimize the background

that can be collected in the field of view. Therefore  $5\mu\text{m}$  spacing is chosen, such spacing gives approximately  $27 \times 27$  bright spots per field of view using a  $60\times$  water immersion objective with a  $512 \times 512$  pixel array EMCCD camera.

Occasionally  $2\mu\text{m}$  spaced apertures arrays are used when the physiological activities under study are on the membrane or inside a living cell. Such arrays in fact form grids that can be used to identify cells on the other side of an otherwise opaque metal layer.

$10\mu\text{m}$  spacing array of ZMW is used as a further compromise between locating an aperture and minimizing transmitted light from any aperture other than the one under measurement.

**Size of Fabricated ZMW Devices** The dominating factor of fabrication that determines the size of the resulting aperture is electronic exposure, or total dose per fabrication spot. Although the freshness of the resist, pre- and post-exposure temperature and time also play a role. During the e-beam exposure process, accelerated electrons forward-scatter through resist and strike the fused silica substrate. Only a fraction of the forward-scattered electrons lead to cross-linking of the resist, the rest undergo backscattering and their resulting secondary electrons can cause further cross-linking of resist in the neighborhood of the focal spot, leading to proximity effect and expansion of the pattern.

When drawn on a computer aided design (CAD) software, ZMW devices are designed to be much smaller than their final diameter. One version of CAD drawing of ZMWs designated each aperture with a single exposure dot, corresponding to a 5-nm resolution of the exposure tool. An alternative CAD drawing of ZMWs used multiple  $5\text{nm}$  dots to designate a single aperture. There were

no noticeable differences of the final aperture using these two CAD drawings. The determining factor for the resulting aperture size is the total electron dose for an aperture.

Fabricated devices are examined with scanning electron microscopes (SEMs). Diameters of apertures on aluminum film are measured directly on SEM images. Five apertures are measured and diameters recorded for each designed size. Their average is taken to be the average for that design and exposure dose, and their standard deviation calculated to illustrate size distribution. By comparing ZMW size and actual applied electron beam dose, we obtain an empirical threshold of exposure  $Q_{\text{TH}}$  relating total exposure of electronic charge  $Q_{\text{TOTAL}}$  to the resulting aperture diameter  $\phi$ .

$$\frac{2 \cdot Q_{\text{TOTAL}}}{\sqrt{2\pi}\sigma} e^{-\frac{\phi^2}{8\sigma^2}} = Q_{\text{TH}} \quad (4.1)$$

where  $\sigma$  denotes pattern expansion constant for our resist and substrate.

In one incidence of fabrication, we obtained  $\sigma = 34.69 \pm 1.84\text{nm}$  and  $Q_{\text{TH}} = 384.4 \pm 36.3\mu\text{C}/\text{cm}^2$ .

Since NEB-31A is a chemically amplified negative resist, the post-exposure bake affects the resulting pattern. Although we did not characterize the exact effect of post-bake temperature and time, we have been consistent with manufacturer's recommended recipe, in order to obtain repeatable results.

We note the freshness of e-beam resist NEB-31A can also affect the resulting aperture. In one occasion, resist that was a year beyond its expiration date produced patterns that were hard to lift off and cross-linked resist pillars were not

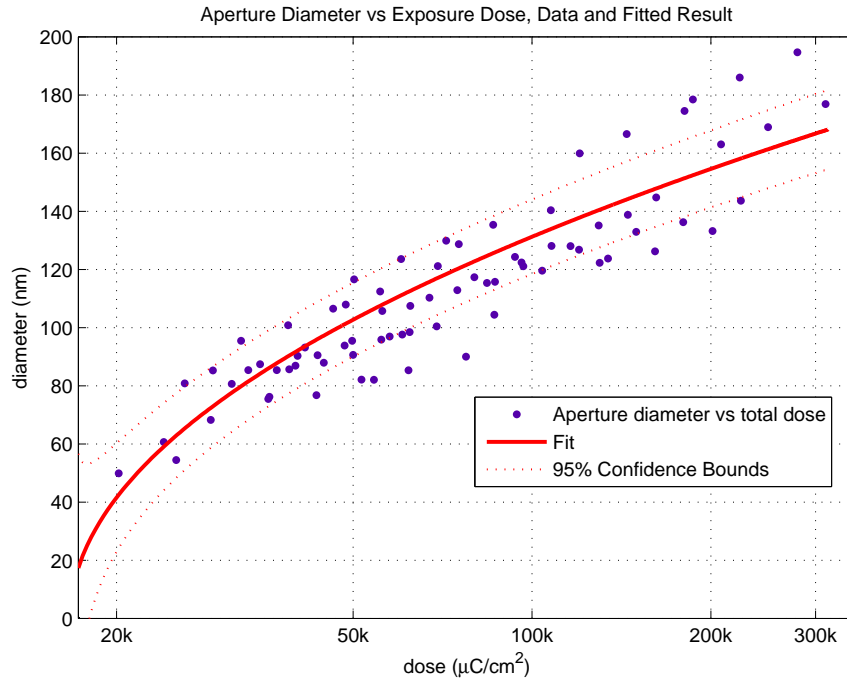


Figure 4.4: Resulting aperture diameter is a function of total dose and expansion factor  $\sigma$ .

completely dissolving in 1165.

**Shape of ZMW Apertures** Aluminum layer is deposited via thermal evaporation after e-beam resist pillars have been defined. Aluminum not only adheres to fused silica substrate, but also sticks to resist pillars. Consequently, any aluminum that is accumulated on the top of the resist pillars tends to grow in size and, together with the pillar itself, forms a shadow for the aluminum layer on the substrate. The resulting device before lift-off, as shown in Fig. 4.5, appears to have a muffin-top.

The shadowing effect of the “muffin top” can be seen more clearly in Fig. 4.6. The cross-section shows developed NEB-31A pillar is surrounded by alu-

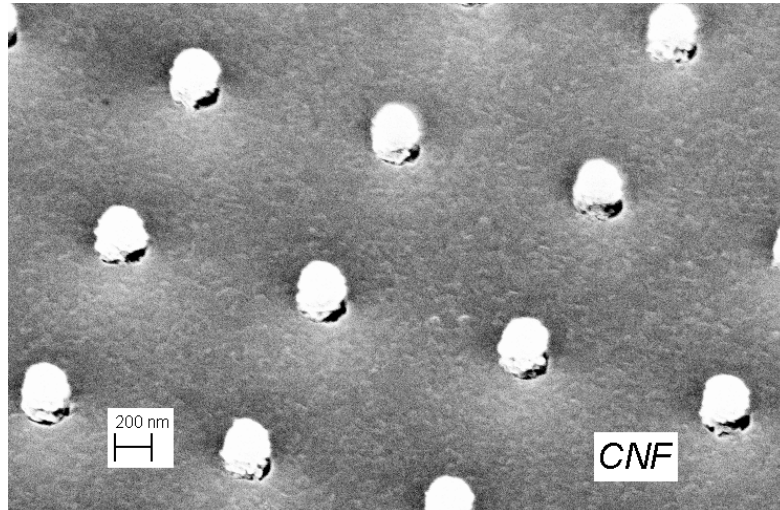


Figure 4.5: Evaporated aluminum on top of pillars, creating a shadow for what's below.

minum. Yet the gap between aluminum and resist pillar is formed because aluminum was blocked from this region.

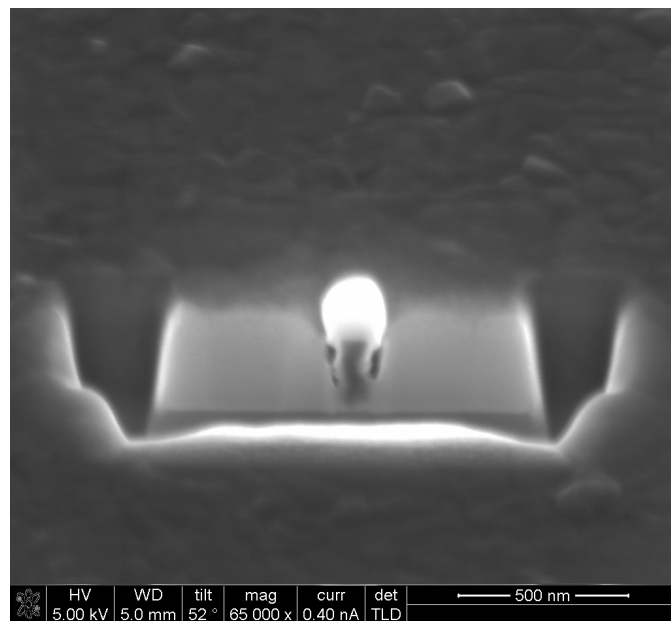


Figure 4.6: Focused-Ion-Beam cross-section cut showing pillar formed by developed NEB-31A before lifting off.

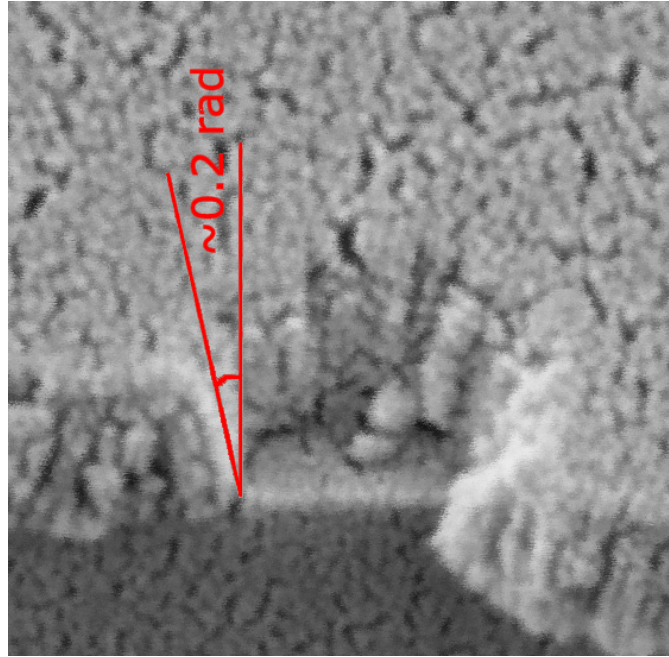


Figure 4.7: SEM Image of a cross-section of a Zero-Mode-Waveguide device, showing approximately 0.2 radian sloped aluminum side-wall. The diameter of the aperture is approximately 150nm.

As a result, ZMW devices fabricated using metal lift-off method will have a conic shape inside, and a slightly slanted aluminum wall. From SEM image 4.7, we estimate the slope of the side wall is approximately 0.2 radians, wider at the top.

## 4.5 Electromagnetic Solution of Zero-Mode Apertures

### 4.5.1 Wave Solution in Cylindrical Coordinates

The propagation of light in macroscopic medium satisfies Maxwell's equations (in SI units):

$$\begin{aligned}\nabla \cdot \mathbf{B} &= 0 \\ \nabla \cdot \mathbf{D} &= \rho \\ \nabla \times \mathbf{E} + \frac{\partial \mathbf{B}}{\partial t} &= 0 \\ \nabla \times \mathbf{H} - \frac{\partial \mathbf{D}}{\partial t} &= \mathbf{J}\end{aligned}\tag{4.2}$$

where  $\mathbf{E}$  and  $\mathbf{H}$  are the macroscopic electric and magnetic fields,  $\mathbf{D}$  and  $\mathbf{B}$  are the electric displacement and magnetic induction fields, and  $\rho$  and  $\mathbf{J}$  are the free charge and current densities, respectively (31).

Material properties affect the solution of these equations. First of all, magnetic field  $\mathbf{B}(\mathbf{r})$  is related to  $\mathbf{H}(\mathbf{r})$  in that  $\mathbf{B}(\mathbf{r}) = \mu(\mathbf{r})\mathbf{H}(\mathbf{r})$ , where  $\mu(\mathbf{r})$  is the material permeability. For most dielectric materials, the permeability is close to that of vacuum, or  $\mu_0 = 4\pi \times 10^{-7} \text{Henry/m}$ . For simplicity, we use  $\mathbf{B}(\mathbf{r}) = \mu_0\mathbf{H}(\mathbf{r})$ .

For linear and isotropic media, the displacement field  $\mathbf{D}(\mathbf{r}, \omega)$  is related to the electric field  $\mathbf{E}(\mathbf{r}, \omega)$  by a scalar dielectric function  $\epsilon(\mathbf{r}, \omega)$  known as the permittivity, where  $\omega$  is frequency of electromagnetic wave. Here we have specifically noted the spatial ( $\mathbf{r}$ ) dependence of each variable.

These four equations are not independent of one another. After a series of manipulations (see for example, (11)), we have the following homogeneous vec-

tor wave equations for a source-free region,

$$\begin{cases} \nabla^2 \mathbf{H} - \mu\epsilon \frac{\partial^2}{\partial t^2} \mathbf{H} = 0, \\ \nabla^2 \mathbf{E} - \mu\epsilon \frac{\partial^2}{\partial t^2} \mathbf{E} = 0. \end{cases} \quad (4.3)$$

In general, the wave solution to the Helmholtz's equation

$$\nabla^2 \mathbf{E} - \gamma^2 \frac{\partial^2}{\partial t^2} \mathbf{E} = 0 \quad (4.4)$$

is

$$\mathbf{E} = \hat{\mathbf{x}} E_0 e^{-\gamma z} = \hat{\mathbf{x}} E_0 e^{-\alpha z} e^{-j\beta z} \quad (4.5)$$

where we have arbitrarily defined the plane wave's direction of propagation as  $+z$  and polarization to be in the  $x$ -direction. Both  $\alpha$  and  $\beta$  are positive constants.  $\alpha$  is a non-negative attenuation constant;  $\beta$  is a non-zero propagation constant. Since

$$\gamma = \alpha + j\beta = j\omega \sqrt{\mu\epsilon}, \quad (4.6)$$

and  $\epsilon(\mathbf{r}, \omega)$  is material dependent, the solution  $\mathbf{E}$  must satisfy boundary conditions at all material interfaces.

In optics, complex refractive indices  $\tilde{n} = n + i\kappa$  are often used to describe the optical properties of a material. where  $\epsilon = \tilde{n}^2$ . In fact optical phenomenon in our structures can be completely described by electromagnetic theory above.

Since ZMWs are constructed in circular shape, the obvious choice of coordinate system to use is cylindrical, where the geometry does not support a transverse electromagnetic (TEM) wave, but only a transverse electric (TE) or transverse magnetic (TM) wave, separately (11).

### TM wave solution

$$\begin{cases} H_z = 0 \\ E_z(r, \phi, z) = E_z^0(r, \phi)e^{-\gamma z} = C_n J_n(hr) \cos n\phi \end{cases} \quad (4.7)$$

where  $C_n$  is an arbitrary constant, and  $J_n(hr)$  is the Bessel function of the first kind of  $n$ th order with an argument  $hr$ , defined as

$$J_n(hr) = \sum_{m=0}^{\infty} \frac{(-1)^m (hr)^{n+2m}}{m!(n+m)!2^{n+2m}} \quad (4.8)$$

$E_z^0$  must vanish at the perfect conductor boundary. Therefore

$$J_n(ha) = 0 \quad (4.9)$$

where  $a$  is the radius of the cylinder. The eigenvalue for the  $TM_{01}$  mode that corresponds to the first zero of  $J_0(ha)$  is

$$h_{TM_{01}} = \frac{2.405}{a} \quad (4.10)$$

and the corresponding cut-off wavelength is

$$\lambda_{TM_{01}} = \frac{2\pi \sqrt{\mu_r \epsilon_r}}{h_{TM_{01}}} = 2.613a \sqrt{\mu_r \epsilon_r} \quad (4.11)$$

### TE wave solution

$$\begin{cases} E_z = 0 \\ H_z(r, \phi, z) = H_z^0(r, \phi)e^{-\gamma z} = C'_n J_n(hr) \cos n\phi \end{cases} \quad (4.12)$$

where the boundary condition requires the normal derivative of  $H_z^0$  must be zero on the wall of the perfect conductor, that is

$$J'_n(ha) = 0. \quad (4.13)$$

The eigenvalue for the  $TE_{11}$  is

$$h_{TE_{11}} = \frac{1.841}{a}, \quad (4.14)$$

giving the cut-off wavelength

$$\lambda_{\text{TE}_{11}} = \frac{2\pi \sqrt{\mu_r \epsilon_r}}{h_{\text{TE}_{11}}} = 3.413a \sqrt{\mu_r \epsilon_r} \quad (4.15)$$

**Cut-off Wavelength** We see in a cylindrical waveguide,  $\text{TE}_{11}$  represents the lowest mode with the largest cut-off wavelength  $\lambda_c$ . In addition,  $\lambda_c$  increases when there is dielectric material  $\epsilon_r > 1$  that fills the waveguide.

However the above solutions are only valid for perfect metal. For real metal with finite conductivity, boundary conditions do not require equations 4.9 and 4.13 to vanish. Therefore there is not a sharp and definite cut-off wavelength. The actual solution inside the waveguide is a combination of TE and TM modes, with finite attenuation along the direction of propagation. The actual solution, however, can only be obtained using numerical methods.

## 4.5.2 Numerical Solution Using Finite Element Methods

**Geometric Properties** To obtain sensible numerical solution of Maxwell's equations, it is essential that we model our ZMW structures correctly. This includes correctly defining the geometric features that allow sufficiently accurate solution within reasonable computing power.

Figure 4.8.A shows geometric drawing of a ZMW device. The overall volume is roughly 3 times the size of the ZMW aperture, plus a surrounding perfectly matched layer (PML) that minimizes reflected wave. Therefore the overall dimension of the geometry is on the order of one wavelength. The mid-section of the geometry is a 100-nm aluminum layer, supported by a fused silica (undoped  $\text{SiO}_2$ ) substrate below, and filled with dielectric filling inside and above

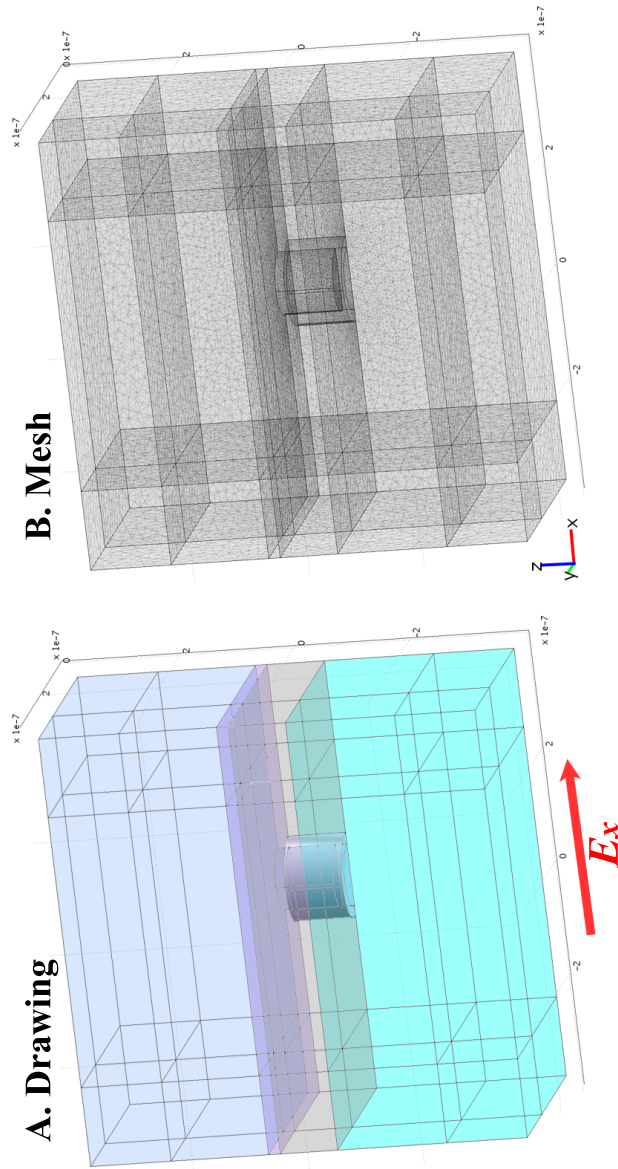


Figure 4.8: ZMW simulation model used in COMSOL. Electric field is arbitrarily defined to be polarized in the  $x$  direction. A. Geometric drawing of half a device showing fused silica substrate, aluminum cladding, ALD layer dielectric, and aqueous filling above the ZMW; B. Meshing divides the geometry into 700,000 piece-wise linear elements. Corners and curves are segmented with finer elements, whereas coarse elements are used for the open volume.

the ZMW. The dielectric constant is that of water, simulating the aqueous environment used in actual experiments. When there is atomic layer deposited material covering a layer just above and inside the ZMW, as drawn, the dielectric constant of the ALD layer is taken to be that of the aluminum oxide. The ALD layer thicknesses used in simulations vary from 5nm to 25nm.

**Meshing** COMSOL divides the geometry into very small and piecewise linear segments in order to arrive at a numerical solution of the wave equation supported by the geometry. The smallest elements are in and around the corners of the drawing. Coarse segments are used in the larger and continuous volume, in order to speed calculation (Figure 4.8.B). On average, each geometry contains between 500,000 and 700,000 elements, and each solution run (error less than  $10^{-6}$ ) takes less than 1 hour.

**Symmetry Argument** We arbitrarily defined the plane wave to be polarized in the  $x$  direction. Therefore the wave solution is symmetric with respect to the  $y$ -axis. We take advantage of this symmetry and only simulate the  $+y$  half of the geometry. Compared to a full geometry simulation model, this drastically lessens the memory requirement and computing time. We note, symmetry argument dictates the  $y = 0$  boundary be defined as a “perfect magnetic conductor”.

**Material Properties** There are four basic materials used in modeling the ZMWs: fused silica substrate, aluminum (or other metal) that makes up the cladding, aluminum oxide that represents the ALD layer, and aqueous layer that fills inside and above the ZMWs. PML domains simply set up attenuation constant inside respective materials in order to minimize reflected wave. For

all materials except water, we measured their refractive indices using Woollam ellipsometer (J. A. Woollam, Lincoln, NE).

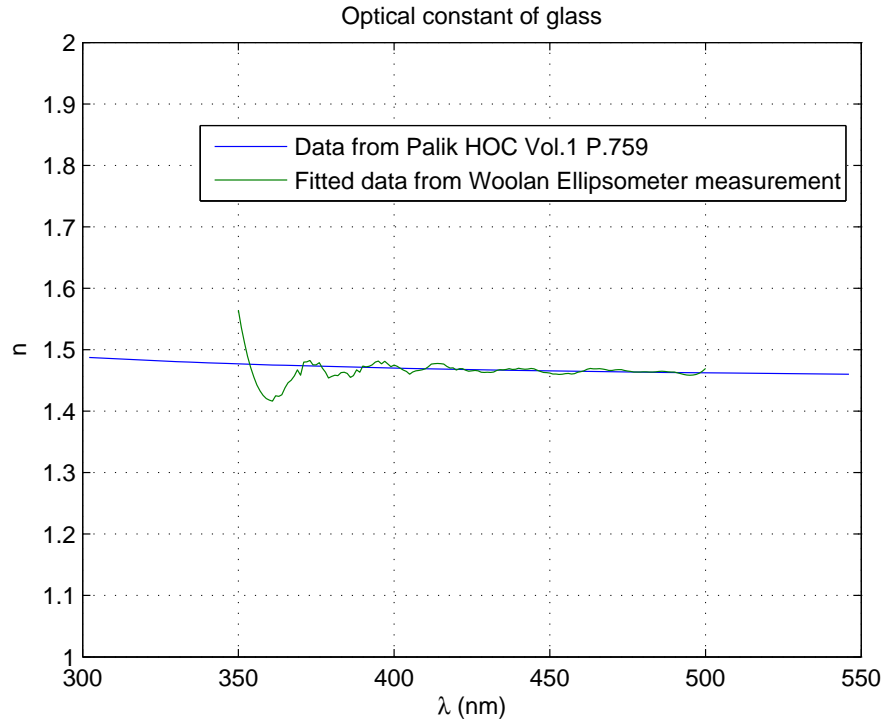


Figure 4.9: Refractive index of  $\text{SiO}_2$ , measured from  $170\mu\text{m}$  fused silica wafer.

**Fused Silica Substrate** Fused silica showed remarkable constant refractive index in the visible range. We used  $n_{\text{SiO}_2} = 1.47$  in our simulations.

**Aluminum** From profilometer measurement, we know our deposited aluminum layer is  $100 \pm 5\text{nm}$ . Using this thickness in ellipsometry fitting, we obtain the result shown in Figure 4.10.

After evaporated aluminum has been exposed in the air for days, there is a native oxide layer that exists on the aluminum surface. The ellipsometry fitting

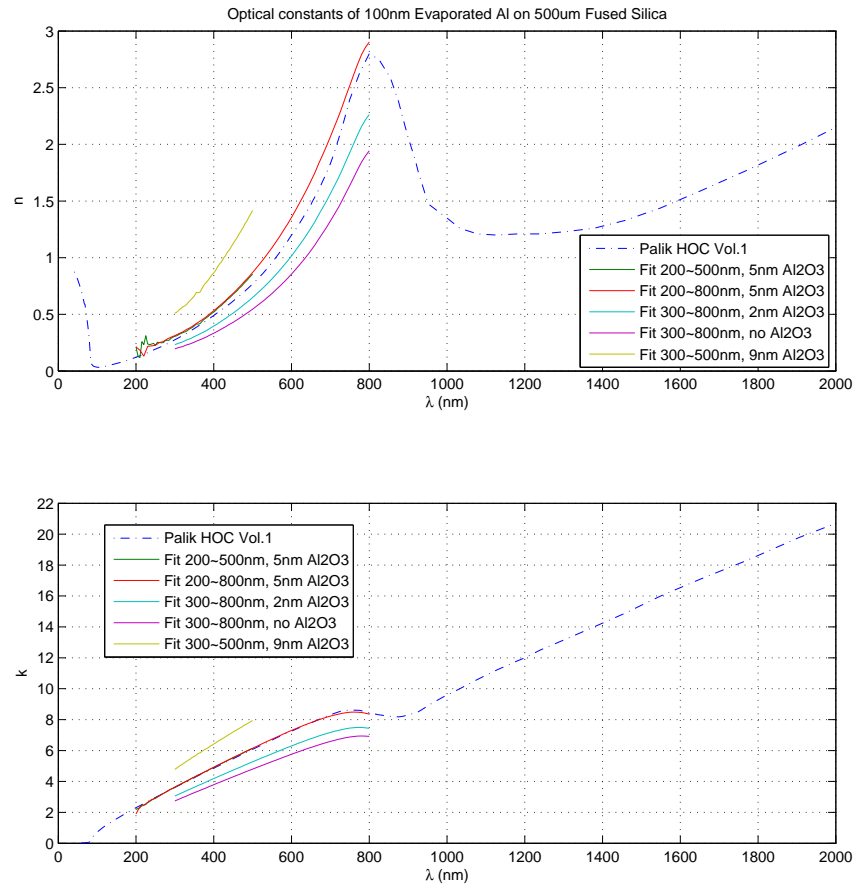


Figure 4.10: Optical constants of thermally evaporated aluminum. Complex refractive index is wavelength dependent and is written as  $\tilde{n} = n - ik$ .

model assumed a top layer aluminum oxide between 2 and 5 nanometers thick, which gives good fitting results.

However due to the small numerical value of the thickness of the native oxide layer and the difficulty in resolving small features in finite element methods, we do not explicitly include a native aluminum oxide layer in our simulations.

**Aluminum Oxide** We postpone the discussion of  $\text{Al}_2\text{O}_3$  till section 4.7.2.

## 4.6 Simulation Results

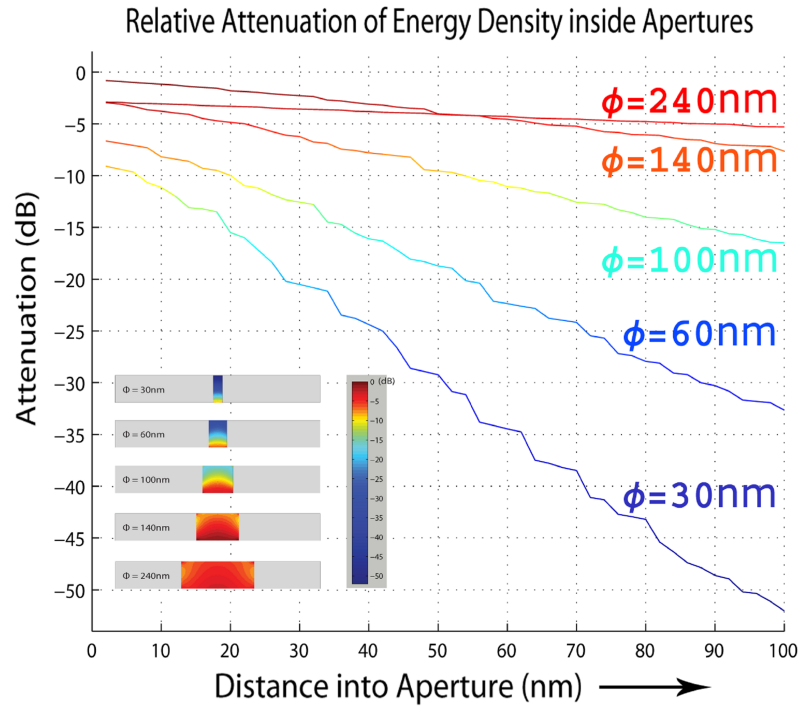


Figure 4.11: Simulated result of attenuation of energy density along the central axis of transmission inside ZMW. Inset shows corresponding color plot of energy density on the same color scale.

**For various aperture diameters** Fig. 4.11 shows relative attenuation of energy density inside apertures, with plane incident wavelength at 488nm. The smallest aperture, with diameter  $\phi = 30\text{nm}$ , though never successfully fabricated using lift-off method, has the greatest attenuation along the direction of transmission. Comparatively, the largest aperture, with  $\phi = 240\text{nm}$ , is no longer considered “zero-mode”, and shows very little attenuation. Interestingly, aper-

ture with diameter  $\phi = 140\text{nm}$  has the highest energy density at the entrance. We think this is a result of energy concentration due to proximity to the edges of the metal, similar to that of the standing wave effect when an electromagnetic wave hits a metallic boundary, and forms a “node” approximately quarter wavelength away from the boundary.

For each decay curve, we can fit an exponential decay model  $I(z) = I_0e^{-\eta z}$ , assuming  $z = 0$  at the entrance, and compare the exponential decay constants between various aperture sizes and among different metals.

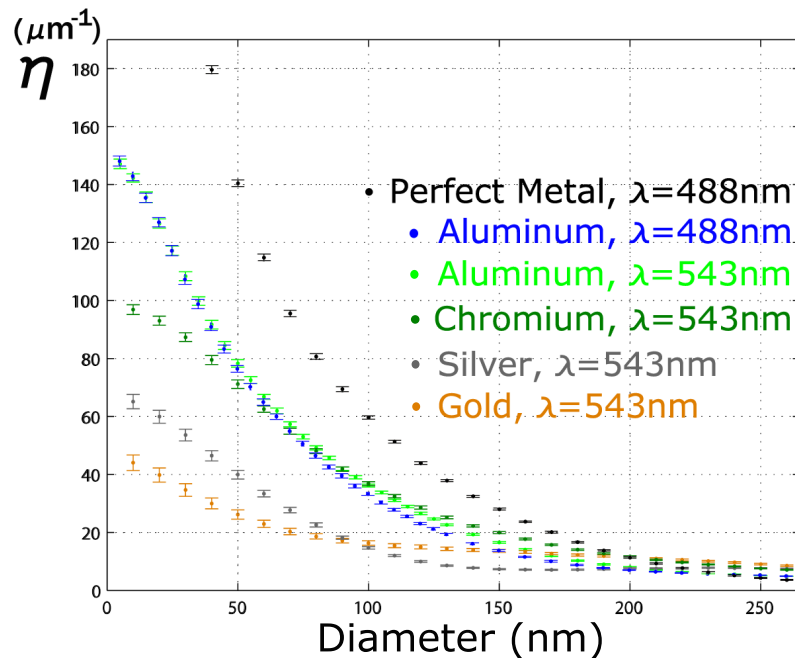


Figure 4.12: Decay constants of various metals simulated as cladding surrounding apertures. Energy density along the central axis of aperture is fit to an exponential decay model,  $I(z) = I_0e^{-\eta z}$ , and exponential decay constant  $\eta$  is plotted here.

**Attenuation Constant for Different Metals** Exponential decay constants for all metals, including the perfect metal, follow a monotonic decreasing trend as

the aperture size increases, with aluminum most resembling the perfect metal. Compared with aluminum, chromium, silver, and gold, are less conductive and attenuate incident light much less in their apertures. Gold, however, shows more attenuation than silver for apertures larger than  $100\text{nm}$ . We think this is due to the incident wavelength being close to plasmonic frequency of gold, and the decay is due to energy transfer to gold, rather than due to geometric effect of the aperture.

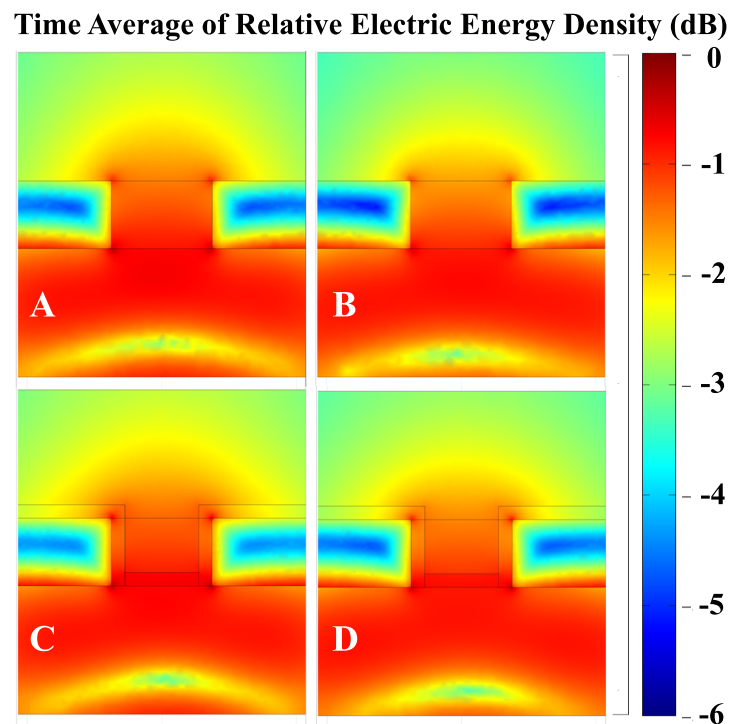


Figure 4.13: Time average of electric energy density inside and outside an aperture of diameter= $150\text{nm}$  in  $100\text{nm}$ -thick aluminum layer, supported by fused silica on one side, and immersed in aqueous solution in another. Light incidents from the fused silica side. Shown in dB scale to include large dynamic range. A.  $\lambda = 488\text{nm}$  without ALD layer; B.  $\lambda = 530\text{nm}$  without ALD layer; C.  $\lambda = 488\text{nm}$  with  $20\text{nm}$   $\text{Al}_2\text{O}_3$  ALD layer; and D.  $\lambda = 530\text{nm}$  with  $20\text{nm}$   $\text{Al}_2\text{O}_3$  ALD layer.

**Dielectric-filled apertures** To compare with experimental results discussed later in this chapter, we also simulated for numerical solutions of electromagnetic waves in aluminum apertures with and without a dielectric layer, specifically, a  $20\text{nm}$  aluminum oxide layer. Fig. 4.13 shows the electric energy density plots. The obvious conclusion to draw is that the left-half of the frame show more energy transmission (and hence inside the aperture), whereas the right half shows smaller energy density. This is expected, because the left panel was simulated using  $488\text{nm}$  light whereas the right panel was simulated using  $530\text{nm}$  light.

The lower half of the figure are solutions assuming a  $20\text{nm}$  ALD layer of  $\text{Al}_2\text{O}_3$ . If we look carefully, we can see slightly higher optical transmission from the apertures with ALD layer, than those without. We postpone discussion of this result until the experimental discussion section later in this chapter.

**Profile of a real ZMW** In fabricating physical ZMW device, we used evaporation and lift-off method. Since evaporated aluminum tends to form a crown or a “mushroom top”-like feature, the aperture after lift-off tends to have a larger opening than the bottom, due to the shadowing effect of the mushroom top.

We incorporated the bigger-opening shape of the actual device in one of our simulations. Specifically, using SEM images (shown in Figure 4.7), we estimated there is a  $0.2$ -radian slope of the ZMW side-wall due to fabrication. Simulation results shown in Fig. 4.14 suggests the optical energy is less confined inside a ZMW with a sloped side-wall, compared to that of a perfectly vertical side-wall. This result is hardly surprising given the wider aperture diameter towards the opening.

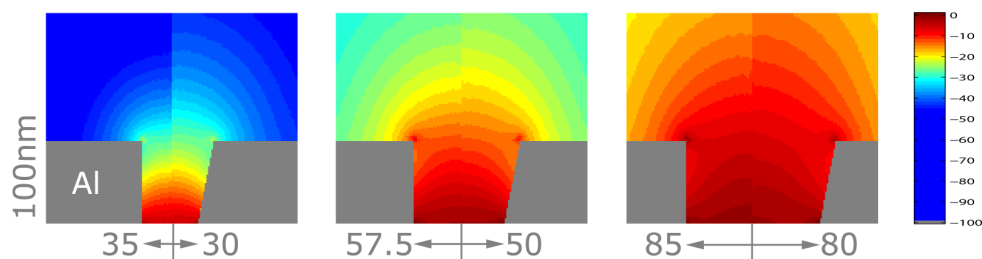


Figure 4.14: Simulated illumination profile inside ZMW with larger opening than entrance. For each plot, the left half represents an aperture with straight side-wall, and the right half represent an aperture with a slanted sidewall. The intensity plots are on the same scale for easy comparison.

On the other hand, the electromagnetic fields of a slanted-sidewall aperture does not differ much from one with straight sidewall. The actual effect is as if the aperture is slightly larger than its strictly cylindrical counter part by approximately 10%. Therefore we ignore this difference in most of our simulations to simplify geometric drawing.

**Consequence to Diffusion Equation** There have been various ways in describing fluorescence correlation function of molecules diffusing inside a metallic aperture. For very small apertures, for example with diameter less than  $60\text{nm}$ , a one-dimensional diffusion model has been successfully applied (49, 84). This model is adequate because of the fast attenuation of electromagnetic energy along the axis of propagation. For diffusion studies of membrane-bound single molecules, a two-dimensional diffusion model is appropriate, especially when the aperture opening is large compared to the depth of the hole (103).

Alternatively, when aperture diameters are in the  $100 \sim 200\text{nm}$  range, the attenuation of electromagnetic energy inside the aperture is not rapid enough

to ignore field variations in the radial direction. Assuming a perfect cylindrical shape, the only direction that a fluorescent molecules moves that does not result in fluorescence fluctuation is the angular direction  $\phi$ . Therefore in fitting fluorescence correlation functions of molecules diffusing in ZMWs, we have successively applied a 2-dimensional diffusion model (105):

$$G^{ZMW}(\tau) = (1 + \frac{F}{1-F} e^{-\tau/\tau_T}) \frac{1}{N_{eff}} \frac{1}{\sqrt{1 + \tau/\tau_{D1}}} \frac{1}{\sqrt{1 + \tau/\tau_{D2}}}, \quad (4.16)$$

where  $F$  is fraction of molecules in triplet state with characteristic time  $\tau_T$ ,  $N_{eff}$  is the number of molecules in the observation volume,  $\tau_{D1}$  and  $\tau_{D2}$  are two characteristic times for  $\hat{z}$  and  $\hat{r}$  directions, respectively. We have found it provide the best fit for single fluorescent molecule diffusion in our ZMW devices, compared to 1- or 3- dimensional diffusion models.

## 4.7 Experimental Materials and Methods

We present two experiments in better our understanding of ZMW's optical properties. First is wavelength-dependent transmission properties for different hole sizes, measured using narrow band tunable filter. Second is illumination profile inside ZMWs, measured using successive dielectric-filling of the apertures to elevate fluorescent solution away from the aperture entrance.

### 4.7.1 Tunable Filter for Measuring Transmission

**Transmitted Spectrum Measurement** Since each ZMW only let very little transmitted light through, measuring the transmitted spectra presents challenges. Previously, Huizhong Xu had attempted to measure discrete spectra

using three filters at red, green and blue. However the relatively low sensitivity of EMCCD camera did not yield great results. In our study, Avalanche photodiode (APD) with much higher sensitivity, was used to collect transmitted light. To obtain the complete spectrum, three tunable optical filters (Semrock, Rochester, NY) were used to cover the complete visible range. Each filter position covers approximately 50nm bandwidth, and is tunable by adjusting the light incidence angle.

As shown in Fig. 4.15, the incidence angle was changed by turning the *Versa Chrome* series tunable filters from Semrock (Rochester, NY) inside a custom-machined holder at constant speed. A Hall-effect sensor detects the 90-degree incidence angle and a pulse is sent to gate the APD output, such that photon count momentarily reads zero. This zero-reading is used to mark the starting point of a rotation, and incidence angles are interpolated for every degree between successive zero-reading marks, and mapped to filter pass band according to table 4.1.

#### **4.7.2 Aluminum Oxide Filling by Atomic Layer Deposition**

We use atomic layer deposition tool (Oxford ALD FlexAL, Oxfordshire, UK) to deposit thin layers of dielectric material into the ZMWs. Prior to ALD process, ZMW devices were diced, resist pillars lifted off, and cleaned in Glen1000 oxygen plasma etcher (Yield Engineering Systems, Livermore, CA) for 5 minutes at 400W continuous RF power.

For each ALD process, we used 300°C thermal Al<sub>2</sub>O<sub>3</sub> recipe, and repeated the deposition cycle by desired number of times. We used geometrically increasing

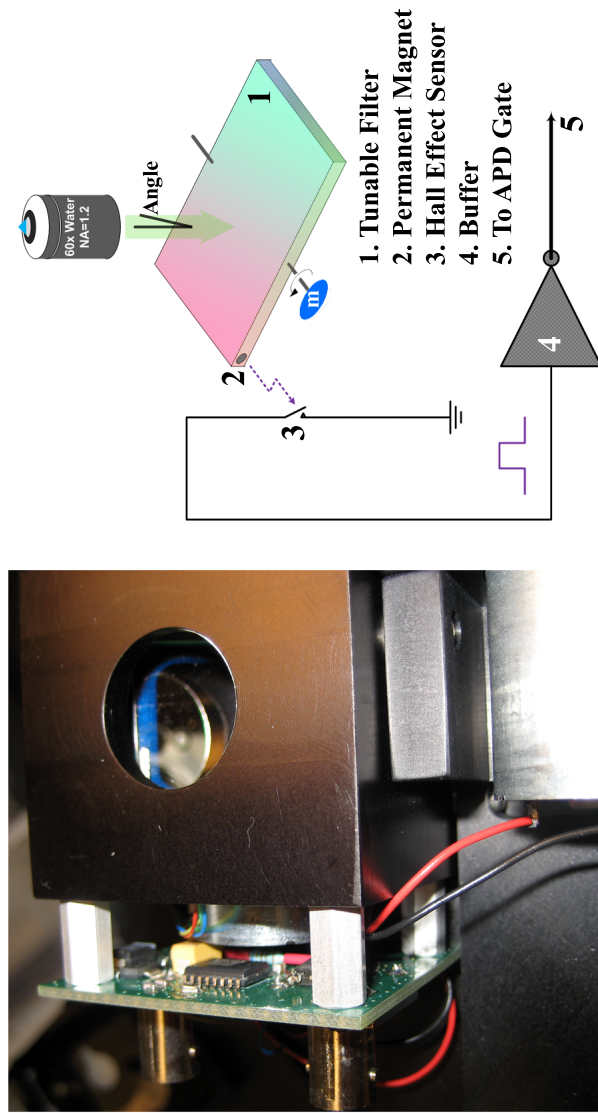


Figure 4.15: Tunable Filter setup. The angle of the filter determines the pass band. As the motor (m) drives the filter through one rotation, the permanent magnet (2) triggers the hall effect sensor (3), generating a short pulse. Buffered output (5) momentarily nulls APD output. The zero-photon count region in photon intensity data stream indicates filter position (Angle =  $-90^\circ$ ).

Table 4.1: *Versa Chrome* filter series center wavelength and pass band width, extracted from simulation results provided by Semrock.

| Filter | TBP01-490/15-25x36 |         | TBP01-550/15-25x36 |         | TBP01-620/14-25x36 |         |
|--------|--------------------|---------|--------------------|---------|--------------------|---------|
|        | $\lambda_c$ (nm)   | BW (nm) | $\lambda_c$ (nm)   | BW (nm) | $\lambda_c$ (nm)   | BW (nm) |
| 0      | 490.0              | 19.6    | 549.9              | 19.4    | 620.0              | 19.2    |
| 10     | 487.6              | 19.6    | 547.3              | 19.4    | 617.2              | 19.2    |
| 20     | 480.8              | 19.2    | 540.3              | 19.0    | 609.1              | 19.4    |
| 30     | 470.4              | 18.8    | 529.4              | 18.8    | 596.5              | 19.0    |
| 40     | 457.3              | 18.6    | 515.6              | 18.8    | 580.6              | 18.8    |
| 50     | 443.1              | 19.0    | 500.7              | 19.0    | 563.3              | 19.0    |
| 60     | 429.3              | 19.4    | 486.6              | 19.6    | 547.1              | 19.4    |

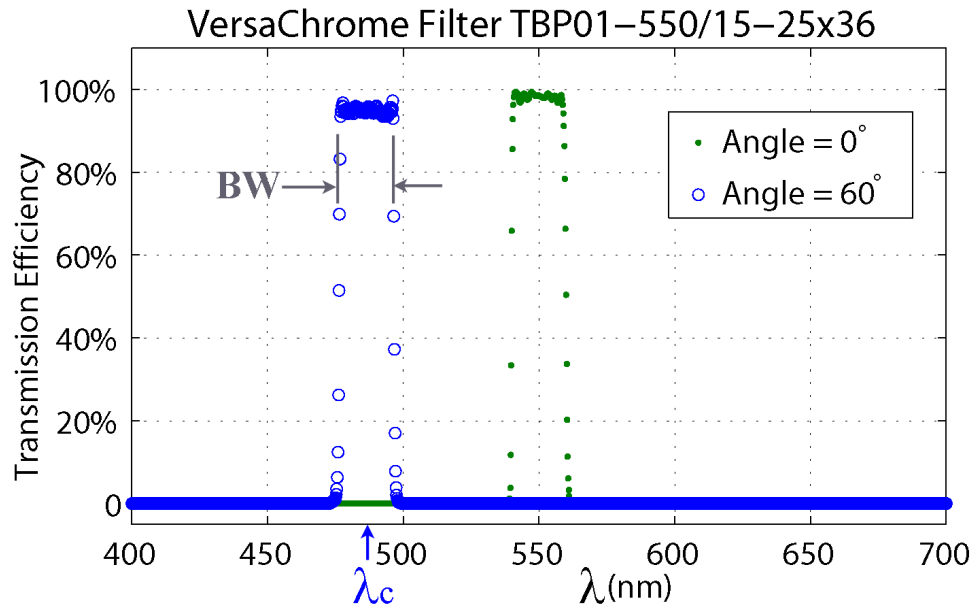


Figure 4.16: Sample *Versa Chrome* Transmission characteristic at 0° and 60°, two edges of the usable range.

number of cycles between successive devices, because we expect exponential effect of the filled dielectric.

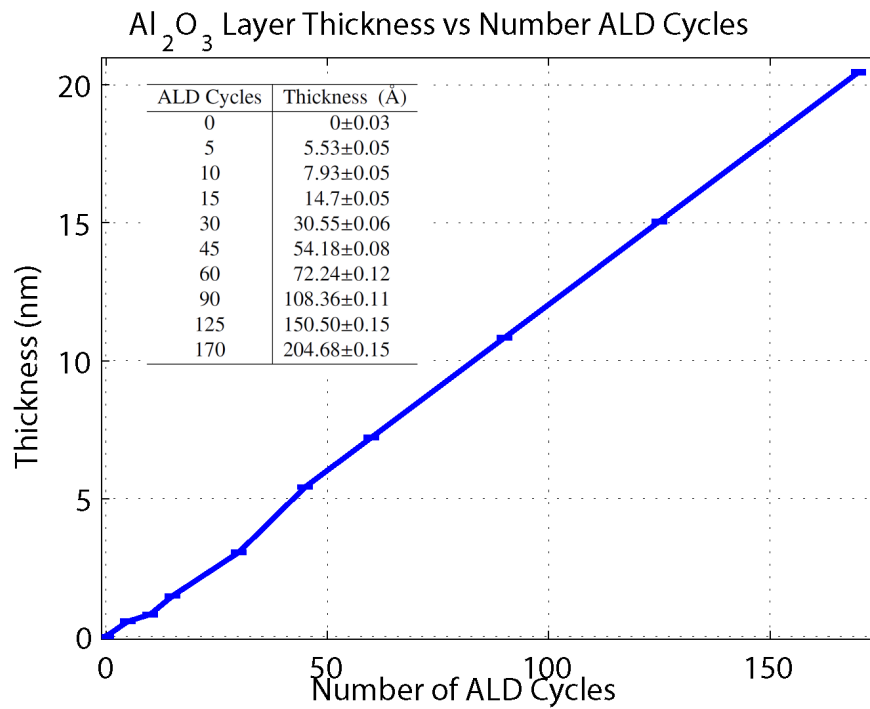


Figure 4.17: Linear relationship between deposited  $\text{Al}_2\text{O}_3$  and the number of ALD cycles.

We measure the thickness of deposited aluminum oxide using ellipsometry. All devices were measured prior to ALD process, and data analyzed to extract the native aluminum oxide thickness, which is  $29.98 \pm 0.01 \text{Å}$ . Refractive indices of native aluminum oxide are extracted for wavelengths between 300 and 1000nm, and shown in Fig. 4.18

As with native oxide, the deposited aluminum oxide's refractive indices are also extracted for the wavelengths between 300 and 1000nm. The fitting of refractive indices and oxide layer's thicknesses from ellipsometry measurement is iterative. With extremely thin deposited layers, either a small thickness value or

a low refractive index could account for the relatively small shift in ellipsometry measurement data compared to that without ALD deposition. We hypothesize that the ellipsometry measurement of thickest ALD layer should provide the least uncertainty in refractive index. Therefore we first fit the data from the device with the longest ALD deposition cycle, and extracted the ALD layer's thickness and refractive indices. We then smoothed the average extracted refractive index using a Cauchy model. Finally this smoothed refractive index curve, shown in Fig. 4.18, was plugged back into the ellipsometry fitting routine in order to obtain all the other ALD layer thickness values, shown in Fig. 4.17.

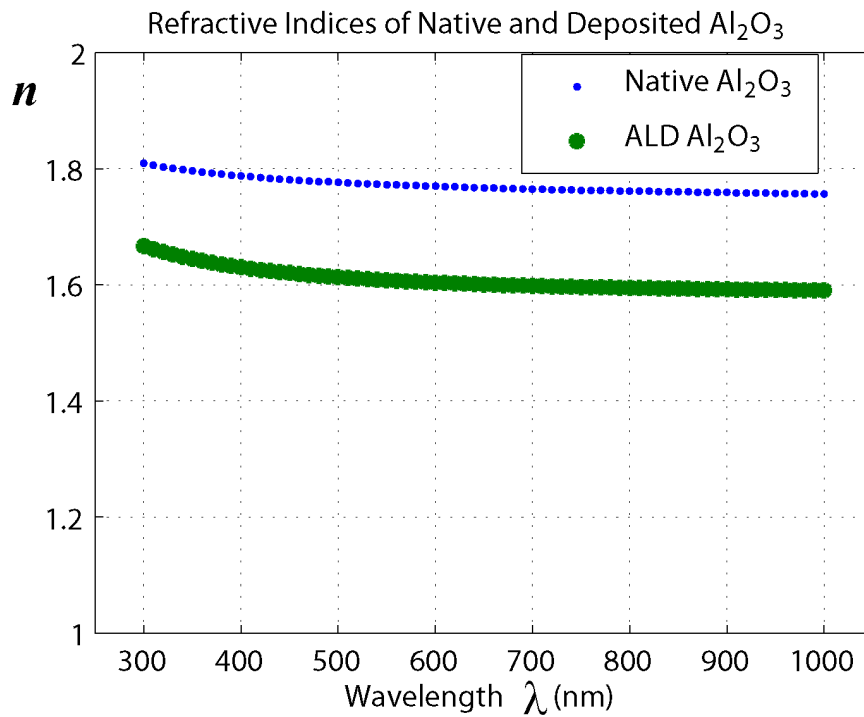


Figure 4.18: Measured refractive indices of native aluminum oxide and ALD deposited  $\text{Al}_2\text{O}_3$ , smoothed to a Cauchy model  $n = 1.583 + \frac{7551}{\lambda^2} + \frac{0.8474}{\lambda^4}$

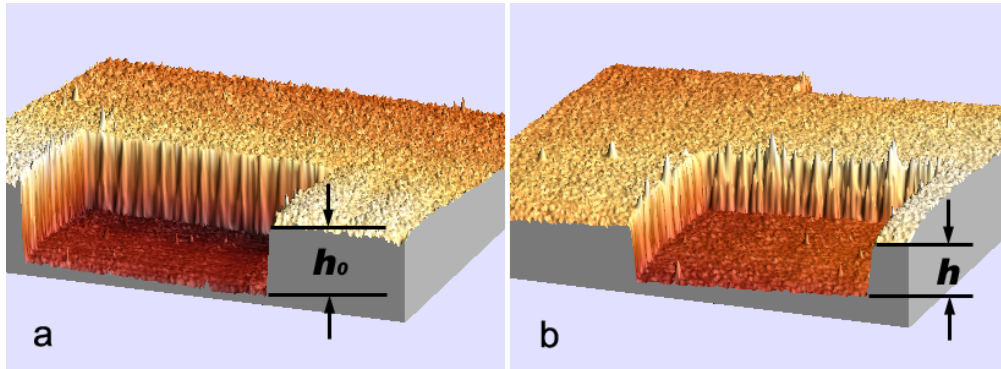


Figure 4.19: Reconstructed 3-D representations of AFM measurement of device profile showing a, height difference  $h_0$  between top aluminum and fused silica substrate surfaces without ALD deposition and, b, height difference  $h$  with 320 cycles of ALD deposition resulting in  $39\text{nm}$   $\text{Al}_2\text{O}_3$ . Both  $h_0$  and  $h$  are found to be approximately  $120\text{nm}$ , indicating uniform ALD deposition on both fused silica and aluminum surfaces

**ALD coats inside and bottom of ZMWs** Ellipsometry only measured the ALD thickness on the flat surface of aluminum, but not that inside the ZMW apertures. Since the ZMW wall consists of aluminum, and bottom consists of fused silica, we need to verify that the deposited dielectric material uniformly coats both fused silica and aluminum in order to be certain that ALD layer is deposited on the bottom of the ZMWs. We used atomic force microscopy to profile a  $5\mu\text{m}$ -square opening on the aluminum surface that exposed the underlying fused silica substrate. As shown in Fig. 4.19, without ALD deposited  $\text{Al}_2\text{O}_3$ , the height difference  $h_0$  between fused silica and aluminum surfaces, i.e, the aluminum layer thickness, is  $120.35 \pm 1.74\text{nm}$ , whereas with ALD deposition, this height difference  $h$  is  $120.21 \pm 2.40\text{nm}$ , indicating that ALD deposition indeed coats both fused silica and aluminum (with native oxide) surfaces without preference. Therefore we conclude ellipsometry measurements of deposited  $\text{Al}_2\text{O}_3$  on aluminum surface also reflect the thickness of that deposited inside the ZMW apertures.

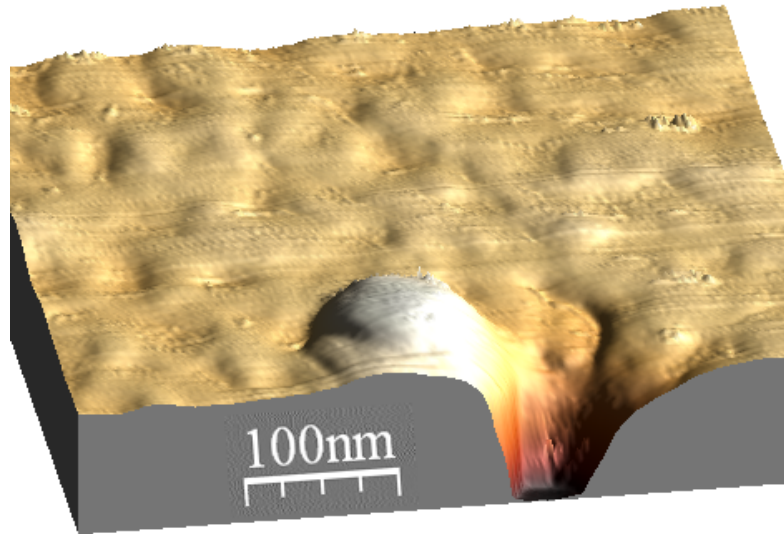


Figure 4.20: Reconstructed 3-D representations of AFM measurement of one ZMW coated with ALD film. The dip in the surface indicates where the ZMW used to be, and is only partially filled with the deposited film. The small lump next to the opening of the dip was most likely due to deposited aluminum that did not completely lift off during the ZMW fabrication process.

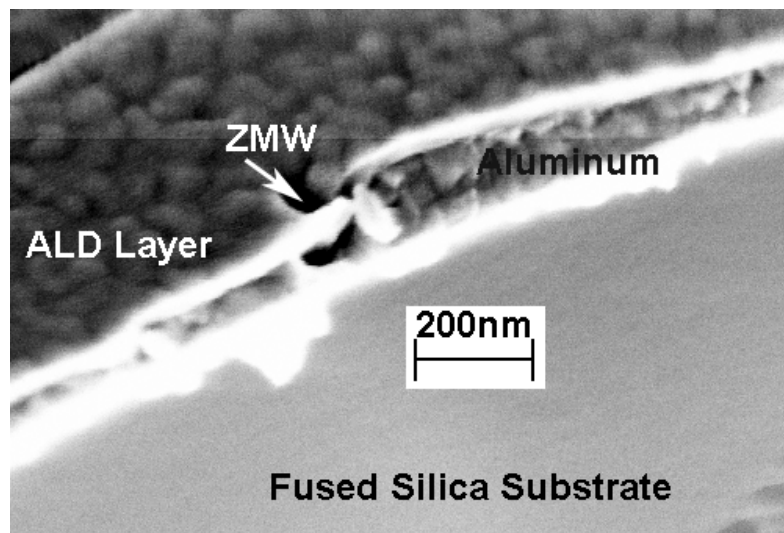


Figure 4.21: Scanning Electron Microscope image of a ZMW with a thin layer of ALD film cover. The ALD film is seen to have conformally coated the ZMW aperture.

At the same time, the ALD film does not cover the openings of the apertures in aluminum. As we can see in Fig. 4.20 and 4.21, the ALD film coats both the topside aluminum and conformally coats the inside walls of the ZMWs, confirming the ALD coated model shown in Figure 4.22.

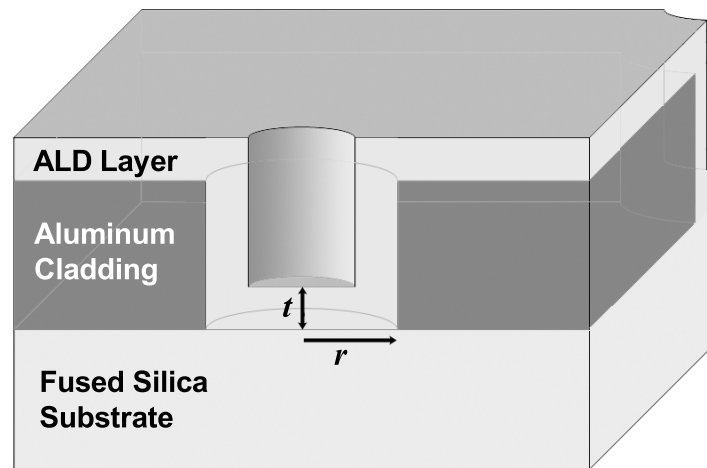


Figure 4.22: Drawing of ZMW with ALD layer. Deposited ALD thickness  $t$  conformally coats the inside of ZMWs and shrinks the effective volume of the aperture.

This is an idealized model of ALD coating the aperture. Certainly in reality we expect the deposition to be non-uniform, and perhaps filling up corners a lot faster than surfaces or walls. Indeed the openings of very small apertures tend to be pinched off with large number of ALD cycles, resulting in lack of fluorescence reading when dye-labeled molecule solution is introduced, indicating non-accessible volume. However when we deposit less than  $20nm$   $Al_2O_3$ , the deposited layer thickness is much less than that of the ZMW dimension, which is on the order of  $100nm$  in diameter, and we assume this idealized model to be approximately true, and reasonably fit for numerical simulations.

## 4.8 Results and Discussion

### 4.8.1 Transmission Properties

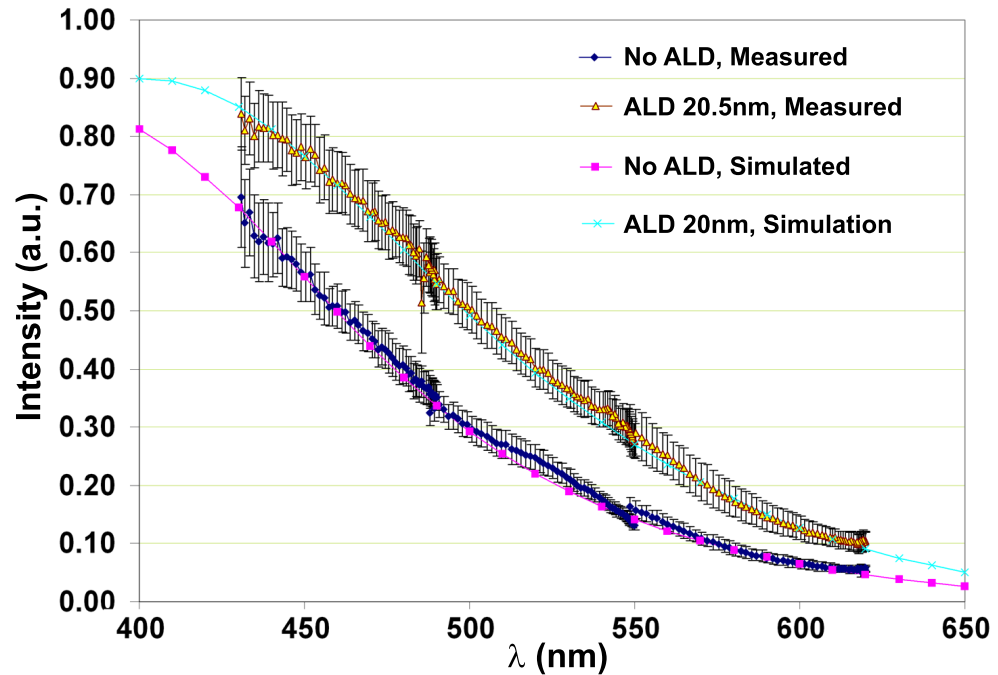


Figure 4.23: Compare measured and simulation results of transmitted light through  $156.2 \pm 2.1nm$  aperture in aluminum layer, with and without 20nm  $Al_2O_3$  ALD layer.

We measured transmitted spectra of  $156.2 \pm 2.1nm$  apertures, with and without 20nm ALD  $Al_2O_3$  layer. Raw photon counts of every incident angle of an aperture is divided by raw photon counts of a large opening at the same incident angle on the device, normalizing out other optical elements' effects in the optical path, resulting in spectral property of the aperture alone. Since the large opening on the device passes orders of magnitude more light than a sub-wavelength aperture, a neutral density filter was used in order to protect APD from saturation. Proper scaling parameters were used to match the three sec-

tions of results of three filter bands. Data over 9 holes of the same size were averaged to give good statistical distribution and minimize uncertainty from hole-to-hole variations.

In collecting simulation results, a mesh grid of a circular region is set up over the aperture opening, forming roughly a 129-degree dome simulating  $1.2\times$  numerical aperture of the  $60\times$  objective lens used in photon sampling. Transmitted intensity is the integrated time-average energy density of this region.

There are several basic observations we can make from the plot in Fig. 4.23. First of all, longer wavelength is more attenuated. We can approximately fit a wavelength-dependent exponential decay constant. However, the data does not fit well to a simple exponential decay function, nor does it fit to an exponential decay function with decay constant in the form of  $-b\sqrt{1/\lambda_c - 1/\lambda}$  (84). This is because first of all, the ZMW aperture is neither an infinitely long cylindrical waveguide, nor an aperture on an infinitesimally thin perfect metallic slab. Secondly, there is not a definite cut-off wavelength, due to the finite conductivity of real metal. Therefore there is always loss as light transit through the apertures.

This leads to our second observation, that aperture with 20nm ALD dielectric allows more light through, and has a seemingly longer cut-off wavelength than the aperture without ALD layer. This behavior agrees with prediction of Eq. 4.15 that  $\lambda_c$  increases when there is dielectric material  $\epsilon_r > 1$  that fills the waveguide. Although our theoretical derivation was based on an infinitely long waveguide in cylindrical coordinates, nonetheless, dielectric filling effectively “shortens” the wavelength of light, and can satisfy the same geometry’s boundary condition with a lower frequency light compared to a vacuum-filled aperture.

## 4.8.2 Illumination Profile Inside Apertures

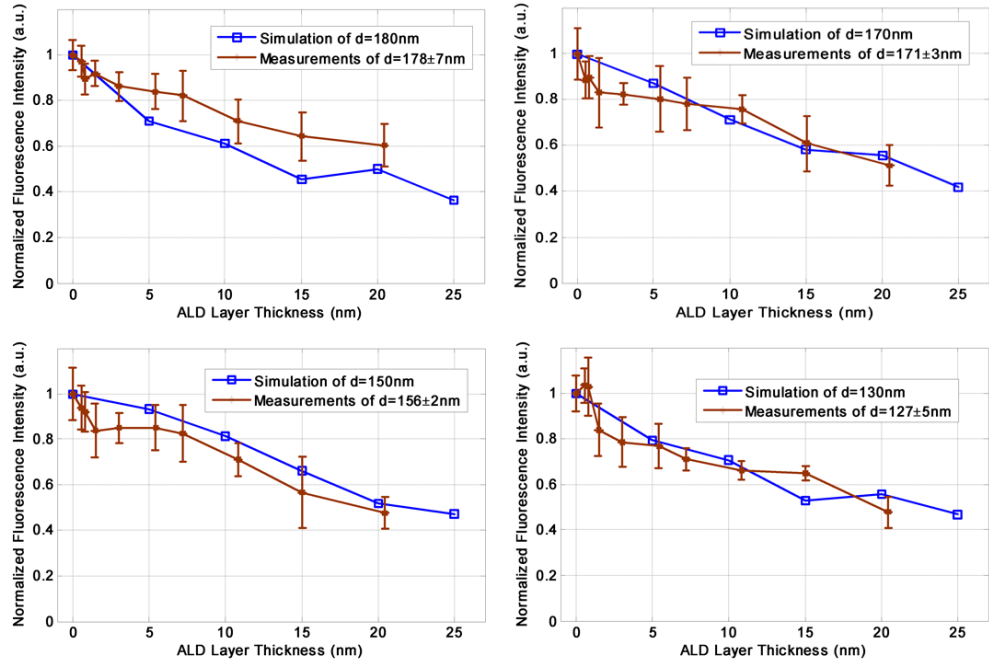


Figure 4.24: Comparing measured and simulated fluorescence intensity for apertures of two diameters, with and without ALD deposited aluminum.

Fluorescence intensity data were taken with 488nm laser illumination and collected in a confocal set up, detecting photons in the emission band of Alexa488 dyes.  $1\mu\text{M}$  dUTP-Alexa488 (Molecular Probes, Carlsbad, CA) in  $1\times$  PBS solution was used as imaging probes to report illumination intensity inside the apertures. Since the illumination intensity inside a ZMW is assumed to follow an exponential decay profile, that is,

$$I(z) \sim I(0)e^{-\eta z} \quad (4.17)$$

exciting fluorescent molecules in volume  $dv$  with concentration  $C$ , the total emitted photon intensity from volume  $dv$  at depth  $z$  is

$$dI_m(z) \sim I(0)e^{-\eta z} dv. \quad (4.18)$$

By reciprocity (8, 45), the efficiency of fluorescence emission coupling out of aperture is the same as excitation light going in. Therefore the fluorescence intensity at detector is

$$dI_d(z) \sim I(0)e^{-2\eta z} dv. \quad (4.19)$$

Here we have assumed the attenuation constant  $\eta$  is the same for both the excitation and emission wavelengths of the fluorophore, which in reality is not the case. However based on our simulation, see Fig. 4.12, the attenuation constants at these two wavelengths do not differ drastically. The model we have assumed here will result in an average value of the two, i.e,  $2\eta = \eta_{\text{ex}} + \eta_{\text{em}}$ .

Using the ALD-filled ZMW model shown in 4.22, the total fluorescence intensity collected from an aperture is:

$$I_d \sim \int_{r=0}^{a-t} \int_{z=t}^{\infty} I(0)e^{-2\eta z} 2\pi r dz dr \quad (4.20)$$

$$\sim \pi(a-t)^2 I(0)e^{-2\eta t} \quad (4.21)$$

where  $t$  is the thickness of ALD layer, elevating fluorescent solution away from aperture entrance,  $a$  is the radius of the aperture.

Table 4.2: Fitting result of exponential decay constant  $\eta$  used in equation 4.21.

| Diameter (nm) | Simulation ( $nm^{-1}$ ) | Experiment ( $nm^{-1}$ ) |
|---------------|--------------------------|--------------------------|
| 178±7         | 9.7±5.8                  | 2.0±2.6                  |
| 171±3         | 3.2±1.9                  | 3.9±4.5                  |
| 156±2         | 2.9e-6±2.6               | 3.4±3.4                  |
| 127±5         | 3.9e-6±4.8               | 1.0±5.0                  |

Clearly, other than the result of the  $180\text{nm}$ -diameter aperture, the measured exponential decay constants are smaller than what we had expected using Fig. 4.12. Although we had expected an attenuation constant close to  $10\text{nm}^{-1}$ , the fitting data of fluorescence in ALD-deposited apertures suggest a decay constant between 2 and 3 times less. We attribute this disagreement to the fact that ALD layer enhances both the energy traveling through the aperture, and the energy coupled into the aperture. According to Fig. 4.23, the ratio of energy coupled into ALD deposited apertures to no ALD deposited apertures is around 2. Therefore as the ALD layer lifts fluorescent solution away from the aperture opening and away from the most intense optical energy, it also passes more light into the aperture. The exponential decay of optical energy is greater than the enhanced transmission due to ALD dielectric filling, resulting in a combined effect of lower excitation energy with increasing ALD layer thickness, but still greater fluorescence than predicted by a simple exponential decay model. Therefore the model assumed by Eq. 4.21 is invalid for our ALD measurement and simulation, and should be adjusted to reflect higher transmission with deposited dielectric filling.

## 4.9 Conclusion

We demonstrated highly sensitive measurement method and analyzed illumination profile inside sub-wavelength aluminum apertures. We showed agreement between measurement results and numerical solutions obtained using finite element methods. The basic assumption that optical energy decreases exponentially inside a metallic aperture is shown to be valid. At the same time, dielectric-filling inside metallic apertures enhances transmission.

## **Chapter 5**

### **GFP Aptamer Binding to GFP**

## 5.1 Introduction

As a demonstration of signal processing techniques discussed so far, we study the effect of a short ribo-nucleotide, or an aptamer, on the fluorescence of Green Fluorescent Protein (GFP). To investigate the fluorescence behavior on a single-molecule basis, we use ZMWs to minimize background fluorescence, while keeping fewer than one molecule inside the observation aperture. In processing photon data collected through ZMW observation, we used matched filtering to clean up noise in the frequency domain, and maximize the signal to noise ratio in order to identify single molecule events, from which a correct photon count histogram can be obtained. In addition, we used fluorescence correlation spectroscopy to analyze the interaction between GFP and a dye-labeled aptamer. With careful selection of fluorescent molecules, we did not have to utilize spectral deconvolution techniques to separate fluorescence from GFP and dye-labels. We find that upon aptamer binding, a GFP molecule may be in a dark ( $\sim 43\%$  of the time) or a fluorescent ( $\sim 57\%$ ) state. However, even in the fluorescent state, an aptamer-bound GFP molecule is on average only 45% as fluorescent as a free GFP molecule. This result agrees with bulk measurement where GFP solution saturated with aptamer is only 25% as fluorescent as a similar solution without the aptamer.

## 5.2 Background

**Green Fluorescent Protein** Green fluorescent protein (GFP) was first discovered in 1962 by Shimomura *et al* (88). The wild type GFP has two absorption peaks, at approximately  $396\text{nm}$  and  $473\text{nm}$ , with a higher extinction coefficient

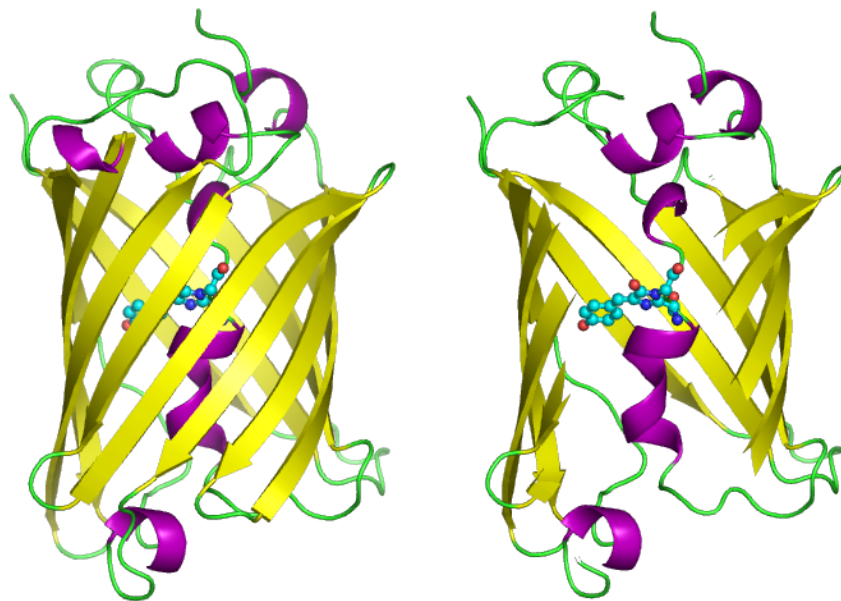


Figure 5.1: Tertiary structure of Green Fluorescent Protein (GFP) showing beta barrel and its caged fluorophore. Image from the RCSB PDB ([www.pdb.org](http://www.pdb.org)) of PDB ID 1GFL (109).

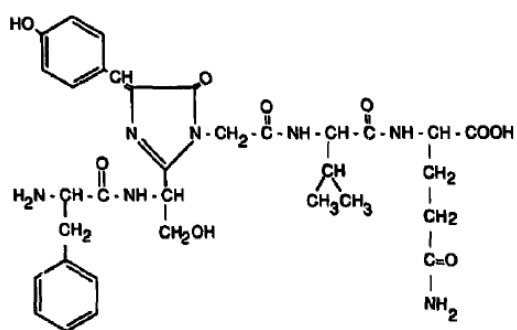


Figure 5.2: Chemical structure of GFP fluorophore. (78)

at the shorter wavelength, and one emission peak at 504nm (76). However, there are many variants derived from wild type GFP that absorb and emit at slightly shifted wavelengths, and with different extinction coefficients and quantum yields. One of the most popular phenolate anion mutants, the enhanced GFP or eGFP, is used in our current study. Its excitation wavelength peak is at 488nm and its emission peak is at 509nm (76,102). Compared to other dyes, eGFP has the advantage of a high extinction coefficient ( $\epsilon \sim 5M^{-1}\mu m^{-1}$ ) and quantum yield ( $\sim 0.6$ ) and can be naturally expressed by organisms upon successful transfection. It has also been reported that a single GFP molecule has on and off blinking characteristics that go dark after prolonged illumination at its excitation wavelength. This dark state, however, is reversible when the molecule is radiated with shorter wavelength (360 ~ 405nm) light (18). Though GFP was originally found in *Aequorea* jellyfish, the cloning (78) and expression of its genes were later demonstrated in other organisms, and proven to be a useful marker of gene expression, molecular kinetics, and cell signaling (9, 30). Its utility rests in that GFP is a relatively small molecule. At 27kDa and only 238 amino acid residues, it provides stable fluorescence by encaging its fluorochrome safely within its beta-barrel structure (Fig. 5.1). When GFP is used in tagging applications, its fluorescence intensity and location is a direct reflection of gene expression or subcellular localization of GFP-fused proteins. In a recent application, Moran-Mirabal *et al* studied cell investigation into nano-sized apertures using cells expressing actin fused with GFP (64). GFP's fluorescence can be altered by its local environment, either chemically, or by ligand-substrate interactions, making it suitable as a physiological reaction indicator. Indeed, the current study is on an aptamer's effect upon binding to GFP, and its potential application as a cellular activity indicator by controlling fluorescence intensity via association

and dissociation of a GFP aptamer to GFP.

For simplicity, in the rest of this discussion, “GFP” refers to the eGFP variant in our study, unless otherwise noted.

**GFP-Aptamer** Aptamers are short DNA or RNA oligos with relatively simple structures and certain physiological attributes. A vast pool can be created with enormous diversity from simple sequence alterations. Oligos with desired functionality can be selected from the pool via systematic evolution by exponential enrichment or SELEX (96).

The GFP aptamer under study is an 82-nucleotide RNA oligo that has been identified using this method. The initial GFP aptamer was selected from a 50-randomized nucleotide RNA pool with  $10^{14} - 10^{16}$  unique molecules. His-tagged GFP bound to nickel-charged beads and nitrocellulose membrane-bound GFP were used alternately in RNA molecule selection steps, with negative selections for nickel-charged beads and nitrocellulose-membrane, resulting in multiple copies of two highly related families of RNA oligos after 15 rounds of binding and amplification. It was found that these two families both had sub-micromolar affinity towards GFP, and they were homologous. It was also found that deleting either the 5' or the 3' primer regions caused one of the RNA families to lose activity, indicating the need for some extended nucleotide link for the oligos to maintain their secondary structures. A new RNA pool was created based on this result, each molecule with the core 36-nt binding sequence shared by the two families, and flanked by a 45-nt and 40-nt random regions on 5' and 3' ends, respectively, plus the constant PCR primers, leading to a new  $10^{14} - 10^{16}$  RNA pool. Further 12-rounds of SELEX process on this new library resulted in

one clone, designated as AP3, and identified to have the highest affinity towards GFP ( $K_D = 14.4nM$ ) and fluorescence quenching efficacy ( $\sim 70\%$ ) (89).

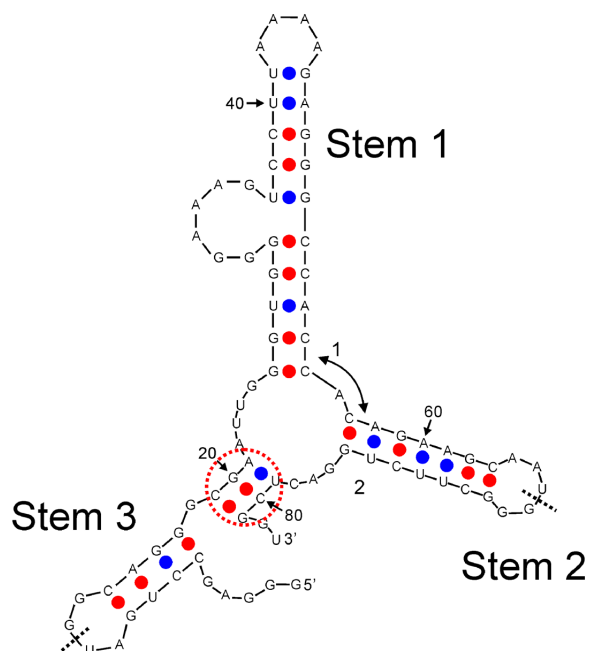


Figure 5.3: Secondary structure of GFP aptamer AP3 (89).

## 5.3 Fluorescence Reduction of GFP in Bulk Measurement

### 5.3.1 Materials and Methods

**GFP-Aptamer** The 82-nucleotide RNA peptide AP3 is not fluorescent on its own. Fluorescent versions of AP3 were produced using dye-labeled primers to initiate transcription. However, the labeling efficiency is only estimated to be between 20% and 50%. Cy-3 labeled aptamers were used for bulk measurements, both in solution and in surface-immobilized GFP using  $Ni^{2+}$ . Dy-647

labels were used for single-molecule fluorescence correlation studies described later in this chapter. Compared with the Cy-3 label, Dy-647 is spectrally further separated from that of GFP, and hence easily distinguishable using appropriate emission filters. In labeled aptamer solutions, there were un-incorporated dyes and dye-labeled free primers, as well as short segments of RNA degradation products. A gel-purification step was used to remove these smaller molecules for single-molecule experiments. For storage, the aptamer is kept in a concentrated aliquot with Tris·HCl at pH 8.0, and SUPERase·In RNase Inhibitor from Ambion, Inc (Austin, TX), and stored at  $-25\text{ }^{\circ}\text{C}$ .

**Optical Set Up** An inverted IX-71 microscope (Olympus USA, Central Valley, PA) was used for epi-fluorescence measurements. Excitation light comes from an EXFO arc lamp (Mississauga, Ontario, CANADA). Two fluorescent filter sets from Chroma Technology (Bellows Falls, VT), one for GFP and another for Cy3/DiI were used to image GFP and Cy-3 labeled aptamers respectively. Fluorescence images were acquired through a 20 $\times$  microscope objective and collected by an EMCCD camera.

**Binding Buffer** GFP aptamer binding to GFP was detected in binding buffer with 0.5% BSA, 1xPBS and 5mM MgCl<sub>2</sub> at pH 7.4.

### 5.3.2 In Solution

Two images were taken of GFP solutions, as seen in Fig. 5.4. With 1 $\mu\text{M}$  GFP in PBS, we see the detected fluorescence intensity is much greater than the same

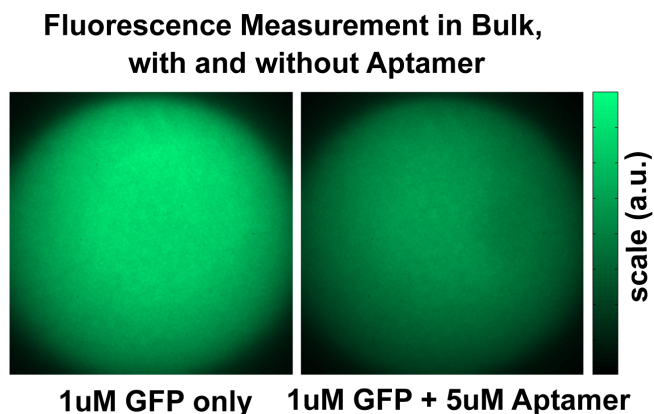


Figure 5.4: GFP fluorescence in solution with and without Aptamer.

GFP solution with  $5\mu M$  (unlabeled) aptamer. If we assume  $K_D = 14nM$ , more than 99% of GFP molecules should be bound by an aptamer. Although the exact fluorescence intensity decrease after adding aptamer depends on scaling and proper background correction, the approximate reduction of fluorescence is indeed 70%, agreeing with previous results (89). However this experiment does not clearly explain what aptamer binding does to GFP.

### 5.3.3 Cy3 labeled Aptamer Binding to GFP Immobilized on Glass Surface

Since the GFPs were expressed with a sequence of six histidines at their C-terminus, and this  $(His)_6$  group (or His-tag) binds strongly to divalent metallic ions such as  $Cu^{2+}$  and  $Ni^{2+}$  (81),  $Ni^{2+}$ -coated surfaces can be used to immobilize GFPs with His-tag.  $0.1\mu L$  of  $200mM$   $NiCl_2$  dissolved in water was dropped on a clean microscope slide and allowed to dry on a  $70^\circ C$  hot plate.  $500nM$  His-tagged GFP in PBS buffer was dropped on the slide and allowed to incubate for

### GFP fixed to glass surface, before and after adding Aptamer

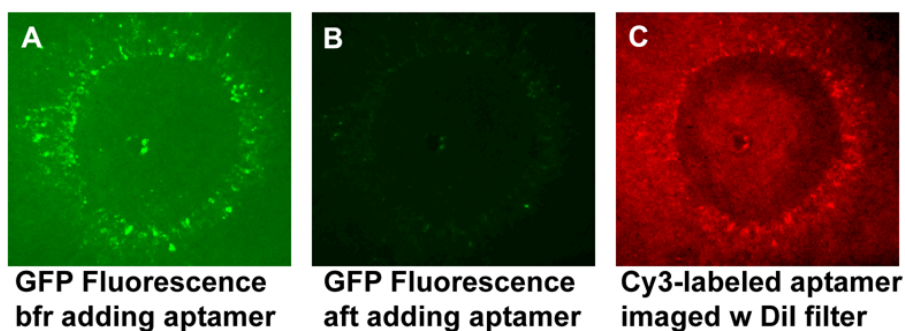


Figure 5.5: Fluorescence of GFP molecules fixed on surface via  $\text{Ni}^{2+}$  binding, before and after adding Aptamer solution.

30 minutes. The slide is then rinsed with deionized water, and imaged with pure PBS buffer, used to keep the slide hydrated.  $100\text{nM}$  Cy3-labeled GFP-Aptamer solution was subsequently applied to the same surface, allowed to incubate for half an hour at room temperature, before being washed off with de-ionized water and imaged.

With dried  $\text{Ni}^{2+}$  grafted on the surface, we can clearly see His-tagged GFP adsorption by the increase in fluorescence in the  $515\sim 560\text{nm}$  band (Fig. 5.5.A). But there was undetectable fluorescence in the  $605\text{nm}$  (Rhodamine/Cy-3/DiI filter, Chroma Technology) band, before Cy-3 labeled aptamer solution was added (not shown). After the  $5\mu\text{M}$  aptamer solution was incubated, there was a marked reduction in GFP fluorescence (Fig. 5.5.B) and increased Cy-3 fluorescence, indicating adsorption of Cy-3 labeled aptamers (Fig. 5.5.C), co-localized where GFP protein had adsorbed. Control experiments using Cy-3 labeled aptamer solution, incubated on a  $\text{Ni}^{2+}$  grafted surface did not result in specific adsorption to the surface (not shown), indicating targeted aptamer binding to GFP molecules only.

### 5.3.4 Whether Aptamer completely quenches GFP

From bulk-fluorescence measurements, we see that when aptamer is mixed with GFP in solution, the overall fluorescence of the GFP solution decreases by roughly 70%. It is uncertain, however, if aptamer binding to a single GFP results in complete quenching of GFP fluorescence, or if 30% of GFP remain, however transiently, unbound and fluorescent at normal levels. In order to tell how aptamer affects GFP fluorescence on a single-molecule level, the straight-forward method is to continuously monitor a single GFP molecule's fluorescence, add aptamer molecules, detect binding, and observe the GFP molecule again detecting its fluorescence change.

This method is met with several difficulties. First of all, in order to focus observation on a single GFP molecule, it is necessary to either track the molecule as it diffuses through solution, or stationarily observe a fixed molecule. Although His-tagged GFP molecules can be immobilized on Ni<sup>2+</sup> grafted surfaces, and observation can be focused on a few fluorescent spots on said surface, impurities can confuse our measurements, GFP can float off half way through experiments, or GFP can go into blink mode where it will temporarily become non-fluorescent (18). Therefore we may lose a GFP molecule under observation simply due to prolonged exposure at its excitation wavelength. This blinking behavior may also be confused with fluorescence quenching after GFP-Aptamer is incubated on a surface. Lastly, if aptamers completely quench GFP's fluorescence, we will not be able to image any surface features. In short, observing a fixed GFP molecule's fluorescence and the effect of GFP aptamer has to overcome uncertainties in location, fluorescence baseline, photo bleaching and blinking characteristics that are beyond the experimenter's control, or at best,

requires observations of many molecules in order to build a statistical distribution of GFP fluorescence before and after aptamer binding.

## 5.4 Single-Molecule Measurements

To understand the aptamer binding effect on GFP, it is important that we isolate each individual molecule and study the fluorescence one molecule at a time.

Two methods allow us to observe GFP in free solution and on a single molecule basis: nanofluidic channel, and confocal microscopy using zero-mode-waveguides. In fact both techniques use a confocal set up. In nanofluidic channels, molecules are driven through a laser focal volume using electrophoresis. Due to the fluidic channel geometry, the concentration needed in order to keep on average one molecule in the focal spot and still have good flow characteristics, is on the order of  $100\text{pM}$ . This is at least two orders of magnitude smaller than the currently known  $K_D$  between GFP and AP3. In addition, magnesium ions in the aptamer solution tend to severely limit the flow rate under electrophoresis. Therefore when we ran GFP and aptamer mixture in the nanofluidic channels, we did not see bound molecules. Hence this experimental result is at best inconclusive. For completeness, additional information on this experiment is included in appendix 5.6.3.

**Zero-Mode-Waveguides** Zero-Mode Waveguides provide a reaction and observation volume that is on the order of zeptoliters, allowing single molecule observation while keeping the ligand concentration up to micro-molar range. In our case, we test GFP and aptamer binding with ligand concentrations at less

than  $1\mu M$ , which is relatively low compared to what is permissible by ZMW, but much higher than what can be achieved with diffraction-limited illumination.

We attempted two methods using ZMWs. First, in subsection 5.4.1, we immobilized GFP molecules inside ZMWs, and applied a Cy-3 labeled aptamer solution. We did not resolve a fluorescence change upon binding. However from photo bleaching experiments, we did determine  $k_{\text{off}}$  is very low, hence unbinding of AP3 from GFP is infrequent enough to be readily observed.

Second, Dy-647 labeled GFP aptamer was added to GFP solution of  $100nM$ . These solutions were measured with ZMWs using fluorescence correlation spectroscopy before and after adding aptamer. By careful calibration of illumination volume and photon counts from single-molecule fluorescence, and counting photon data at fine time resolution, we determined an empirical binding model. (Section 5.4.2)

### 5.4.1 Lack of Aptamer Unbinding from GFPs

One straightforward way to study molecule interactions inside ZMWs is to fix one substrate inside the ZMW, and allow a fluorescently labeled ligand to diffuse in and either associate with, or dissociate from the substrate, while its kinetics are monitored via confocal microscopy. We immobilized GFP into ZMWs using non-specific adsorption, and applied labeled aptamers in solution.

**Lack of Aptamer Unbinding** We incubated GFP in ZMW device and let the proteins adsorb non-specifically. As shown in Table 5.1. After washing with

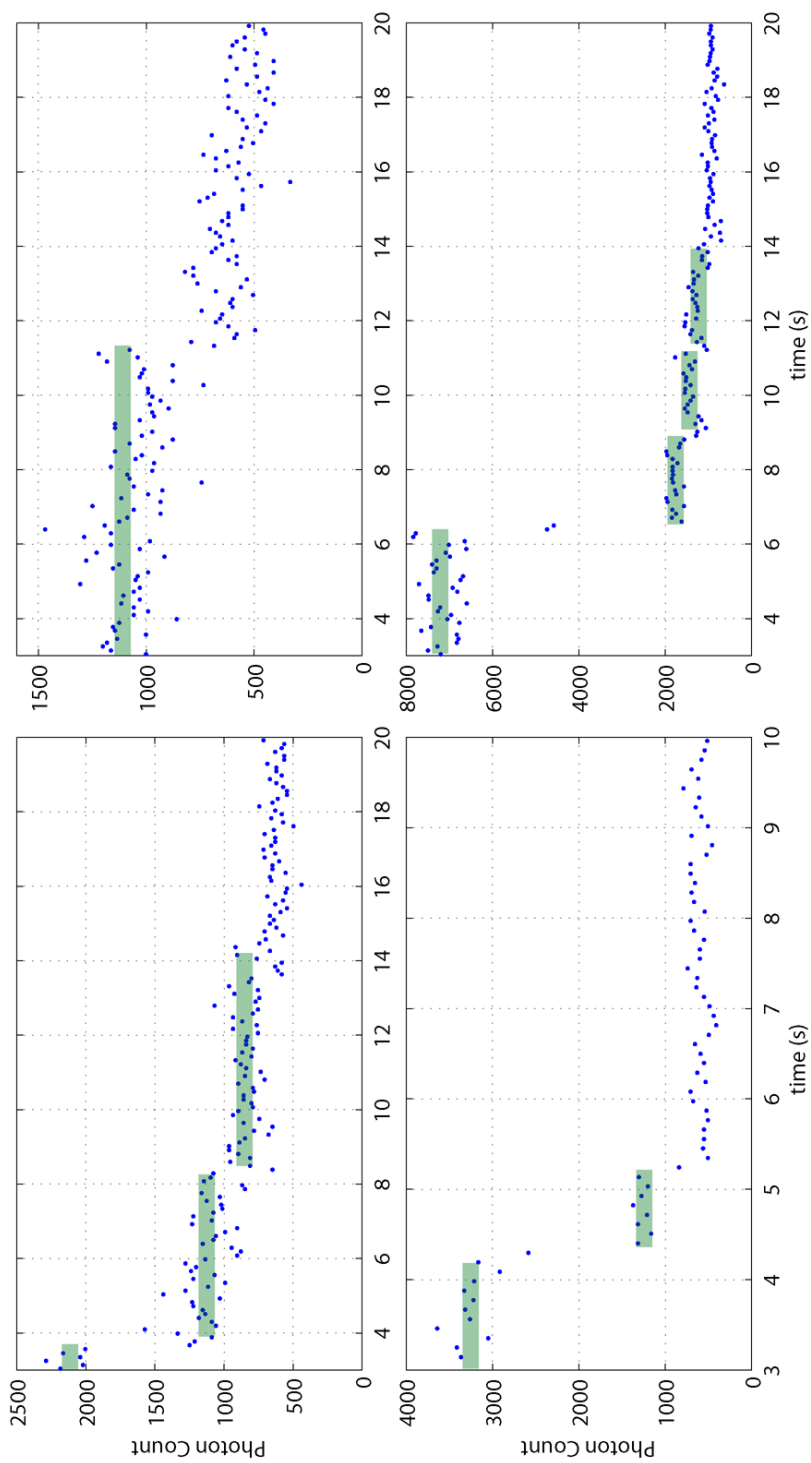
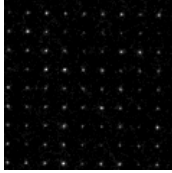
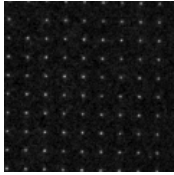
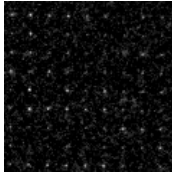
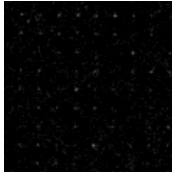


Figure 5.6: Sample photon traces from four ZMWs with adsorbed GFP and bound aptamer, showing bleaching of Cy-3 labels on bound aptamer. We drew in horizontal lines to illustrate where we think single-fluorophore bleaching occurred. There is usually more than one GFP adsorbed in a given ZMW, and hence more than one bound aptamer with Cy-3 label.

Table 5.1: Incubating GFP in ZMWs with Aptamer and Control. Cy-3 labeled AP3 clearly binds to GFP in ZMWs and partially quenches GFP fluorescence, while Cy-3 fluorescence could be detected, indicating aptamer binding.

| GFP   | Cy3-Aptamer | GFP Filter   | Cy-3 Filter   |
|---|-------------|--|---|
| in ZMW  | Cy3-AP3     |  |  |
|  | Cy3-Control |  |  |

deionized water, there was still fluorescence from GFP, indicating adsorbed proteins. After incubating with Cy-3 labeled AP3, we saw clear accumulation of Cy-3 fluorescence in the same ZMWs and a drastic drop in GFP fluorescence. On the other hand, ZMW apertures with Cy-3 labeled aptamer that had a complimentary sequence of AP3, which we call reverse aptamer, and used as a control, did not show a clear change in GFP fluorescence, nor accumulation of Cy-3 fluorescence beyond normal detectable signals from diffusing molecules.

**Photo-Bleaching Experiment** When we used a 543nm laser to illuminate ZMWs with Cy-3 labeled AP3, we saw step-wise drops of fluorescence, shown in Fig. 5.6, without seeing any step-wise increases of fluorescence. Therefore, we conclude the drop in fluorescence is due to bleaching of Cy-3 label, whereas the aptamer once bound to GFP, does not dissociate in the time frame of observation.

Direct binding and unbinding of AP3 to GFP on a single molecule level is thus difficult to detect. Due to fluorophore-to-metal interactions and the uncertainty in location of GFP inside ZMWs, we cannot tell the exact fluorescence decrease of GFP due to aptamer binding without a large number of observations to gain statistical confidence.

## 5.4.2 GFP-AP3 Interaction Model

**GFP fluorescence in Presence of GFP-Aptamer** Before considering different methods of coincidence measurements, let's consider for a moment the four possible outcomes when we mix GFP and Dy-647 labeled AP3.

| Reaction  | detect      | population | $\langle fluo \rangle$ |
|---|-------------|------------|------------------------|
| $\text{GFP} + \text{Aptamer} \xrightleftharpoons[k_{-1}]{k_1} \text{GFP-Aptamer}$ | <i>fluo</i> | $p$        | $f$                    |
|   | <i>none</i> | $1 - p$    | $-$                    |

Figure 5.7: Reaction model of GFP and GFP-aptamer.

Here we propose a general model (Fig. 5.7) that may describe what happens.

1. Nothing happens if aptamers do not bind with GFP molecules. In this case, both GFP and aptamer molecules diffuse independently. Our previous results have ruled out this possibility, as we have confirmed that aptamers bind GFP quite strongly;
2. Aptamer binds GFP molecule and completely quenches the GFP fluorescence. In this case, we see lower overall GFP fluorescence, but otherwise independent GFP and aptamer diffusion. Due to similar molecular weight

and size, it will be difficult to tell a bound complex from an unbound aptamer's diffusion behavior. We will not be able to see bound GFP because they are undetectable. In this case,  $p = 0$ ,  $f = 0$ ;

3. Aptamer binds to GFP molecule and decreases but does not completely quench GFP fluorescence. In this case, we see decreased overall GFP fluorescence, but we also see a population of GFP and AP3 molecules diffuse together, in addition to independent diffusions of free GFP and labeled AP3 molecules. In this case,  $p = 1$ , and  $0 \leq f \leq 1$ ;
4. A combination of the second and third possibilities above, where some of the aptamer-bound GFP molecules are completely dark, and some are still fluorescent. In this most general case,  $0 < p < 1$ , and  $0 \leq f \leq 1$ .

To tell if aptamer binding completely quenches GFP fluorescence, we use fluorescence cross-correlation measurements.

**Dual-Color Cross-Correlation Spectroscopy** Fluorescence-Correlation Spectroscopy is a single-molecule technique that examines the temporal relationship of molecular dynamics (21). Dual-color fluorescence cross-correlation spectroscopy was first suggested by Eigen and Rigler (20), and experimentally demonstrated in a dual-labeled nucleic acid reaction system by Schwille *et al* (87).

In cross-correlation of two species containing dual-fluorescent molecules,

the correlation functions are (87):

$$G_{DG}(\tau) = \frac{\langle C_G \rangle Diff_G + \langle C_{GR} \rangle Diff_{GR}}{V_{\text{eff}}(\langle C_G \rangle + \langle C_{GR} \rangle)^2} \quad (5.1)$$

$$G_{DR}(\tau) = \frac{\langle C_R \rangle Diff_R + \langle C_{GR} \rangle Diff_{GR}}{V_{\text{eff}}(\langle C_R \rangle + \langle C_{GR} \rangle)^2} \quad (5.2)$$

$$G_{DGD}^{\times}(\tau) = \frac{\langle C_{GR} \rangle Diff_{GR}}{V_{\text{eff}}(\langle C_G \rangle + \langle C_{GR} \rangle)(\langle C_R \rangle + \langle C_{GR} \rangle)} \quad (5.3)$$

where we have designated  $G$  for GFP,  $R$  for Dy647-labeled AP3,  $GR$  for Dy647-AP3-GFP complex,  $C$  stands for concentration, and  $Diff_*$  is the temporal fluctuation decay function of diffusion species  $*$ , which in our case, is Eq. 4.16, where the effective number of molecules in the observation volume  $V_{\text{eff}}$ , is  $N$ , and

$$G_{DGD}^{\times}(0) = \frac{N_{GR}}{N_G^{\text{tot}} N_R^{\text{tot}}} \quad (5.4)$$

where  $N_G^{\text{tot}} = N_G + N_{GR}$  and  $N_R^{\text{tot}} = N_R + N_{GR}$ .

The existence of a cross-correlation can confirm whether or not GFP aptamer binds to GFP when the two solutions are mixed, provided there is no false correlation between two detection channels due to spectral cross-talk. Fig. 5.8 shows that there is little overlap between the excitation and emission bands of GFP and Dy-647.

In addition, as we can see from Fig. 5.9, while taking autocorrelation curves of GFP or Dy-647 labeled aptamer solutions independently, we can obtain clear FCS curves for the species of interest, while observing only background fluorescence of the other detection channel. In other words, spectral bleed through from GFP detection channel to Dy-647 detection channel is insignificant and below noise, and does not produce any false cross-correlation curves.

Therefore, if there is any cross-correlation between fluorescence events in the GFP detection channel and Dy647 detection channel, it must be a result of the

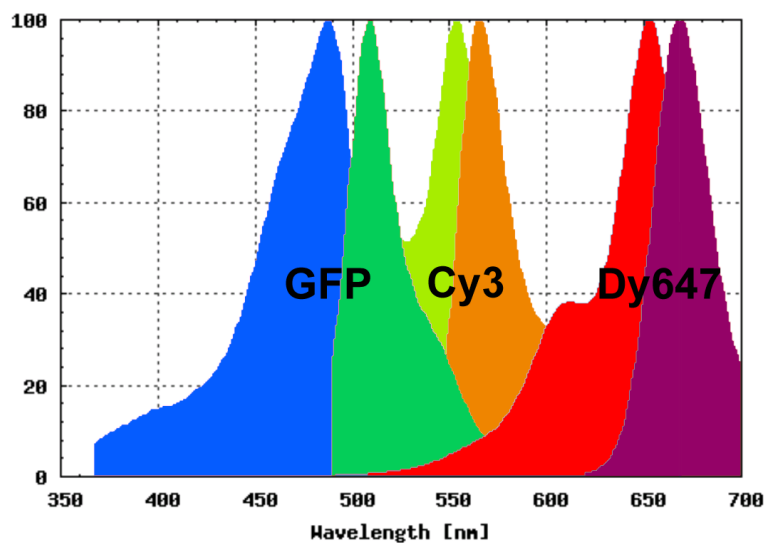


Figure 5.8: Excitation and emission spectra of GFP, Cy3, and Dy647. There is very little overlap between GFP and Dy647. Yet there is considerable spectra leak through between Cy3 and GFP, and Cy3 and Dy647.

two fluorescent molecules (GFP and Dy-647) diffusing together through the observation volume, indicating aptamer bound to still fluorescent GFP molecules.

Indeed, we can see clear cross-correlation curves of signals from green and red detection channels, indicating co-incidence of diffusion between a green and a red species (Fig. 5.10). This result strongly suggests binding of Dy-647 labeled aptamer to GFP, and these co-diffusing GFP molecules were still fluorescent, though perhaps with lower detectable fluorescence.

**Number of fluorescent GFP molecules** Derived from Eq 5.3 and 5.4, Fig. 5.11 shows concentration of fluorescent species inside ZMW observation volume. We have corrected the number of molecules by normalization using 100nM dUTP-Alexa488 and dUTP-Alexa647 fluorophores in the same apertures, re-

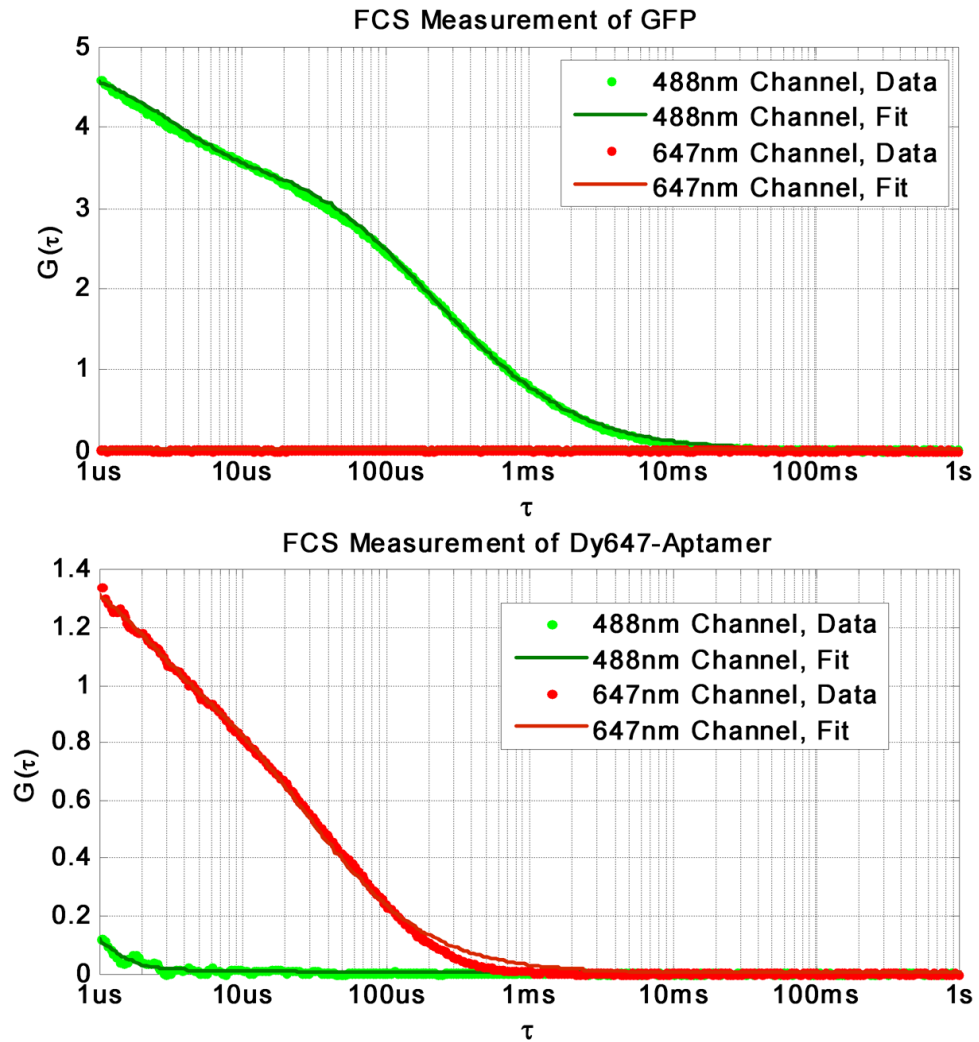


Figure 5.9: Autocorrelation curves of GFP and Dy-647-labeled aptamers independently. Lack of spectral bleed-through to the corresponding detection channel is shown as a lack in correlation curves, 647nm channel, above, and 488 channel, below.

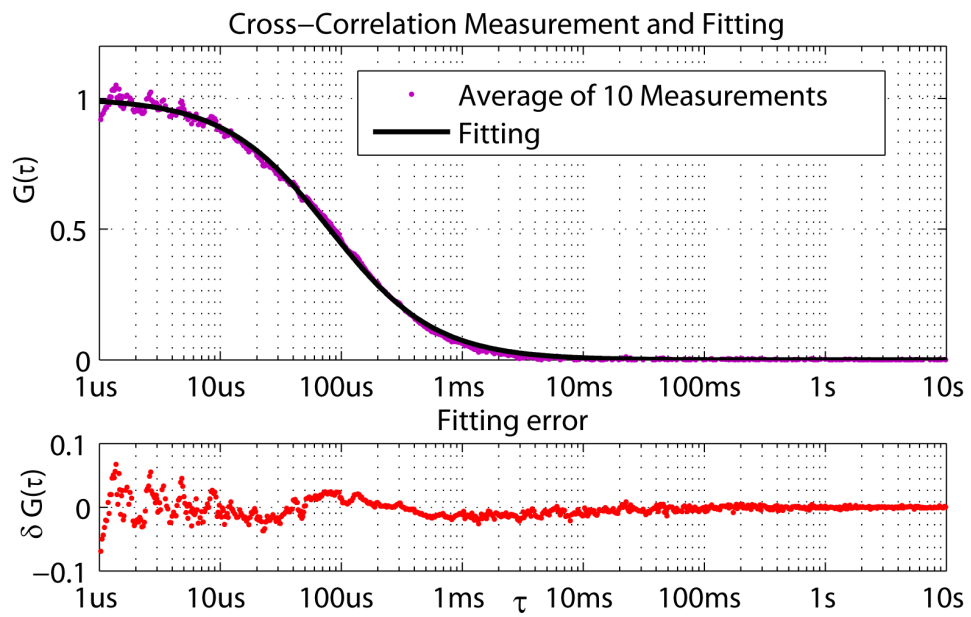


Figure 5.10: Cross correlation measurement of GFP and Dy647-labeled Aptamer. Though it is a cross-correlation curve, we find Eq. 4.16 provide a good fit.

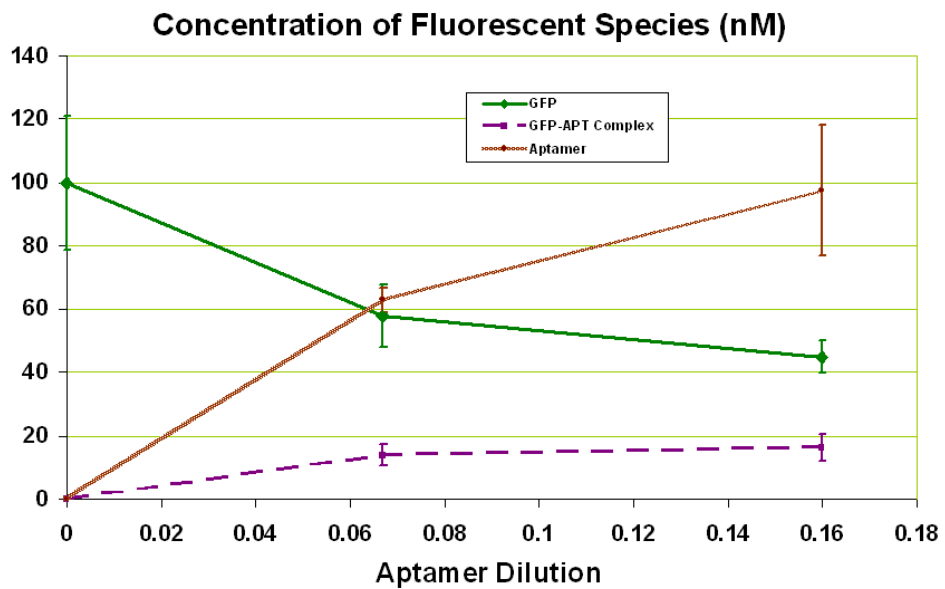


Figure 5.11: Derived concentration from average number of fluorescent molecules in a ZMW's observation volume.

spectively. The apparent GFP concentration seems to decrease as aptamer was added. We hypothesize this is a result of fluorescence quenching due to aptamer binding. Even though the total number of GFP molecules, and hence GFP concentration, remains unchanged.

**Single Molecule Counting** But to analyze photon statistics and find how many molecules are present, we need to use the cross-correlation curve to calculate average of photon pulse shape of a fluorescent molecule, i.e, GFP bound to a Dy-647-labeled aptamer, diffusing through the illumination volume of a ZMW. We note that the diffusion of molecule through the illumination volume is random and not necessarily symmetric in the time domain. However the ensemble average of many diffusions should approach a symmetric Gaussian distribution.

Using the reconstructed photon burst pulse shape as the coefficients of a matched finite impulse response (FIR) filter, we pass the collected raw photon traces through the filter and obtain a processed photon trace that clearly distinguishes a fluorophore transition event from a constant fluorescence background (noise), as shown in Fig. 5.12.

Qualitatively, we can clearly see a decrease in both intensity and frequency of GFP transitions after aptamer was added. For quantitative analysis, however, we plot the histograms as shown in Fig. 5.13.

There are several conclusions that can be drawn from Fig. 5.12 and 5.13. First of all, as aptamer is added to GFP solution, the total number of fluorescent events, i.e, GFP transiting through ZMW illumination volume, decreases.

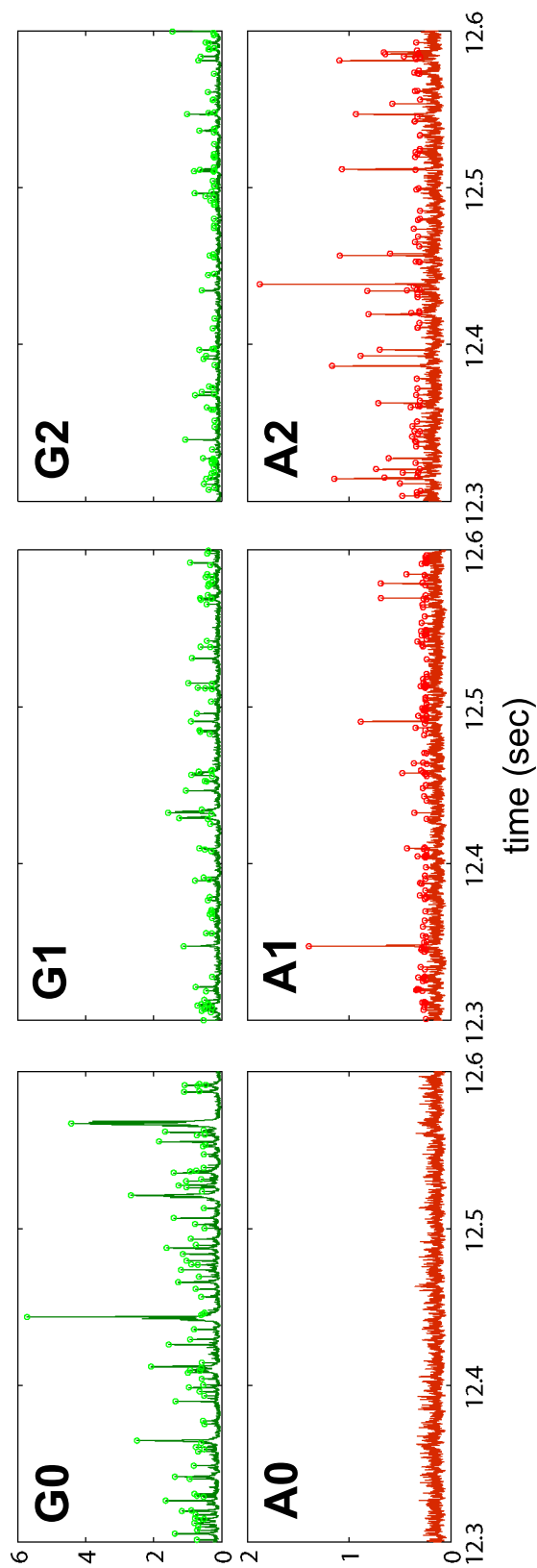


Figure 5.12: Sample photon data traces of GFP and Dy647 labeled aptamer diffusing through ZMW observation volume. Frame G0: 100nM GFP solution without aptamer, and 647nm detection channel background shown in frame A0; Frame G1: 93.3nM GFP with 0.067x aptamer solution, with detected aptamer photon trace shown in frame A1; Frame G2: 84nM GFP with 0.16x aptamer solution, with detected aptamer photon trace shown in frame A2. The slight decrease in background is noticeable from G0 to G1.

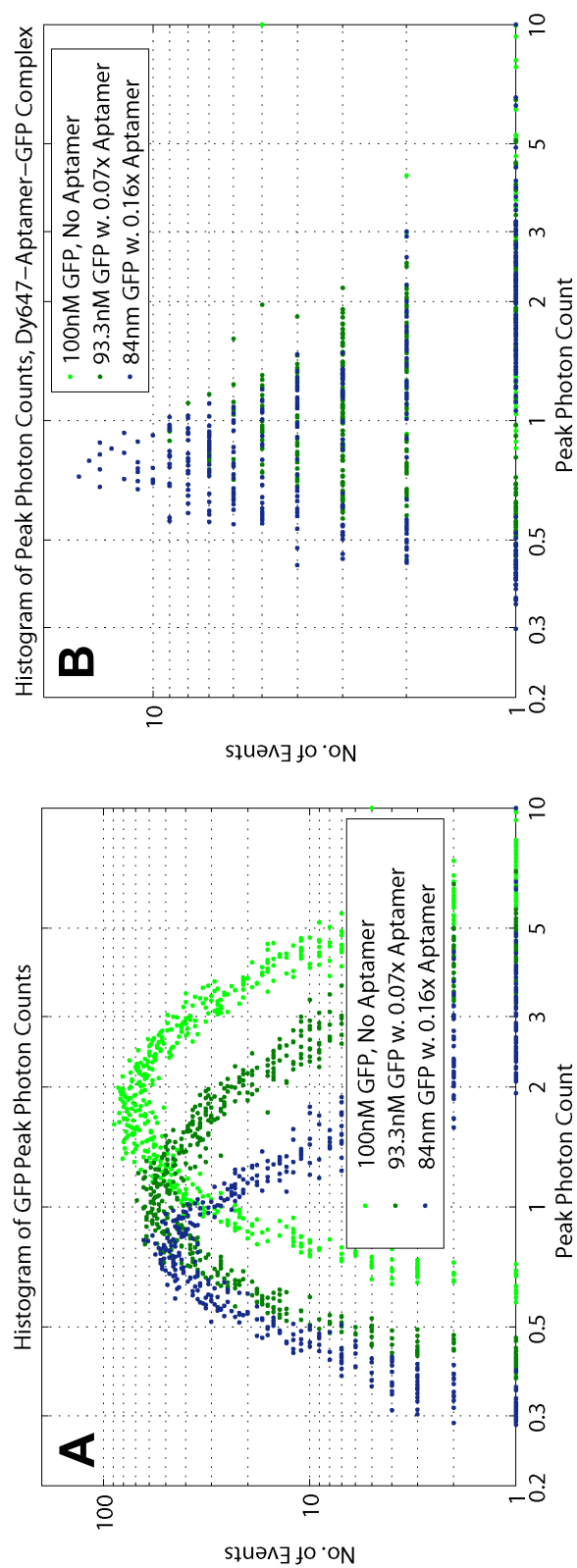


Figure 5.13: Photon statistics of GFP transition through illumination volume inside ZMW. As aptamer concentration is increased, we see a definite shift of GFP peak fluorescence towards the lower.

Secondly, when we fit peak photon data to a continuous Poisson distribution (Eq. 5.6), and obtain the peak-photon-count, as well as molecular concentration result, shown in Table 5.2, we see the peak photon count of GFP's (Fig. 5.13.A) shifts lower, and approaches the same peak photon count as GFP's bound with Dy-647-AP3 (Fig. 5.13.B). This suggests some AP3-bound GFPs are still fluorescent, while others have undetectable fluorescence.

At this point we can find the parameters in the model 5.7. First of all, the fluorescence of bound complex is (We divide peak fluorescence of complex by the peak fluorescence of free GFP)  $f = 44.9\% \pm 0.3\%$  of that of a free GFP molecule. The still fluorescent subpopulation (we divide the fluorescent events of  $84nM$  GFP with aptamer to that of  $100nM$ ) is  $p = 57\% \pm 5.8\%$ . We see  $p \cdot f = 26.5\% \pm 8.4\%$ . This agrees well with bulk measurement results of  $\sim 70\%$  fluorescence reduction. Even though we do not know the initial concentration of aptamer stock solution, we have assumed that almost all GFP molecules exist in the AP3-bound state after  $0.16\times$  aptamer dilution was added to GFP solution. We made this conclusion based on the plateauing of Dy647-GFP-AP3 curve shown in Fig 5.11, and the agreement of peak photon counts between Fig. 5.13.A and B.

We can now estimate the dissociation constant  $K_D$  of Dy647-aptamer-GFP pair to be between 300 and 420nM. However this number is calculated from the number of Dy647-labeled aptamer molecules. The actual  $K_D$  depends on the labeling ratio. A rule-of-thumb estimation of 20% labeling ratio lowers the  $K_D$  to about 100nM.

Table 5.2: Corrected concentration is the concentration of still fluorescent GFP, inferred from FCS fitting result and corrected to initial starting concentration of 100nM.

|                             | Peak Photon Count per 50 $\mu$ s | No. of Events per 30s | Concentration (nM) |
|-----------------------------|----------------------------------|-----------------------|--------------------|
| 100nM GFP, No Aptamer       | 2.161 $\pm$ 0.011                | 1716.70 $\pm$ 140.43  | 100 $\pm$ 0.68     |
| 93.3nM GFP w. 0.07x Aptamer | 1.327 $\pm$ 0.007                | 1354.77 $\pm$ 60.04   | 57.79 $\pm$ 0.32   |
| 84nM GFP w. 0.16x Aptamer   | 0.906 $\pm$ 0.022                | 977.98 $\pm$ 58.94    | 44.94 $\pm$ 0.16   |
| GFP-Aptamer Complex         | 0.970 $\pm$ 0.004                | 158.69 $\pm$ 26.56    | 16.35 $\pm$ 0.09   |

## 5.5 Conclusion

We studied GFP aptamer binding to GFP molecules. We find that upon binding, approximately 43% of the bound population has undetectable fluorescence. The rest 57% has average fluorescence that is 44.9% of the unbound GFP molecules. Therefore when there is overwhelming concentration of aptamer and almost all GFP molecules are bound, the bulk fluorescence is approximately 26.5%.

The exact quenching mechanism should be further investigated. Since the fluorochrome inside the GFP molecule is caged and protected by a  $\beta$ -barrel, it is likely that binding of aptamer caused modification of the tertiary structure of the folded GFP, thus changing the surrounding environment of the fluorochrome. However this hypothesis does not explain the fact that close to half of the bound GFP population have undetectable fluorescence. Though we used a simple fluorescent/non-fluorescent model to describe the population distribution of aptamer-bound GFP molecules, we suspect that the fluorescence absorption/emission characteristics of GFP-Aptamer complex may follow a smooth distribution curve rather than our simplified fluorescent/dark model.

Previous measurements have shown that at 426nm excitation wavelength, GFPs are insensitive to the presence of aptamer in the solution. Whereas with 390nm excitation wavelength, GFP emission increased slightly upon aptamer binding (89). This result suggests firstly, aptamer binding to GFP shifts the absorption spectra of the protein, making it less sensitive to 470nm and more sensitive at 390nm, perhaps due to a conversion of GFP between phenolate anion form into a neutral phenol form, with excitation peaks at 399nm (15). Secondly, aptamer binding and fluorescence quenching may be of two separate mech-

anisms, similar to enzyme molecule's functional domains (binding, catalytic reaction, etc), aptamer molecules, though much smaller, may be divided into sections with specific functions. The GFP aptamer was selected by the SELEX process that focuses on binding to GFP. Our result strongly suggests a SELEX process that favors fluorescence modulation may result in a molecule that has more specific result on GFP's fluorescence.

## 5.6 Appendix

### 5.6.1 Poisson Process

**Definition** A Poisson process satisfies the following two conditions:

1. The Probability  $P(X; t_1, t_2)$  that  $K$  impulses fall within the time interval  $t_1 < t \leq t_2$  is given by

$$P(X; t_1, t_2) = \frac{\left(\int_{t_1}^{t_2} \lambda(t) dt\right)^X}{X!} \exp\left(-\int_{t_1}^{t_2} \lambda(t) dt\right), \quad (5.5)$$

where  $\lambda(t) \geq 0$  is called the rate of the process.

2. The numbers of impulses falling in any two non-overlapping time intervals are statistically independent.

**Continuous Poisson Process** Even though Poisson process is only defined for integer  $K$ , the un-normalized probability distribution function of a continuous version of the Poisson process can be defined as

$$f(X; a) = A \frac{a^X e^{-a}}{\Gamma(X + 1)} \quad (5.6)$$

where  $A$  is a normalization coefficient such that  $\int_0^{\infty} f(X; a) dX = 1$ , and we have omitted explicit time-dependence of  $\lambda$  and defined  $a = \lambda(t_2 - t_1)$ , and  $\Gamma$  is the gamma function

$$\Gamma(X + 1) = \int_0^{\infty} \frac{t^X}{e^t} dt. \quad (5.7)$$

For integer  $X$ ,  $\Gamma(X + 1) = X!$ .

**Weighted Sum of Poisson Processes** Passing collected photon trace through linear filter  $h$  is equivalent to producing a random process  $Z$  from  $N$  stochastic processes  $X$ :

$$Z = \sum_{i=1}^N b_i X_i \quad (5.8)$$

where  $b_i$ 's are the coefficients of the finite impulse response filter  $h$  of length  $N$ . The expectation value of  $Z$  is

$$\mu = E[Z] = \sum_{i=1}^N b_i E[X_i] = \lambda t \sum_{i=1}^N b_i = \lambda t \quad (5.9)$$

where we have used the fact that the FIR filter is normalized to have an overall unity response. Similarly, the variance  $\nu$  of  $Z$  is

$$\nu = E[Z^2] - \mu^2 = E \left[ \left( \sum_{i=1}^N b_i X_i \right)^2 \right] - \mu^2 = \lambda t \sum_{i=1}^N b_i^2 \quad (5.10)$$

Define  $k = \mu/\nu$ , we have

$$pdf(Z) = \frac{(k\mu)^{kZ} e^{-k\mu}}{\Gamma(kZ + 1)} \quad (5.11)$$

## 5.6.2 GFP interaction with ZMW

We have observed long time-tails in fluorescence correlation curves of many molecules, and specifically in this case, the GFP molecule. We think the long time interaction of GFP molecule is due to non-specific adsorption of protein to ZMW walls. Similar interaction is found with Dye-labeled aptamers. By carefully adjusting laser power used in experiment, we can minimize the long time tail of the FCS curves, as shown in Fig. 5.14. However we need to properly control laser power in order to minimize triplet state.

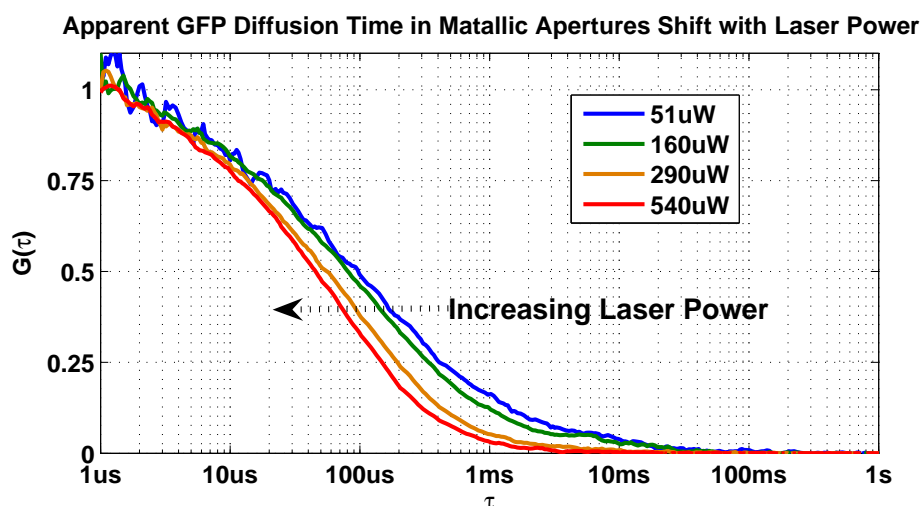


Figure 5.14: Apparent GFP Diffusion time inside metallic apertures gets shorter as excitation laser power is increased. I think this is due to GFP fluorescence gets more easily quenched at higher powers when they interact with metallic walls of the aperture.

### 5.6.3 Running GFP in Nanofluidic Channel

**Materials and Methods** A typical microfluidic device is shown in Fig. 5.15. Excitation laser was Coherent (Santa Clara, CA) diode pumped solid state laser at  $488\text{nm}$  and measured to be  $300\mu\text{W}$  before entering microscope objective's back aperture. At the excitation power, the background photon count is approximately  $1.5\text{kHz}$ . Emitted photons from fluorophores were collected through a  $60\times$  water immersion objective and focused through a pin-hole, and filtered with emission filters (Semrock, Rochester, NY) for respective fluorescence emitter, collected by avalanche photo diodes (APDs) (Perkin Elmer, Waltham, MA). Photon pulses detected from APDs were sent to 2-channel correlator box (correlator.com) and correlation data along with photon count data were sent to computer via USB cable.

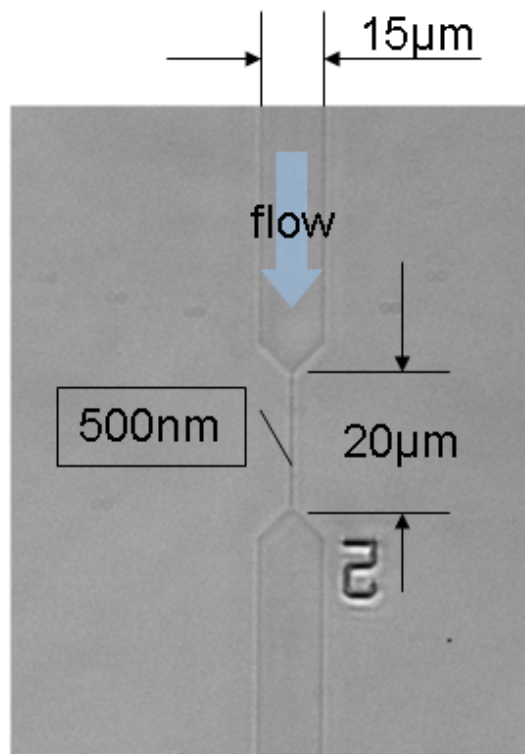


Figure 5.15: Set up for measuring single molecule fluorescence in nano-fluidic channel.

**Lack of Flow of GFP with GFP-Aptamer** We drove GFP molecules in solution through the sub-micron region, and used fluorescence-correlation-spectroscopy to study the transit time of GFP molecules through the diffraction-limited laser spot. We did not observe any time difference of GFP transit time with and without the presence of aptamer (Fig. 4). Possible reasons are 1, most GFPs are not bound to aptamers at concentrations ( $\sim 100\text{pM}$ ) used in this study; 2, GFPs bound to aptamers did not flow through the channel; or 3, Aptamer-bound GFPs did not emit detectable fluorescence.

## 5.6.4 Reconstructed GFP photon burst from correlation function

Fig. 5.16 shows reconstructed photon pulse used as matched filter for identifying GFP-AP3 diffusion events inside a ZMW. We see the characteristic time for such events is on the order of  $100\mu s$  to  $1ms$ . In addition, the shape of the pulse clearly reflects the fact that when a fluorescent molecule reaches to the bottom of the ZMW where the highest illumination is, the highest fluorescence is collected; however the molecule is more likely to spend time close to the bulk fluid side, where illumination is less, but where the space of exploration is greater.

## 5.6.5 Background Correction in FCS Models

In most cases, there is uncorrelated background in auto- and cross-correlation measurements. The modified autocorrelation function is (66)

$$G'(\tau) = \frac{\langle (F(t) + B)(F(t + \tau) + B) \rangle}{\langle F(t) + B \rangle^2} - 1 = G(\tau) \left( \frac{\langle F(t) \rangle}{\langle F(t) \rangle + B} \right)^2. \quad (5.12)$$

Therefore the background-corrected number of fluorescent molecules

$$N_c = \frac{1}{G(0)} = \frac{1}{G'(0)} \left( \frac{\langle F(t) \rangle}{\langle F(t) \rangle + B} \right)^2. \quad (5.13)$$

In the same token, considering constant background  $B_x$  and  $B_y$  in cross-correlation of fluorescence  $F_x$  and  $F_y$  collected in detection channels  $x$  and  $y$ ,

$$G'(\tau) = \frac{\langle (F_x(t) + B_x)(F_y(t + \tau) + B_y) \rangle}{\langle F_x(t) + B_x \rangle \langle F_y(t) + B_y \rangle} - 1 = G(\tau) \frac{\langle F_x(t) \rangle \langle F_y(t) \rangle}{\langle F_x(t) + B_x \rangle \langle F_y(t) + B_y \rangle} \quad (5.14)$$

Likewise the background-corrected number of fluorescent molecules

$$N_c = \frac{1}{G(0)} = \frac{1}{G'(0)} \frac{\langle F_x(t) \rangle \langle F_y(t) \rangle}{\langle F_x(t) + B_x \rangle \langle F_y(t) + B_y \rangle}. \quad (5.15)$$

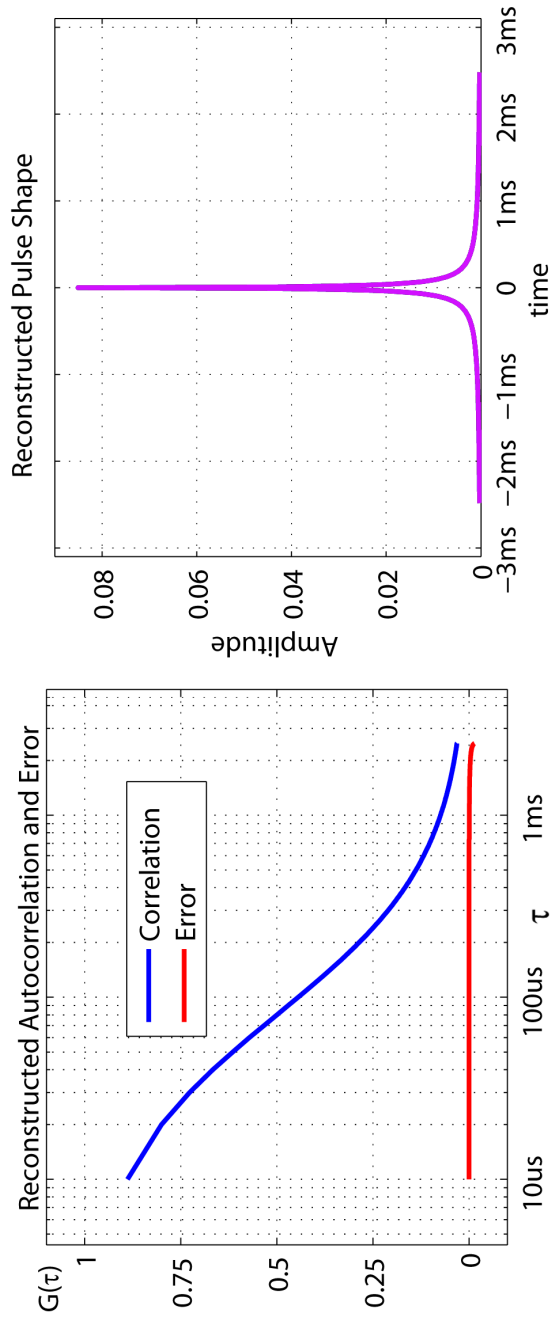


Figure 5.16: Reconstructed characteristic photon burst from FCS curve as a GFP or a Dy-647 labeled aptamer diffuses through the illumination volume of a ZMW. We also reconstruct the autocorrelation function from this photon burst and plot the error between the reconstructed correlation function from the measured correlation function.

## **Chapter 6**

# **Mobility Studies of Fluorescent Molecules under Electrophoresis**

## 6.1 Introduction

To give another demonstration of potential application using matched filter, we explore the possibility of separating molecules in fluidic channels by their mobility differences. Traditionally, gel electrophoresis has been used to separate biological molecules such as DNA and RNA or protein. In gel electrophoresis, a polyacrylamide or purified agarose gel forms a sieving matrix, in which charged molecules move at size-dependant speeds under an electric field, resulting in controlled separation (3). A similar method, capillary electrophoresis, achieves charge-dependent separation of molecules in long capillary tubes (93). With the advent of micro- and nano-fluidic channels, it's the natural next step to test and see how molecules move in ever smaller geometries.

In fact single molecule study using nanofluidic channels is very similar to capillary electrophoresis, where molecular migration is controlled by voltage applied at either ends of the capillary. Nanofluidic channels replace the capillary with lithographically defined fluidic paths for molecular migration and electric current conduction. What's more, the geometry of the fluidic channel leads to single molecule confinement, allowing experimenter to study one molecule at a time, and gaining insights to the statistical distribution of molecule binding and fluorescence labeling (13,91).

**Single Molecule Separation** In a recent study, Cipriany *et al* have demonstrated single molecule separation based on fluorescence labeling, using nanofluidic devices fabricated in fused silica substrate (12). Using a similar approach, we envision a design with a 3-way junction, where a "slower" molecule can be switched to one fluidic path, and a "faster" molecule a different path,

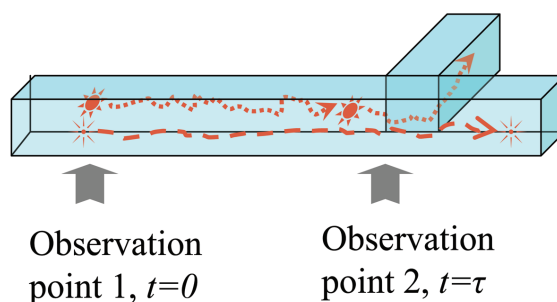


Figure 6.1: Drawing of single molecule separation in nanofluidic channels based on electrophoretic mobility.

thus achieving mobility-based separation. Fig. 6.1 shows a set up to achieve such a scheme. Along the fluidic channel, two observation spots are defined by illumination laser. As a fluorescently labeled molecule passes through the laser spots sequentially, the transit time of the molecule through the distance between the two laser spots is calculated. Molecules moving at different speeds will have different transit times between the two observation points. Given a transit time and therefore a mobility measure, a decision is made as to which subsequent path to direct the molecule.

But first, we need to select a few molecule pairs and see if we can demonstrate the feasibility of mobility measurement in nanofluidic channels.

## 6.2 Theory of Electrophoresis in fluidic Channels

A charged molecule with net charge  $q$  in electric field  $\vec{E}$  feels a Coulomb force  $\vec{F} = q\vec{E}$ . Ignoring gravity, charged molecules will accelerate under this force, until “drag” cancels out the Coulomb force. In the simplest form of 1-

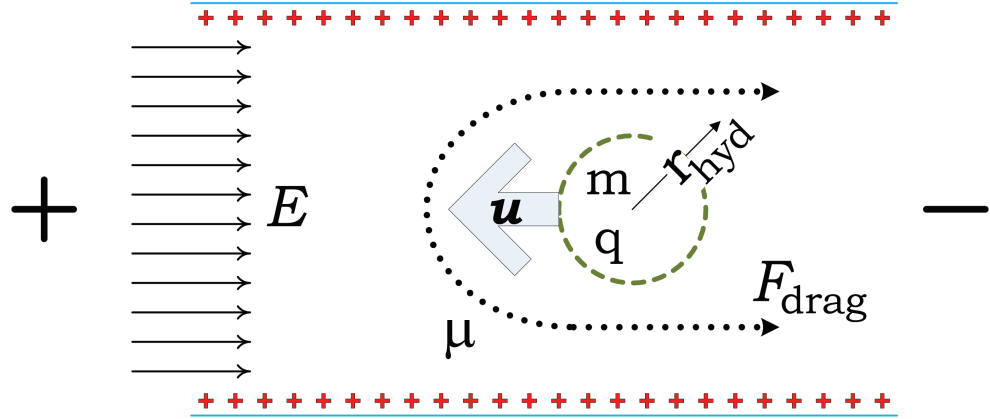


Figure 6.2: Electrophoresis model of a molecule with mass  $m$ , charge  $q$ , hydrodynamic radius  $r_{hyd}$  flowing under electric field  $E$  in nanofluidic channel where the viscosity of the fluid is  $\mu$ , leading to speed  $u$  dependent drag force  $F_{drag}$ .

dimensional electrophoretic flow, not considering diffusion, we can describe the speed  $u$  of a molecule with charge  $q$  and mass  $m$  using the basic transient equation as an external field  $E$  is applied:

$$m\dot{u} + F_{drag} = qE \quad (6.1)$$

where the dot indicates time derivative. One good model of the drag force is (42):

$$\vec{F}_{drag} \approx -6\pi\vec{u}\mu r_{hydr} \quad (6.2)$$

where  $\mu$  is viscosity of the solution and  $r_{hydr}$  is the hydrodynamic radius of the molecule, which not only depends on the molecule's physical size, but also depends on its charge distribution and the electric double layer thickness, which is buffer-dependent. We therefore have,

$$m\dot{u} + 6\pi\mu r_{hydr}u = qE \quad (6.3)$$

The general solution of this differential equation can be found using Laplace

Transform, or by guessing. It is

$$u = \frac{qE}{6\pi\mu r_{hydr}} + Ce^{6\pi\mu r_{hydr}t} \quad (6.4)$$

where  $C$  is an initial condition-defined constant. We recognize the first part of the right hand side as the steady-state solution and the second half the transient solution that decays to 0 as  $t \rightarrow \infty$ . Since the magnitude of the electric field  $E = V/d$  where  $V$  is the potential drop over channel distance  $d$ , the steady-state transit time  $\tau$  between two points separated by distance  $d$  is related by:

$$u = \frac{qV}{6\pi\mu r_{hydr}} = \frac{d}{\tau} \quad (6.5)$$

In other words,

$$\tau = \frac{q6\pi\mu r_{hydr}d}{V} \quad (6.6)$$

Here we have ignored the transient solution and assumed the molecule transit time is only due to electrophoresis and is inversely proportional to the applied voltage  $V$ . In actual measurement, we assume the voltage drop across the two laser spots  $V$  is proportional to supply voltage  $V_{DC}$  across the two reservoirs, and we lump the coefficient with the numerator  $q6\pi\mu r_{hydr}d$  and call it constant  $A$ :

$$\tau = \frac{A}{V_{DC}^k} \quad (6.7)$$

where if indeed  $\tau$  is inversely proportional to  $V_{DC}$ ,  $k = 1$ . Later we will see this is not the case for certain geometries and DC drive conditions.

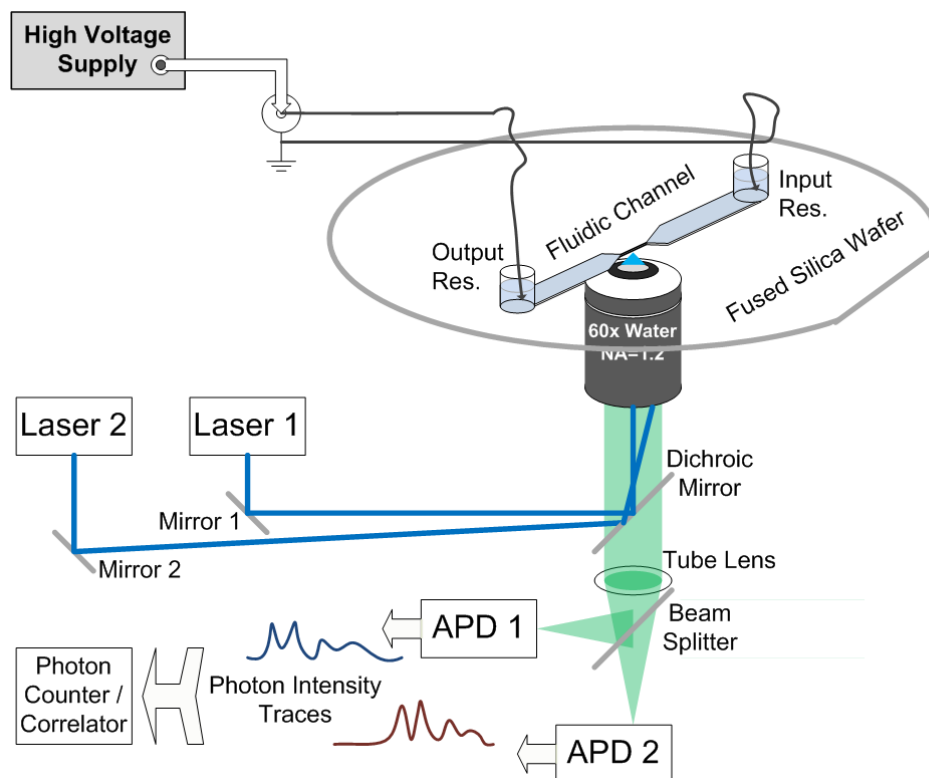


Figure 6.3: 2-spot measurement set up.

## 6.3 Materials and Methods

### 6.3.1 Optical Setup

Fig. 6.3 shows the optical set up for a 2-laser spot mobility measurement. Two independent laser sources Laser 1 and Laser 2 are combined together at the back aperture of the microscope objective. The slight angle offset of Laser 2 allows it to be focused a distance  $d$  away from the focal point of Laser 1 (See Fig. 6.9). These two laser spots are aligned along the fluidic channel in the fused silica wafer. As fluorescent molecule passes through these two laser spots, the fluorescence signal is collected via APD 1 and APD 2 sequentially. A photon

counter/correlator card (correlator.com) records raw photon counts and calculates the cross-correlation between the two photon traces.

For species with dual-color labels, Laser 1 and Laser 2 can be of different excitation wavelengths targeting the corresponding fluorophores. APD 1 and 2 can be set to collect photons from the two emission wavelengths separately using corresponding emission filters. For single-color species, to minimize uncertainty, detection channel's cross-talk should be minimized. By carefully aligning detectors' pin holes (not shown in Fig. 6.3), we determined the isolation between the two detector channels is better than 10 : 1.

### 6.3.2 Channel Fabrication

**CAD** In the microfluidic channel CAD drawing, we designed two nanofluidic regions, one straight channel (Fig. 6.4 right section), and the other a channel with twists. The purpose of this design is to test if a longer channel would attribute to molecular separation such that a longer transition time in the longer channel would result in better separation of single molecules traveling at different speeds in the fluidic channel.

**Fabrication** Microfluidic devices were fabricated using standard optical lithography techniques and complete with fusion bonding. Details of the fabrication have been described elsewhere (13, 92). We repeat the essential steps here. A thin film of i-line photoresist SPR700-1.2 (Rohm and Haas Company, Philadelphia, PA) was spun onto a 500 $\mu\text{m}$  fused silica wafer and exposed in i-line exposure tool. We optimized the exposure dose such that all exposed resist

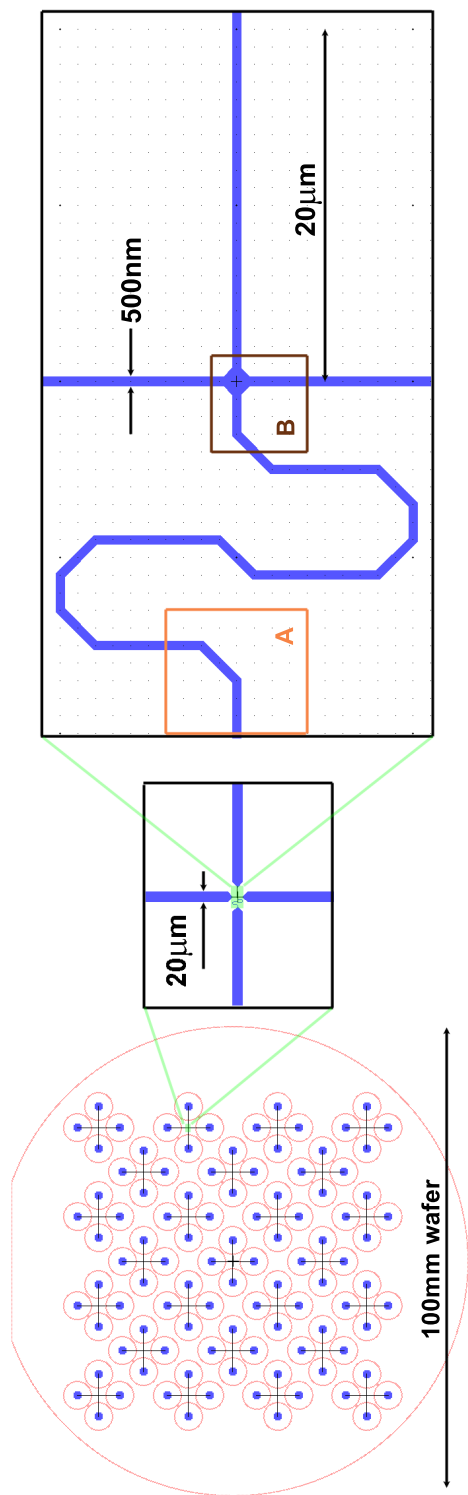


Figure 6.4: CAD design of microfluidic channels for single molecule mobility studies. The A and B windows correspond to Fig. 6.5.A and B AFM measurement frames. We have designed in a cross-junction for possible applications such as voltage/current monitoring, and providing an alternate path for single molecule separation.

Table 6.1: Channel depth as a result of etch times. Measurement was done using KLA-Tencor profilometer p10 (Milpitas, CA) with 1Å resolution.

| Etch Time ( <i>min</i> ) | Depth ( <i>nm</i> ) |
|--------------------------|---------------------|
| 3                        | 85.30±2.55          |
| 5                        | 146.35±4.45         |
| 7                        | 204.25±3.32         |
| 9                        | 256.55±0.92         |

is removed after development, yet with minimum over exposure to limit feature expansion. After pattern transfer, a CF<sub>4</sub> reactive ion etch was applied for 3, 5, 7, and 9 minutes, respectively on 4 separate wafers, so we obtained a distribution of etch depths. The resulting etch depths vary from sub-100nm to ~ 250nm, shown in table 6.1.

Using atomic force microscopy, we also found that channels at 45-degree angles were ~ 20% wider than channels with perpendicular designs (Fig. 6.5.A). We attribute this discrepancy to the mask writer used in photolithography process.

**Wafer Packaging and Bonding** After etching, both sides of the wafer were coated with a thick protective layer (~ 7μm) of photoresist. Fine alumina powder driven at ~ 80psi was used to blast ~ 1mm holes in the fused silica wafer to create access ports from the microfluidic channels to glue-on reservoirs made from pipette-tip cut-offs. The processed wafers were thoroughly cleaned repeatedly in photoresist stripping bath, hot piranha, and finally through RCA

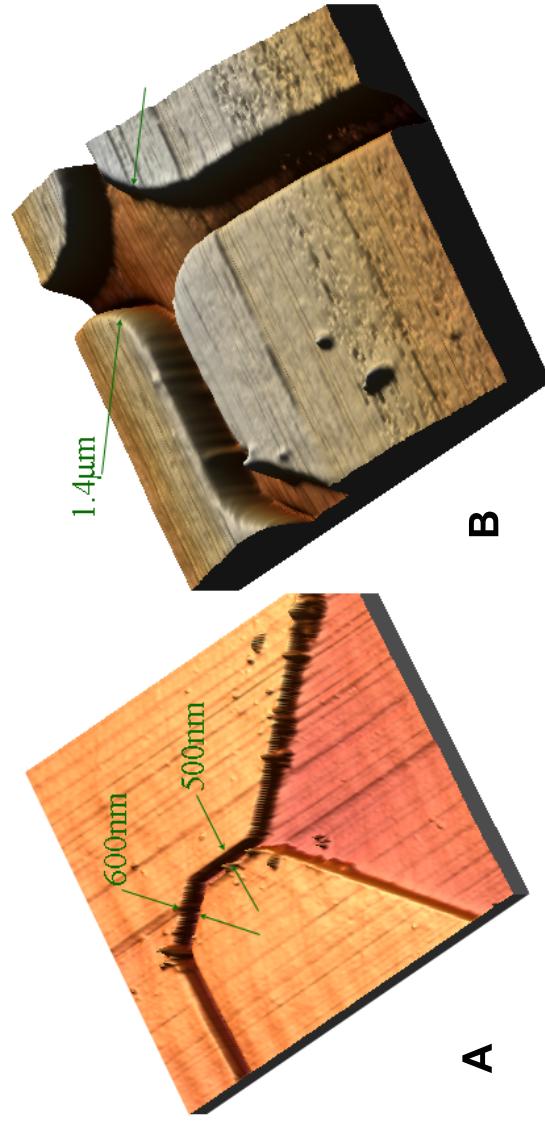


Figure 6.5: AFM image of etched channel in fused silica substrate before bonding, showing A, 45-degree bend region to be 20% wider, and B, the junction region for potential use as single molecule separation device. Surface curvature shown in frame B is an artifact of AFM.

base/acid/base wash cycle, before they were each put into physical contact with another similarly cleaned 170 $\mu$ m fused silica wafer, where surface electrostatic attraction took over and fused the two wafers together. Sometimes mechanic force was needed to push isolated trapped air bubbles out of the bonded surfaces. A slow-ramp to high temperature anneal process (up to 1100 °C) was used to make the bond permanent.

### 6.3.3 Analyte Preparation

```

5' - /5Alex488N/ TTG GGA GAA TTC AAC TGC CAT CTA GGC -3'
3' - AAC CCT CTT AAG TTG ACG GTA GAT CCG /iSp9//5Alex647N/ -5'
5' - /56-FAM//iSp9/ UUG GGA GAA UUC AAC UGC CAU CUA GGC -3'
3' - AAC CCU CUU AAG UUG ACG GUA GAU CCG /iSp9//5Cy5/ -5'

```

Figure 6.6: ssDNA and ssRNA structures for hybridization. The “iSP9” is a triethylene glycol spacer incorporated between RNA bases and fluorophores to minimize possible quenching effect due to Guanine (95).

**DNA Constructs** One of our goals is to determine if DNA and RNA electrophoresis differently in nanofluidic channels. In addition, we would like to find if single-strand DNA and single-strand RNA oligos have different mobilities compared to double-strand oligos. We therefore ordered from Integrated DNA Technologies (Skokie, IL) 4 short (27-base) oligonucleotide, each with fluorescent labels, with spectra shown in Fig. 6.6.

With these four constructs, we can hybridize the DNA pair, the RNA pair, and DNA/RNA pair, respectively. The resulting hybridization product contains a fluorophore in the FITC wavelength (Alexa-488 or FAM labels), and in the Cy-5 wavelength (Alexa-647 or Cy-5 labels), as shown in Fig. 6.7. With these

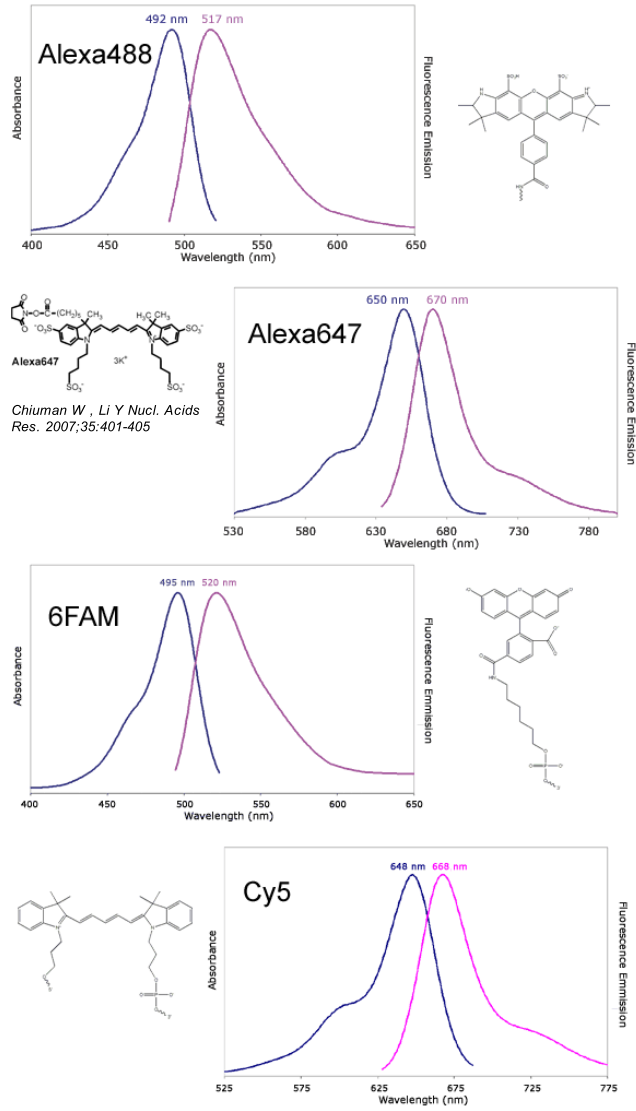


Figure 6.7: Structures and spectra of fluorescent labels on ssDNA and ss-RNA.

two fluorophores on a single molecule, we can perform cross-correlation and potentially distinguish double-strand from single-strand oligos, which contain only single-color fluorophores.

**Hybridization** We used  $75mM$  Sodium Citrate,  $750mM$  Sodium Chloride, 1% BSA, and 0.02% Sodium Dodecyl Sulfate (SDS) in aqueous solution at  $pH=7$  to hybridize DNA and RNA oligos. ssDNA or ssRNA and its complementary strands were mixed in a  $1.6mL$  eppendorf tube with the hybridization buffer at final concentration of  $5\mu M$  each. This tube was then immersed in  $62^{\circ}C$  water bath for up to an hour, before the water bath was powered off and allowed to cool naturally to room temperature over a period of several hours. The resulting solution containing hybridized dsDNA/RNA species was stored in  $50\mu L$  aliquots at  $-25^{\circ}C$  and diluted in TE buffer before use.

**Electrophoresis Buffer** We use TE buffer in experiments involving electrophoresis in nanofluidic channels. Specifically, the TE buffer contains  $10mM$  Tris base,  $1mM$  EDTA, titrated with hydrogen chloride to  $pH=7.6$ . 0.5% Polyvinylpyrrolidone (PVP) was added to prevent analyte sticking to fluidic channel walls.

### 6.3.4 Electrical Setup

A Stanford Research System (Sunnyvale, CA) high voltage supply was used to provide DC drive across the channel. DC voltages range from 10 to 2500 Volts can be applied. Using Ohm's law and device geometry, we estimate the voltage drop over the micro-channel is three-times of that over the nano-channel.

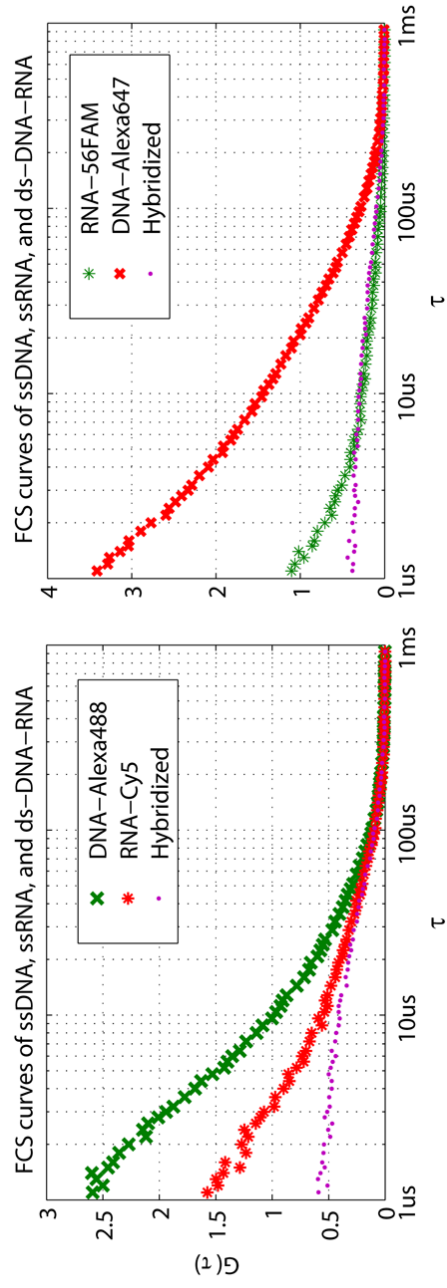


Figure 6.8: We use fluorescence correlation spectroscopy to confirm the existence of hybrid DNA+RNA molecules. The existence of cross correlation between green and red photon detection channels means there are single molecules containing both green and red fluorophores.

Therefore the voltage across the nano-channel region is approximately 1/4 of the applied voltage. The exact voltage drop across the nano-channel region cannot be measured directly. But we expect this voltage to scale linearly with applied source voltage. In the results section, however, we see there are deviations to this linearity assumption.

## 6.4 Results and Discussion

### 6.4.1 2-spot separation

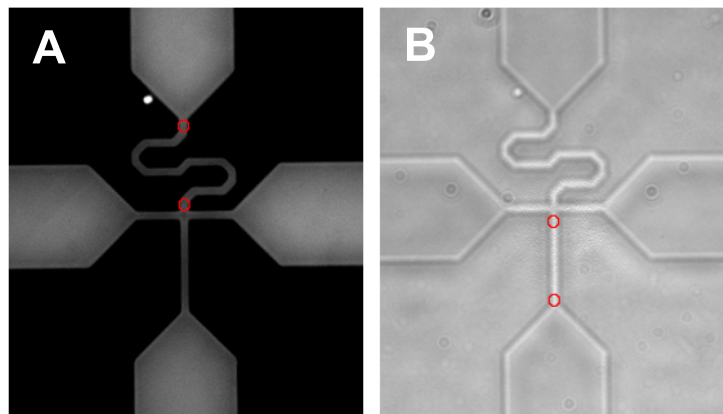


Figure 6.9: 2 laser spot set up with red circles designating laser spot location when using A. twisted channel section and B. straight channel section. Frame A was taken with arc lamp illumination, resulting in much better contrast of water-filled channel region to bonded glass region. Frame B which was taken with overhead lamp illumination, showing poorer contrast.

Using Fig. 6.9, we estimate the channel path length to be  $53.1\mu\text{m}$  between two laser spots for the twisted region, and  $16.8\mu\text{m}$  for the straight channel region. It is more than three-times in their path length difference.

## 6.4.2 From Photon Traces to Cross-Correlation

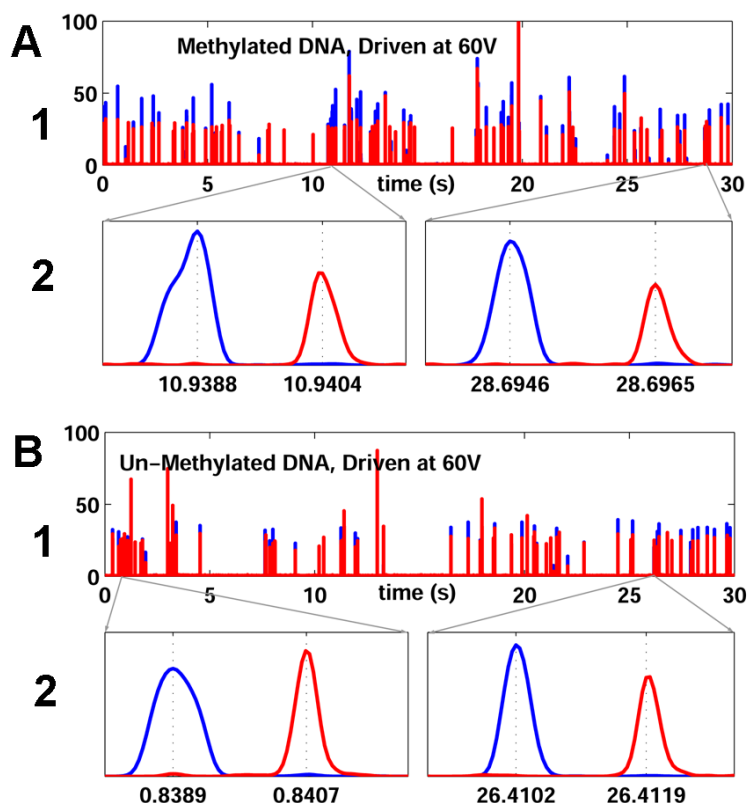


Figure 6.10: Temporal fluorescence intensity traces of A. Methylated and B. Unmethylated DNA intercalated with YOYO label driven at  $60V_{DC}$ . A2 and B2 provide sections of zoom-in view of A1 and B1. Here we used blue and red traces to illustrate two photon detection channels. The actual emission filter for YOYO label is same as FITC dye (green) and hence it is result of a single-color, dual channel detection set up.

**Flow of Yoyo labeled Methylated and Unmethylated 15kb DNA** Fig. 6.10 shows temporal photon traces of YOYO-intercalated DNA flowing through nanofluidic channels using our two-spot measurement set up. By analyzing photon traces, we see the time lag between sequential photon pulses is approximately  $16.7ms$ , for both methylated and unmethylated DNA molecules. How-

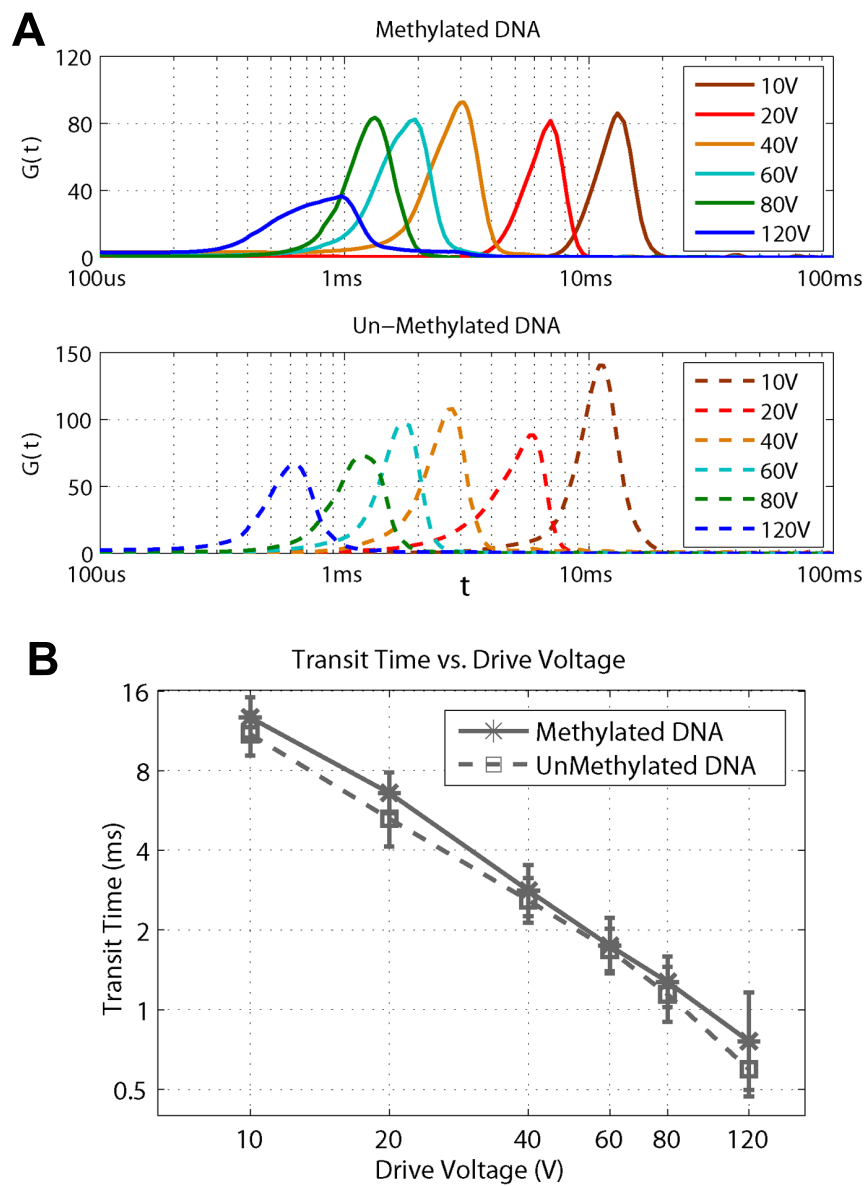


Figure 6.11: Two-spot measurement of methylated and unmethylated DNA with YOYO label in fluidic channels, showing A, cross-correlation curves with respect to voltages; and B, summary of the averages of transit times with respect to voltages.

ever to obtain a large number of measurements of time lapses and calculate a average of transit time more effectively, we use two-beam cross-correlation method (6).

Table 6.2: Characteristic times for Diffusion and Flow after we fit the data shown in Fig. 6.11 to Eq. 6.7.

| Methylation  | $A(ms \cdot V)$ | $k$       |
|--------------|-----------------|-----------|
| Methylated   | 147.8±41.7      | 1.06±0.11 |
| UnMethylated | 128.2±16.6      | 1.07±0.05 |

By correlating photon bursts from two collection channels, we can obtain cross-correlation peaks of a fluorescent species transiting through the two laser beams. By varying the drive voltage, we can get the transit-time versus voltage relationship. The mobility of the molecule can also be calculated from the two-spot separation and the transit times. Certainly the mobility of a molecule depends on the drive voltage, its charge and size, as well as buffer conditions.

For methylated and unmethylated DNA molecules, we see methylated DNA flow at a slightly slow rate than unmethylated DNA. However there is enough overlap in their transit times that they cannot be easily separated. Subsequent measurements of these two species in twisted channels with longer separation between two laser spots did not result in separable time-lapses (data not shown).

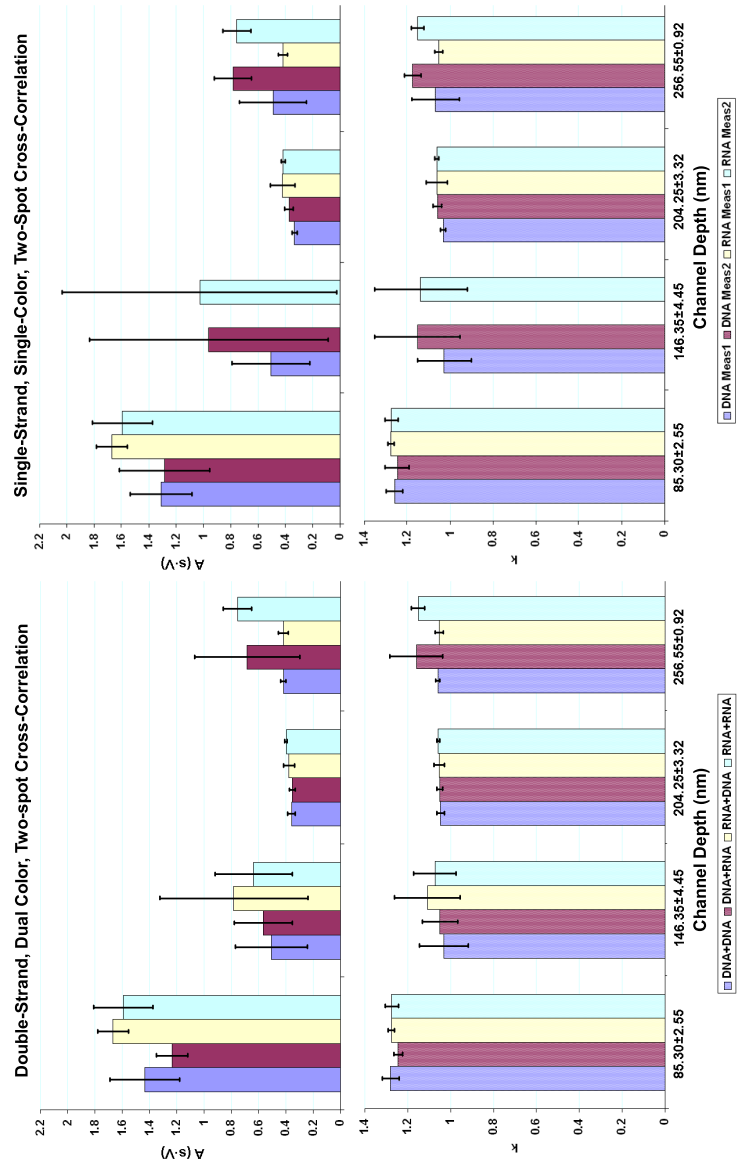


Figure 6.12: Compare mobility of hybridized and single-strand oligonucleotide.

### 6.4.3 Mobility of Different DNA Constructs

We apply the same method to study DNA and RNA constructs made from hybridized IDT samples. Similarly, we fit the results to Eq. 6.7 and obtain corresponding  $A$  and  $k$  parameters. We plot the results in Fig. 6.12.

With the exception of shallow-etch of  $85.30 \pm 2.55nm$  channels, the exponent  $k$  in Eq. 6.7 is consistently very close to 1, agreeing with the assumption that electrophoresis speed is proportional to the field strength in the channel. Therefore the transit time is inversely proportional to the applied voltage. However we do not see appreciable mobility differences between double strand and single strand DNA or RNA or their hybrid molecules. This result agrees with previously published result that DNA molecules under electrophoresis appear to be “free draining” and their mobilities are largely size-independent (97).

### 6.4.4 Differences between Long and Short Channels

We compare the effect of long and short channels in the device with etch depth of  $204.25 \pm 3.32nm$ . Seen from Fig. 6.13, the longer path length, via twisted channel design, is roughly 3.16 times of the shorter straight channel, and the transit time of hybridized DNA and/RNA molecules transit time is  $3.22 \pm 0.64$  times longer in the twisted channel than the shorter straight channel, showing excellent agreement with the theory of transit time. For the channel with etch depth of  $256.55 \pm 0.92nm$ , however, the transit times between long and short paths were  $1.54 \pm 0.82$  in ratio. We attribute this discrepancy to large measurement and fitting errors.

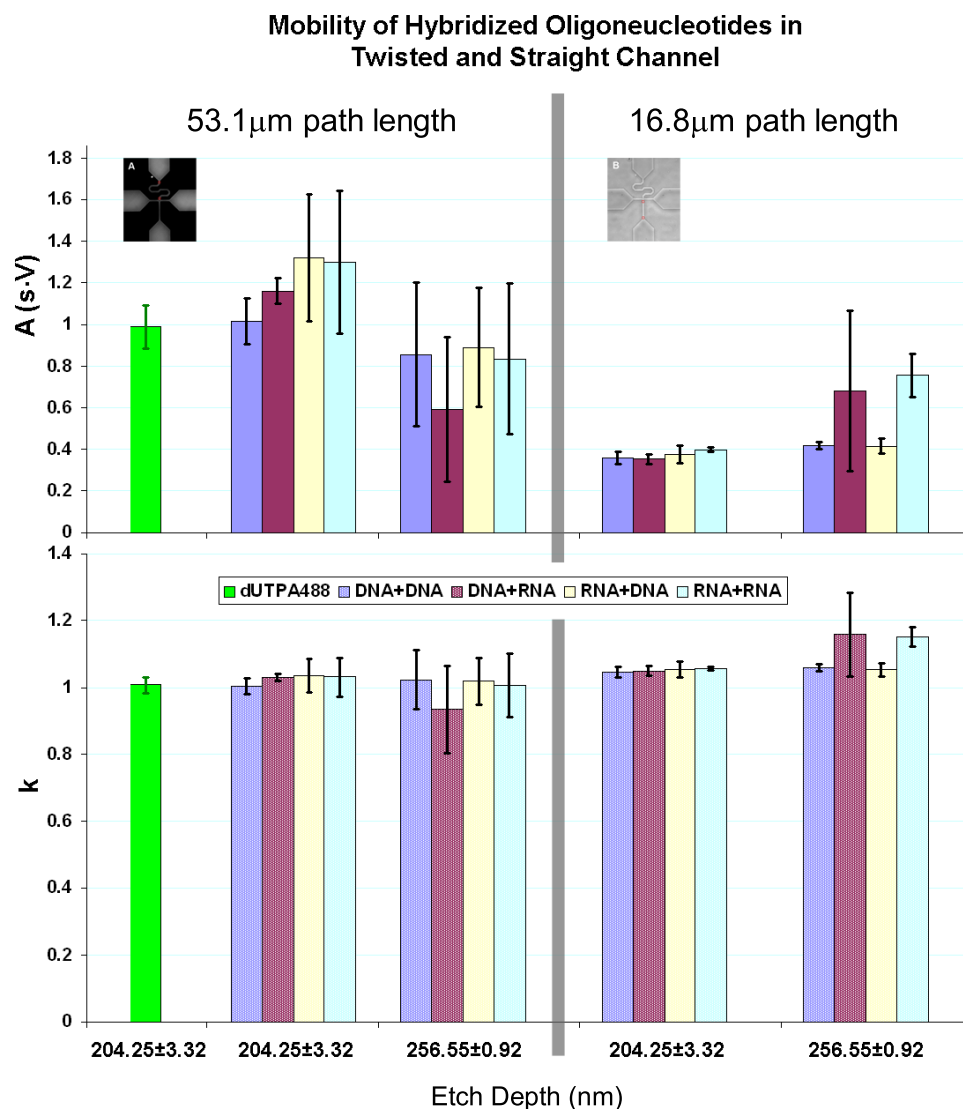


Figure 6.13: Compare mobility of hybridized oligonucleotide in twisted and straight channels of different etch depths. Measured transition times between two observation laser spots are fit to Eq. 6.7, and parameters  $A$  and  $k$  are extracted.

## 6.4.5 Differences between Shallow and Deep Channels

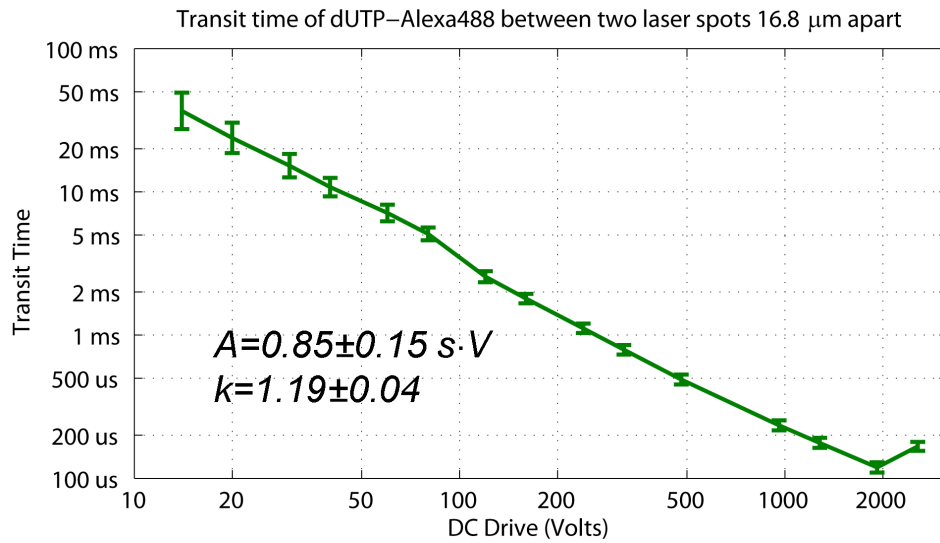


Figure 6.14: Average transit time of dUTP-Alexa488 molecule through two laser spots separated by 16.8  $\mu\text{m}$ , in shallow-etch channel with depth = 85.3  $\text{nm}$  showing non-linear relationship especially at  $V_{\text{DC}} = 2560\text{V}$ .

There seems to be no differences between shallow and deep channels for those devices with deep enough etching, until the channel depth is less than  $\sim 100\text{nm}$ , and when drive voltage is over several hundred volts.

The exception occurs in the case of the shallowest channel with etch depth 85.3  $\pm 2.55\text{nm}$ , the exponent  $k$  is approximately 1.2 for both hybridized and single-color cross-correlation results. It is unclear what may have caused this deviation from linear relationship. However it has been reported that at micro-to-nano-channel interface, there exists a concentration polarization phenomenon that can “pinch off” the nano channel like a field-effect junction (56, 57). We hypothesize that as applied voltage increases, the nanochannel region accumulates more charged ions that shrinks the effective dimension of the nanochannel. As a result, more voltage is dropped across the nanochannel, leading to

a stronger electric field. Though the number of molecules going through the channel may decrease as a result of channel narrowing, for those molecules that do go through, the average speed of electrophoresis flow is higher than that in a linear model.

In our devices, we see unexplained phenomenon that with increased voltage and for shallow channels, there is non-linear relationship between mobility and drive voltage. When voltage is above 2500V, there is apparent decrease in mobility. In our discussion so far, we have neglected electroosmotic flow that is opposite the electrophoretic direction. Electroosmotic flow depends on electric double layer thickness. When the channel dimensions are not much larger than electric double layer thicknesses, electroosmotic flow effects may not be negligible.

#### **6.4.6 Mobilities of Quantum Dots and DNA Constructs**

As a final demonstration of utility of the two-spot measurement, we compare mobility of quantum dots (QD565 from invitrogen) and hybridized DNA+DNA molecules described in Materials and Methods section. With these two species, we see clear and distinguishable transit peaks as shown in Fig. 6.15. Fitting transit times in Fig. 6.15, we obtain the following results shown in Table 6.3.

The interesting behavior to note is for quantum dot and DNA, the mobility scales with drive voltage differently. Quantum dots obviously have a higher mobility. What's more, the separation between quantum dots and DNA increases with drive voltage. We think this is due to increased polarization of quantum dots as voltage is increased, therefore increasing its effective charge

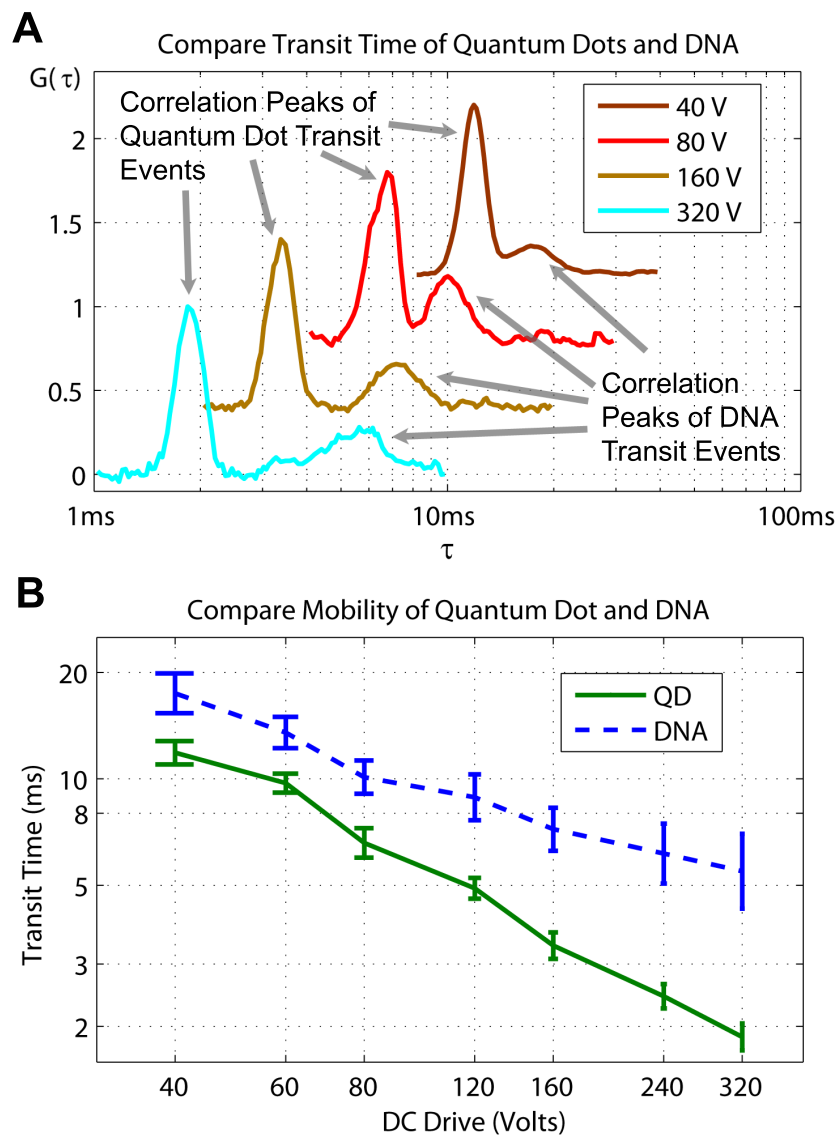


Figure 6.15: Compare transit times of Quantum Dots and DNA, both detected in the 525nm spectral range. Part A shows cross-correlation peaks due to quantum dots and DNA with varying voltages. In part B we plot the average of transit times with respect to drive voltages.

Table 6.3: Compare parameters of QD and DNA transit model.

|     | $A(ms \cdot V)$   | $k$           |
|-----|-------------------|---------------|
| QD  | $300.4 \pm 199.8$ | $0.9 \pm 0.2$ |
| DNA | $156.5 \pm 66.6$  | $0.6 \pm 0.1$ |

on the particle. At voltages above 100V, quantum dots and DNA have clearly separable peaks. With 320V drive voltage for example, we can recognize those that transit through a  $16.8\mu m$  separation in less than 3ms to be quantum dots, and those that use longer time to be DNA.

In addition, the inverse relationship of transit time to drive voltage is far from linear ( $k \neq 1$ ) in this result. The exact mechanism for such deviation remains to be explored. We suspect the interaction of streptavidin-coated quantum dots with fluidic channel walls has appreciable effect on channel geometry and electrophoretic behavior.

## 6.5 Conclusion

We have demonstrated the possibility of using nanofluidic channels to measure and distinguish single molecules with different mobilities. We have shown that DNA and RNA molecules, regardless of single or double-strand, or number of bases, have indistinguishable mobility. Only methylated long DNA molecules show a slightly lower mobility compared to their un-methylated counterparts. However this little difference is insignificant to separate a mixed population in the nanofluidic channel. When we compare DNA molecules and quantum dots,

however, we see the two do have significant mobility differences, and enhanced by increasing drive voltages.

When there is enough separation between two molecules, we can activate a voltage switch, and drive the selected molecule one way and keep the other molecule in a separate path, thus achieving separation of single molecules based on mobility differences. We introduce a possible set up for such an experiment in the next chapter on future research.

## **Chapter 7**

### **Summary and Future Studies**

## 7.1 Summary

### 7.1.1 Techniques to Increase SNR in Single Molecule Studies

In this dissertation we demonstrated two techniques for signal-to-noise ratio enhancement, namely spectral deconvolution and matched filtering. In short, both techniques use our existing knowledge about the signal, and effectively integrate all of the collected energy, thus obtaining a time or spectral integration that elevates the signal with respect to noise.

These methods are used in conjunction with existing techniques of fluorescence microscopy, such as confocal laser scanning microscopy, ZMWs and nanofluidic channels, in order to shrink observation volume and reduce background noise. We also used redox buffer in labeled cellulase binding experiment to increase the fluorescence life time of a fluorophore, increasing the number of photons collected, and hence increasing redundancy while reducing uncertainty.

Here we see an integration of optical engineering, biochemistry, and electrical engineering in uncovering kinetics in the microscopic world. Signal processing is just one piece of a big puzzle called single molecule research. Every piece has to work together in order to produce useful results. Since the goal of any experiment is to obtain information of the system under study, and signal is a vessel carrying the information, we wish to maximize the signal in order to minimize the uncertainty, and obtain the best estimate of the system. When signal power is low, for example in single-molecule studies, signal processing is particularly needed to enhance signal to noise ratio.

## 7.2 Future Research

### 7.2.1 Single Molecule Studies in ZMW and nanofluidic Channels

With advances in micro- and nano-lithography, many additions can be made to current single molecule techniques, giving current structures more specific and target-oriented applications. For example in ZMWs, surface coating can be used to non-specifically block the aluminum oxide or silicon dioxide, giving access to specific areas of the structure for small volume observation. Functionalization of ZMWs have been reported by selectively passivating the aluminum oxide surface with polyvinyl phosphonic acid, and allowing neutravidin adsorption to glass forming a base for targeted molecule attachment (43). Such structures can be integrated with microfluidic channels, allowing microscopic observation of biochemical reactions in flow. Likewise, microfluidic channels can be functionalized by packing the channel with microscopic beads, thus constructing a sieving matrix much like a gel-filled capillary, though at a much smaller scale.

A common theme running through these experimental ideas is integration of nanofabrication with biochemistry and surface chemistry. In short, we wish to functionalize devices and give them either broader or more specific capabilities in order to extract information of a biomolecule.

While smaller structures can be made with improved lithography techniques, the methods to couple signal out of the detection device are still macroscopic in nature. For example in ZMWs, although the fluorophore excitation is confined to an evanescent volume, the detection of fluorescence occurs in the

far field and photons are collected by APDs. Therefore there may be significant background that can also be collected. Even in nanopore-like structures, where electrical detection is used, the electronic probes are immersed in a macroscopic environment, subject to thermal fluctuations, resulting thermal noise. In an ever decreasing observation volume, there is an ever increasing need for signal processing, to extract information from very tiny signals.

### 7.2.2 Cellulose

In the previous paragraph we touched on the boundary between microscopic phenomenon and macroscopic instrumentation. Breaking this boundary requires careful understanding of the subject under study. The cellulase binding to pretreated wood particles is a good example to illustrate this point. In this study, there are two convoluted mechanism at work. The first is diffusion of cellulases into the porous structures of wood particles. The second is the adsorption of cellulases onto accessible sites of the particles. Our effort is one of the first in studying pretreated cellulose particles between the micro and macro-scale. We found that adsorption of cellulases onto cellulose is a much faster process than diffusion process. Yet the adsorption of cellulases is a microscopic reaction, whereas diffusion process of the enzymes is a macroscopic one. Binding constants extracted from kinetic model applied to CLSM data confirmed previously published results. However, determining the exact rate was hindered by the large variation in morphology of the pretreated material, which is a direct consequence of using the substrate with macro scale variations to study phenomenon at the sub-micro-scale level. Therefore for future studies using confocal scanning microscopy, we should concentrate on materi-

als with a more uniform morphology, or concentrate on sub-micron features to determine cellulase-cellulose interactions. In other words, we can use a microscopic method to study microscopic enzyme adsorption, and use a macroscopic method to study the diffusion process.

### **7.2.3 System Integration with Electronics**

With improved integration of electronics, many signal processing can be performed with little hardware real estate. In fact with advances in digital signal processing, lots of processing traditionally carried out in hardware can now be done in software. The advantage of software implementation of signal processing is lower cost and faster speed of development. Obviously software processing requires an initial investment of computing power. The consequence of that is subsequent development of methodology can be quickly implemented and tested in software execution rather than application-specific, potentially costly and time-consuming hardware design and production.

For example correlation measurement so far has been carried out using raw photon counts. When there is spectral bleed-through, there will be false cross-correlation, or worse, increased background that reduces correlation signal. We can think of a system that implements spectral deconvolution before the photon traces are fed to the correlator. Though a background correction step can be implemented after the correlation curve is obtained, a pre-correlation spectral deconvolution step can dynamically remove bleed-through signal and provide better signal to noise ratio.

As a second example, matched filter can be constructed in real time after

photon data has been collected for a few seconds, enough to generate an autocorrelation function. In experiments using nanofluidic channels for instance, such dynamically constructed matched filter can be used quickly and adapted to flow conditions, accurately picking out single molecule transit events.

## 7.2.4 Single Molecule Sorting Based on Mobility

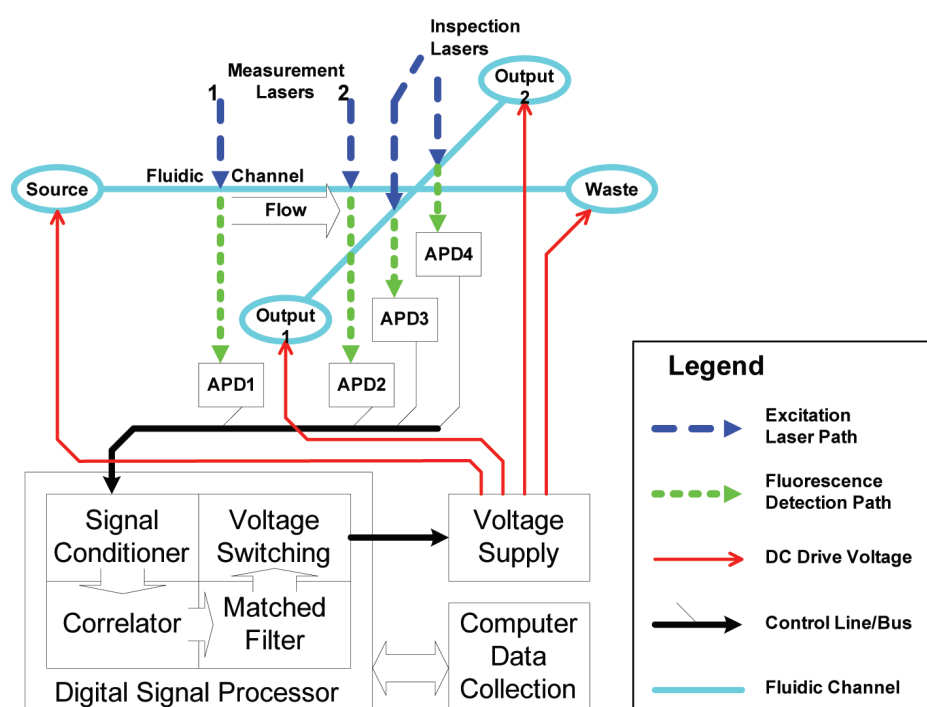


Figure 7.1: Block diagram of single molecule separation based on electrophoretic mobility differences in fluidic channels. With four interrogation spots and four detection devices, fluorescent photon counts are fed to digital signal processor to be filtered and used to calculate molecule mobility in real time. A sorting voltage is triggered based on an empirically determined and dynamically adjustable threshold.

Now that we have demonstrated the possibility of determining different mo-

bilities in nanofluidic channels in Chapter 6, we can design a sorting device that separate molecules based on their mobility differences, as shown in Fig. 7.1. Here we integrate nanofluidic device with optics and electronic measurement and control systems, all implemented in a digital signal processor. The advantage of using a digital signal processor as opposed to a hard-wired control device is the ability to dynamically adjust sorting parameters based on flow conditions, achieving fast and accurate results in real time.

Much improvement can be made on this proposed device, too. For example, rather than using four independent lasers as excitation sources, an diffractive optics element (48) can be placed in the optics path and split one laser beam into four (or however many necessary) discrete spots, thus saving hardware space, and reducing cost. It provides the added benefit of high utilization of laser power, as there is no unnecessary illumination in areas where excitation light is not needed. Similarly, the discrete detection elements (APDs) can be replaced with a highly sensitive camera. Although in general, a camera has a slower response than an APD, it has the benefit of large imaging area. Trade-offs between imaging area and processing speed can be made, such that only a few imaging pixels are selected to be processed, thus achieving higher processing speed, yet with massively parallel capabilities.

### **7.3 Conclusion**

In this dissertation we have seen a few examples of single molecule studies, in which we have built upon knowledge of previous researchers, and added our own contribution. Specifically, we used confocal laser scanning microscopy

and obtained high resolution images of pretreated wood particles. In the same experiment we used fluorescently labeled enzymes to study quantitative enzyme adsorption kinetics. In processing the experimental data, we developed the spectral deconvolution method. Though spectral deconvolution algorithms have been bundled with commercial fluorescence microscopy software, their application to specific substrate, in our case, pretreated wood, called for careful characterization of both the microscopy system and the substrate itself. Similarly, we adapted matched filter algorithm to single molecule studies in nanofluidic channels and ZMWs. Though matched filter has been used in image processing, for example face detection and recognition, their application to photon burst studies has not been documented before in scientific literature. Yet their development was closely related to radar echo processing, which is another form of photon burst, though at much longer wavelengths.

In this final chapter we have listed a few possible areas for improvement and future research effort. Indeed the possibilities for experiments are without bounds. The common theme I have followed is to apply existing engineering techniques to single molecule studies. Experiments at the single molecule level is relatively new compared to other engineering techniques, partly because such experiments were only made possible as a result of improvements in instrumentation. As more and more data are generated in such endeavor, it is essential that data processing follows up in order to make sense of the experimental results. Here is where we see a merge of engineering know-how with practices in biology. Personally, I find this multi-disciplined approach to research one of the best traits of Cornell.

The gorges are great, too.

## BIBLIOGRAPHY

1. Dragos Amarie, Nathan D. Rawlinson, William L. Schaich, Bogdan Dragnea, and Stephen C. Jacobson. Three-dimensional mapping of the light intensity transmitted through nanoapertures. *Nano Letters*, 5:1227–1230, 2005.
2. G. Beldman, A. G. J. Voragen, F. M. Rombouts, M. F. Searle van Leeuwen, and W. Pilnik. Adsorption and kinetic behavior of purified endoglucanases and exoglucanases from *Trichoderma viride*. *Biotechnology and Bioengineering*, 30:251–257, 1987.
3. Milan Bier. *Electrophoresis: theory, methods, and applications*. Academic Press, third edition, 1959.
4. Matthew R. Boelkins, Merle C. Potter, and Jack L. Goldberg. *Differential Equations with Linear Algebra*. Oxford University Press, 2009.
5. M.K. Bothwell, D.B. Wilson, D.C. Irwin, and L.P. Walker. Binding reversibility and surface exchange of *Thermomonospora fuscus* E<sub>3</sub> and E<sub>5</sub> and *Trichoderma reesei* CBHI. *Enzyme Microb. Technol.*, 20:411–417, 1997.
6. Michael Brinkmeier, Klaus Dörre, Jens Stephan, and Manfred Eigen. Two-beam cross-correlation: A method to characterize transport phenomena in micrometer-sized structures. *Analytical Chemistry*, 71:609–616, 1999.
7. B. L. Browning, editor. *The Chemistry of Wood*. John Wiley & Sons, Inc., 1963.
8. C.K. Carniglia, L. Mandel, and K.H. Drexhage. Absorption and emission of evanescent photons. *Journal of the Optical Society of America*, 62:479–486, 1972.
9. Martin Chalfie, Yuan Tu, Ghia Euskirchen, William W. Ward, and Douglas C. Prasher. Green fluorescent protein as a marker for gene expression. *Science*, 263:802–805, 1994.
10. Henri Chanzy, Bernard Henrissat, and R. Vuong. Colloidal gold labelling of 1,4- $\beta$ -d-glucan cellobiohydrolase adsorbed on cellulose substrates. *FEBS Letters*, 172:193–197, 1984.

11. David Keun Cheng. *Field and Wave Electromagnetics*. Addison-Wesley, second edition, 1990.
12. Benjamin R. Cipriany, Patrick J. Murphy, Jame Hagarman, Paul D. Soloway, and Harold G. Craighead. Single molecule sorting in nanofluidics: Real-time analysis and selection of methylated dna. *PNAS*, page In Review, 2011.
13. Benjamin R. Cipriany, Ruqian Zhao, Patrick J. Murphy, Stephen L. Levy, Christine P. Tan, Harold G. Craighead, and Paul D. Soloway. Single molecule epigenetic analysis in a nanofluidic channel. *Analytical Chemistry*, 82:2480–2487, 2010.
14. Earl A. Coddington and Robert Carlson. *Linear Ordinary Differential Equations*. Society for Industrial and Applied Mathematics, 1997.
15. Andrew B. Cubitt, Leslie A. Woollenweber, and Roger Heim. Understanding structure-function relationships in the aequorea victoria green fluorescent protein. In Kevin F. Sullivan and Steve A. Kay, editors, *Green Fluorescent Proteins*, volume 58 of *Methods in Cell Biology*, pages 19–30. Academic Press, 1998.
16. A. Degiron, H.J. Lezec, N. Yamamoto, and T.W. Ebbesen. Optical transmission properties of a single subwavelength aperture in a real metal. *Optics Communications*, 239:61–66, 2004.
17. W. Denk, J.H. Strickler, and W.W. Webb. Two-photon laser scanning fluorescence microscopy. *Science*, 248(4951):73–76, 1990.
18. Robert M. Dickson, Andres B. Cubitt, Roger Y. Tsien, and W. E. Moerner. A dozen years of single-molecule spectroscopy in physics, chemistry, and biophysics. *J. Phys. Chem. B*, 106:910–927, 1997.
19. T. W. Ebbesen, H. J. Lezec, H. F. Ghaemi, T. Thio, and P. A. Wolff. Extraordinary optical transmission through sub-wavelength hole arrays. *Nature*, 391:667–669, February 1998.
20. M Eigen and R Rigler. Sorting single molecules: application to diagnostics and evolutionary biotechnology. *PNAS*, 91(13):5740–5747, June 1994.
21. Elliot L. Elson and Douglas Magde. Fluorescence correlation spectroscopy. *Biopolymers*, 13:1–27, 1974.

22. B.J. Fergus, A.R. Procter, J.A.N. Scott, and D.A.I. Goring. The distribution of lignin in sprucewood as determined by ultraviolet microscopy. *Wood Science and Technology*, 3:117–138, 1969.
23. U. Ch. Fischer and H. P. Zinsheim. Submicroscopic pattern replication with visible light. *Journal of Vacuum Science and Technology*, 19(4):881–885, 1981.
24. Mathieu Foquet, Kevan T. Samiee, Xiangxu Kong, Bidhan P. Chauduri, Paul M. Lundquist, Stephen W. Turner, Jake Freudenthal, , and Daniel B. Roitman. Improved fabrication of zero-mode waveguides for single-molecule detection. *Journal of Applied Physics*, 103(3):034301, 2008.
25. M. Galbe, R. Eklund, and G. Zacchi. Adsorption of cellulases on steam-pretreated willow. *Appl. Biochem. Biotech.*, 24-25:87–101, 1990.
26. Taekjip Ha. Single-molecule fluorescence resonance energy transfer. *Methods*, 25:78–86, 2001.
27. Stefan W. Hell, Ernst H. K. Stelzer, Steffen Lindek, and Christoph Cremer. Confocal microscopy with an increased detection aperture: type-b 4pi confocal microscopy. *Optics Letters*, 19(3):222–224, 1994.
28. Stefan W. Hell and Jan Wichmann. Breaking the diffraction resolution limit by stimulated emission: stimulated-emission-depletion fluorescence microscopy. *Optics Letters*, 19:780–782, 1994.
29. B. Ilic, H.G. Craighead, S. Krylov, W. Senaratne, C. Ober, and P. Neuzil. Attogram detection using nanoelectromechanical oscillators. *J. Appl. Phys.*, 95:3694–3703, 2004.
30. Satoshi Inouye and Frederick I. Tsuji. Aequorea green fluorescent protein: Expression of the gene and fluorescence characteristics of the recombinant protein. *FEBS Letters*, 341:277–280, 1994.
31. John David Jackson. *Classical Electrodynamics*. Wiley, third edition, 1998.
32. Tina Jeoh, D.B. Wilson, and Larry P. Walker. Cooperative and competitive binding in synergistic mixtures of *Thermobifida fusca* cellulases cel5a, cel6b, and cel9a. *Biotechnol Prog*, 18(4):760–769, 2002.
33. Eric J. Jervis, Charles A. Haynes, and Douglas G. Kilburn. Surface diffusion

- of cellulases and their isolated binding domains on cellulose. *Journal of Biological Chemistry*, 272(38):24016–24023, 1997.
34. Kenneth A Johnson. Enzyme kinetics: Transient phase. In *Encyclopedia of Life Sciences*. John Wiley & Sons, Ltd., 2005.
  35. E.D. Jung, G.F. Lao, D. Irwin, B.K. Barr, A. Benjamin, and D.B. Wilson. Dna-sequences and expression in *Streptomyces lividans* of an exoglucanase gene and an endoglucanase gene from *Thermomonospora fusca*. *Appl Environ Microbiol*, 59(9):3032–3043, 1993.
  36. Hyungil Jung, David B. Wilson, and Larry P. Walker. Binding mechanisms for *Thermomonospora fusca* Cel5A, Cel6B, and Cel48A cellulose-binding modules on bacterial microcrystalline cellulose. *Biotechnology and Bioengineering*, 80(4):380–392, 2002.
  37. Hyungil Jung, David B. Wilson, and Larry P. Walker. Binding of *Thermomonospora fusca* CD<sub>Cel5A</sub>, CD<sub>Cel6B</sub>, and CD<sub>Cel48A</sub> to easily hydrolysable and recalcitrant cellulose fractions on BMCC. *Enzyme and Microbial Technology*, 31(7):941–948, 2002.
  38. Hyungil Jung, David B. Wilson, and Larry P. Walker. Binding and reversibility of *Thermomonospora fusca* Cel5A, Cel6B, and Cel48A and their respective catalytic domains to bacterial microcrystalline cellulose. *Biotechnology and Bioengineering*, 84(2):151–159, 2003.
  39. Christopher V. Kelly, Barbara A. Baird, and Harold G. Craighead. An array of planar apertures for near-field fluorescence correlation spectroscopy. *Biophysical Journal*, 100(7):L34–L36, 2011.
  40. Dong Won Kim, Tae Seung Kim, Young Kyo Jeong, and Jae Kuk Lee. Adsorption kinetics and behaviors of cellulase components on microcrystalline cellulose. *Journal of Fermentation and Bioengineering*, 73:461–466, 1992.
  41. Dong Won Kim, Jae Ho Yang, and Young Kyo Jeong. Adsorption of cellulase from *Trichoderma viride* on microcrystalline cellulose. *Applied Microbiology and Biotechnology*, 28:148–154, 1988.
  42. Brian Kirby. *Micro- and Nanoscale Fluid Mechanics: Transport in Microfluidic Devices*. Cambridge University Press, first edition, 2010.

43. Jonas Korklach, Patrick J. Marks, Ronald L. Cicero, Jeremy J. Gray, Devon L. Murphy, Daniel B. Roitman, Thang T. Pham, Geoff A. Otto, Mathieu Foquet, and Stephen W. Turner. Selective aluminum passivation for targeted immobilization of single dna polymerase molecules in zero-mode waveguide nanostructures. *PNAS*, 105(4):1176–1181, 2008.
44. Andreas Kyriacou, Ronald J. Neufeld, and C. Roger MacKenzie. Effect of physical parameters on the adsorption characteristics of fractionated *Trichoderma reesei* cellulase components. *Enzyme and Microbial Technology*, 10:675–681, 1988.
45. El-Hang Lee, R.E. Benner, J.B. Fenn, and R.K. Chang. Angular distribution of fluorescence from liquids and monodispersed spheres by evanescent wave excitation. *Applied Optics*, 18:862–868, 1979.
46. Sun Bok Lee, H. S. Shin, Dewey D. Y. Ryu, and M. Mandels. Adsorption of cellulase on cellulose effect of physicochemical properties of cellulose on adsorption and rate of hydrolysis. *Biotechnology and Bioengineering*, 24:2137–2153, 1982.
47. Yuan-Hsiang Lee, Russell G. Maus, Ben W. Smith, and James D. Winefordner. Laser-induced fluorescence detection of a single molecule in a capillary. *Analytical Chemistry*, 66:4142–4149, 1994.
48. L. B. Lesem, P. M. Hirsch, and J. A. Jordan. The kinoform: a new wavefront reconstruction device. *IBM J. Res. Dev.*, 13:150–155, March 1969.
49. M.J. Levene, J. Korklach, S.W. Turner, M. Foquet, H.G. Craighead, and W.W. Webb. Zero-mode waveguides for single-molecule analysis at high concentrations. *Science*, 299:682–686, 2003.
50. Kecheng Li and Douglas W. Reeve. Fluorescent labeling of lignin in the wood pulp fiber wall. *Journal of Wood Chemistry and Technology*, 24(2):169–181, 2004.
51. David Liao, Peter Galajda, Robert Riehn, Rob Ilic, Jason L. Puchalla, Howard G. Yu, Harold G. Craighead, and Robert H. Austin. Single molecule correlation spectroscopy in continuous flow mixers with zero-mode waveguides. *Optics Express*, 16(14):10077–10090, 2008.
52. Knut Lundquist, Björn Josefsson, and Gunnar Nyquist. Analysis of lignin products by fluorescence spectroscopy. *Holzforschung*, 32:27–32, 1978.

53. J. S. Luterbacher, J.W. Tester, and L.P. Walker. High-solids biphasic  $CO_2-H_2O$  pretreatment of lignocellulosic biomass. *Biotechnology and Bioengineering*, 107:451–460, 2010.
54. A. Lykidis, K. Mavromatis, N. Ivanova, I. Anderson, M. Land, G. DiBartolo, M. Martinez, A. Lapidus, S. Lucas, A. Copeland, P. Richardson, D.B. Wilson, and N. Kyrpides. Genome sequence and analysis of the soil cellulolytic actinomycete *thermobifida fusca* yx. *J Bacteriol.*, 189(6):2477–2486, 2007.
55. Lee R. Lynd, Paul J. Weimer, Willem H. van Zyl, and Isak S. Pretorius. Microbial cellulose utilization: Fundamentals and biotechnology. *Microbiology and Molecular Biology Reviews*, 66(3):506–577, 2002.
56. Ali Mani, Thomas A. Zangle, , and Juan G. Santiago. On the propagation of concentration polarization from microchannel-nanochannel interfaces part i: Analytical model and characteristic analysis. *Langmuir*, 25:3898–3908, 2009.
57. Ali Mani, Thomas A. Zangle, and Juan G. Santiago. On the propagation of concentration polarization from microchannel-nanochannel interfaces part ii: Numerical and experimental study. *Langmuir*, 25:3909–3916, 2009.
58. Barry R. Masters and Peter So, editors. *Handbook of Biomedical Nonlinear Optical Microscopy*. Oxford University Press, 2008.
59. Matlab, 2010. Matlab Help File.
60. József Medve, Jerry Sthlberg, and Folke Tjerneld. Isotherms for adsorption of cellobiohydrolase i and ii from *trichoderma reesei* on microcrystalline cellulose. *Applied Biochemistry and Biotechnology*, 66:39–56, 1997.
61. W. E. Moerner. A dozen years of single-molecule spectroscopy in physics, chemistry, and biophysics. *Journal of Physical Chemistry B*, 106:910–927, 2002.
62. J. Moran-Mirabal, S.C. Corgie, J.C. Bolewski, H.M. Smith, B.R. Cipriany, H.G. Craighead, and L.P. Walker. Labeling and purification of cellulose-binding proteins for high resolution fluorescence applications. *Analytical Chemistry*, 81:7981–7987, 2009.
63. Jose M. Moran-Mirabal, Navaneetha Santhanam, Stephane C. Corgie,

- Harold G. Craighead, and Larry P. Walker. Immobilization of cellulose fibrils on solid substrates for cellulose-binding studies through quantitative fluorescence microscopy. *Biotechnology and Bioengineering*, 101(6):1129–1141, 2008.
64. Jose M Moran-Mirabal, Alexis J Torres, Kevan T Samiee, Barbara A Baird, and Harold G Craighead. Cell investigation of nanostructures: zero-mode waveguides for plasma membrane studies with single molecule resolution. *Nanotechnology*, 18, 2007.
  65. Douglas B. Murphy, David W. Piston, Stuart H. Shand, Simon C. Watkins, and Michael W. Davidson. Spectral bleed-through artifacts in confocal microscopy.
  66. Jörg Mütze, Thomas Ohrt, and Petra Schwille. Fluorescence correlation spectroscopy in vivo. *Laser & Photonics Reviews*, 5:52–67, 2011.
  67. NASA. Voyager, the interstellar mission.
  68. David L. Nelson and Michael M. Cox. *Lehninger Principles of Biochemistry*. W.H. Freeman and Company, fourth edition, 2004.
  69. B. Nidetzky, W. Steiner, and M. Claeysens. Cellulose hydrolysis by the cellulases from trichoderma reesei: Adsorptions of two cellulohydrolases, two endocellulases and their core proteins on filter paper and their relation to hydrolysis. *Biochem J.*, 303(3):817–823, 1994.
  70. Shuming Nie and Richard N. Zare. Optical detection of single molecules. *Annual Review of Biophysics and Biomolecular Structure*, 26:567–96, 1997.
  71. Dwight O. North. An analysis of the factors which determine signal/noise discrimination in pulsed-carrier svstems. *RCA Laboratories Technical Report*, (PTR-6C), June 1943.
  72. Osmair V. Oliveira, Luiz C. G. Freitas, T. P. Straatsma, and Roberto D. Lins. Interaction between the cbm of cel9a from *Thermobifida fusca* and cellulose fibers. *Journal of Molecular Recognition*, 22(1):38–45, 2008.
  73. Yngve Olsson, Erik Svensjö, Karl E. Arfors, and Dieter Hultström. Fluorescein labelled dextrans as tracers for vascular permeability studies in the nervous system. *Acta Neuropathologica*, 33(1):45–50, 1975.

74. Hiroshi Ooshima, Masaru Sakata, and Yoshio Harano. Adsorption of cellulase from *trichoderma viride* on cellulose. *Biotechnology and Bioengineering*, 25(12):3103–3114, 1983.
75. Ekmel Ozbay. Plasmonics: Merging photonics and electronics at nanoscale dimensions. *Science*, 311:189–193, 2006.
76. George H. Patterson, Susan M. Knobel, Wallace D. Sharif, Steven R. Kain, and David W. Piston. Use of the green fluorescent protein and its mutants in quantitative fluorescence microscopy. *Biophysical Journal*, 73(5):2782–2790, 1997.
77. James B. Pawley, editor. *Handbook of Biological Confocal Microscopy*. Springer, third edition, 2006.
78. Douglas C. Prasher, Virginia K. Eckenrode, William W. Ward, Frank G. Prendergast, and Milton J. Cormier. Primary structure of the *Aequorea Victoria* green-fluorescent protein. *Gene*, 111:229–233, 1992.
79. F.W.D. Rost. *Quantitative Fluorescence Microscopy*. Cambridge University Press, 1991.
80. F. J. W. Roughton. Diffusion and simultaneous chemical reaction velocity in haemoglobin solutions and red cell suspensions. *Progress in Biophysical and Biophysical Chemistry*, 9:55–104, 1959.
81. O. Du Roure, C. Debieuvre-Chouvy, J. Malthête, and P. Silberzan. Functionalizing surfaces with nickel ions for the grafting of proteins. *Langmuir*, 19:4138–4143, 2003.
82. Michael J Rust, Mark Bates, and Xiaowei Zhuang. Sub-diffraction-limit imaging by stochastic optical reconstruction microscopy (storm). *NATURE METHODS*, 3(10):793–795, 2006.
83. Gianfranco Rutili and Karl-E. Arfors. Fluorescein-labelled dextran measurement in interstitial fluid in studies of macromolecular permeability. *Microvascular Research*, 12:221–230, 1976.
84. K. T. Samiee, M. Foquet, L. Guo, E. C. Cox, and H. G. Craighead.  $\lambda$ -repressor oligomerization kinetics at high concentrations using fluorescence correlation spectroscopy in zero-mode waveguides. *Biophysical Journal*, 88:2145–2153, 2005.

85. Inder M. Saxena and JR R. M. Brown. Cellulose biosynthesis: Current views and evolving concepts. *Annals of Botany*, 96:9–21, 2005.
86. Susanne Schrof, Thorsten Staudt, Eva Rittweger, Nina Wittenmayer, Thomas Dresbach, Johann Engelhardt, and Stefan W. Hell. Sted nanoscopy with mass-produced laser diodes. *Optics Express*, 19:8066–8072, 2011.
87. Petra Schwille, Franz-Josef Meyer-Almes, and Rudolf Rigler. Dual-color fluorescence cross-correlation spectroscopy for multicomponent diffusional analysis in solution. *Biophysical Journal*, 72:1878–1886, 1997.
88. Osamu Shimomura, Funk H. Johnson, and Yo Saiga. Extraction, purification and properties of aequorin, a bioluminescent protein from the luminous hydromedusan, *Aequorea*. *Journal of Cellular and Comparative Physiology*, 59:223–239, 1962.
89. Bo Shui, Abdullah Ozer, Warren Zipfel, Nevedita Sahu, John Lis, Hua Shi, and Michael Kotlikoff. Rna aptamers that functionally interact with green fluorescent protein and its derivatives. *Submitted*, 2011.
90. Jerry Sthlberg, Gunnar Johansson, and Göran Pettersson. A new model for enzymatic hydrolysis of cellulose based on the two-domain structure of cellobiohydrolase I. *Nature Biotechnology*, 9:286–290, 1991.
91. Samuel M. Stavis, Stéphane C. Corgié, Benjamin R. Cipriany, Harold G. Craighead, and Larry P. Walker. Single molecule analysis of bacterial polymerase chain reaction products in submicrometer fluidic channels. *Biomicrofluidics*, 1:034105, 2007.
92. Samuel M. Stavis, Joshua B. Edel, Kevan T. Samiee, and Harold G. Craighead. Single molecule studies of quantum dot conjugates in a submicrometer fluidic channel. *Lab Chip*, 5:337–343, 2005.
93. Shigeru Terabe, Koji Otsuka, Kunimichi Ichikawa, Akihiro Tsuchiya, and Teiichi Ando. Electrokinetic separations with micellar solutions and open-tubular capillaries. *Analytical Chemistry*, 56(1):111–113, 1984.
94. P. Tomme, V. Heriban, and M. Claeysens. Adsorption of two cellobiohydrolases from *trichoderma reesei* to avicel: Evidence for “exo-exo” synergism and possible “loose complex” formation. *Biotechnology Letters*, 12:525–530, 1990.

95. Masaki Torimura, Shinya Kurata, Kazutaka Yamada, Toyokazu Yokomaku, Yoichi Kamagata, Takahiro Kanagawa, and Ryuichiro Kurane. Fluorescence-quenching phenomenon by photoinduced electron transfer between a fluorescent dye and a nucleotide base. *Analytical Sciences*, 17(1):155–160, 2001.
96. Craig Tuerk and Larry Gold. Systematic evolution of ligands by exponential enrichment: Rna ligands to bacteriophage t4 dna polymerase. *Science*, 249:505–510, 1990.
97. Jean-Louis Viovy. Electrophoresis of dna and other polyelectrolytes: Physical mechanisms. *Reviews of Modern Physics*, 72(3):813–872, 2000.
98. Dusan Vobornik, Daniel S. Banks, Zhengfang Lu, C. Fradin, Rod Taylor, and Linda J. Johnston. Fluorescence correlation spectroscopy with sub-diffraction-limited resolution using near-field optical probes. *Applied Physics Letters*, 93, 2008.
99. Jan Vogelsang, Thorben Cordes, Carsten Forthmann, Christian Steinhauer, and Philip Tinnefeld. Controlling the fluorescence of ordinary oxazine dyes for single-molecule switching and superresolution microscopy. *PNAS*, 106:8107–8112, 2009.
100. Jan Vogelsang, Robert Kasper, Christian Steinhauer, Britta Person, Mike Heilemann, Markus Sauer, and Philip Tinnefeld. A reducing and oxidizing system minimizes photobleaching and blinking of fluorescent dyes. *Angewandte Chemie*, 47:5465–5469, 2008.
101. Junichi Wada, Shou Ryu, Yuji Asano, Taro Ueno, Takashi Funatsu, Takao Yukawa, Jun Mizuno, and Takashi Tanii. Fabrication of zero-mode waveguide by ultraviolet nanoimprint lithography lift-off process. *Japanese Journal of Applied Physics*, 50:06GK07–1–5, 2011.
102. William W. Ward. *Green Fluorescent Protein: Properties, Applications, and Protocols*. John Wiley & Sons, 1997.
103. Jérôme Wenger, Fabien Conchonaud, José Dintinger, Laure Wawrezinieck, Thomas W. Ebbesen, Hervé Rigneault, Didier Marguet, and Pierre-François Lenne. Diffusion analysis within single nanometric apertures reveals the ultrafine cell membrane organization. *Biophysical Journal*, 92:913–919, 2007.

104. Jérôme Wenger, Davy Gérard, Pierre-François Lenne, Hervé Rigneault, José Dintinger, Thomas W. Ebbesen, Annie Boned, Fabien Conchonaud, and Didier Marguet. Dual-color fluorescence cross-correlation spectroscopy in a single nanoaperture : towards rapid multicomponent screening at high concentrations. *Optics Express*, 14:12206–16, 2006.
105. Jerker Widengren, Uelo Mets, and Rudolf Rigler. Fluorescence correlation spectroscopy of triplet states in solution: a theoretical and experimental study. *The Journal of Physical Chemistry*, 99:13368–13379, 1995.
106. Rebecca M. Williams, David W. Piston, and Watt W. Webb. Two-photon molecular excitation provides intrinsic 3-dimensional resolution for laser-based microscopy and microphotochemistry. *The FASEB Journal*, 8:804–813, 1994.
107. D B Wilson. Three microbial strategies for plant cell wall degradation. *Annals of the New York Academy of Sciences*, 1125:289–297, 2008.
108. Jonathan Woodward, Mary K. Hayes, and Norman E. Lee. Hydrolysis of cellulose by saturating and nonsaturating concentrations of cellulase: Implications for synergism. *Nature Biotechnology*, 6:301–304, 1988.
109. Fan Yang, Larry G. Moss, and Jr. George N. Phillips. The molecular structure of green fluorescent protein. *Nature Biotechnology*, 14:1246–1251, 1996.
110. Ahmet Yildiz, Joseph N. Forkey, Sean A. McKinney, Taekjip Ha, Yale E. Goldman, and Paul R. Selvin. Myosin v walks hand-over-hand: Single fluorophore imaging with 1.5-nm localization. *Science*, 300(5628):2061–2065, 2003.
111. Paul Zhu, Jose Moran-Mirabal, Jeremy Luterbacher, Larry P. Walker, and Harold G. Craighead. Observing *Thermobifida fusca* cellulase binding to pretreated wood particles using time-lapse confocal laser scanning microscopy. *Cellulose*, 18:749–758, 2011.
112. Rodger E. Ziemer, William H. Tranter, and D. Ronald Fannin. *Signals and Systems: Continuous and Discrete*. Macmillan Publishing Company, third edition, 1993.